

**Micromechanics of sediments: a variational approach to grain-scale
simulations**

by

Ran Holtzman

B.Sc. (Ben-Gurion University of the Negev, Israel) 1999
B.Sc. (Technion, Israel Institute of Technology, Israel) 2000
M.S. (Technion, Israel Institute of Technology, Israel) 2003

A dissertation submitted in partial satisfaction of the
requirements for the degree of
Doctor of Philosophy

in

Engineering - Civil and Environmental Engineering

in the

GRADUATE DIVISION
of the
UNIVERSITY OF CALIFORNIA, BERKELEY

Committee in charge:
Tadeusz W. Patzek, Chair
Dmitriy B. Silin
Nicholas Sitar
Tarek I. Zohdi

Fall 2008

**Micromechanics of sediments: a variational approach to grain-scale
simulations**

Copyright 2008

by

Ran Holtzman

Abstract

Micromechanics of sediments: a variational approach to grain-scale simulations

by

Ran Holtzman

Doctor of Philosophy in Engineering - Civil and Environmental Engineering

University of California, Berkeley

Tadeusz W. Patzek, Chair

The mechanics of particulate materials is studied through grain-scale simulations. We present a micromechanical model, termed Quasi-Static Granular Model (QuSGM). A three-dimensional, irregular pack of spherical grains is loaded by incremental displacements of its boundaries. Deformation is described as a sequence of equilibrium configurations. These configurations are found by minimizing the total potential energy of the pack with a modified conjugate gradient method. The macroscopic elastic moduli are evaluated from the intergranular forces and the deformation of the pack. Our quasi-static variational approach avoids the difficulties associated with numerical time integration encountered by dynamic models such as the discrete elements method.

To model cohesionless materials, we formulate constitutive laws based on the contact mechanics theories of Hertz, Mindlin, and Deresiewicz. Two types of models are presented: (a) *frictionless*, assuming ideally-smooth grains; and, (b) *frictional*, accounting for intergranular friction. Our simulations confirm that the bulk modulus mainly depends on the normal contact forces, and that grain-scale elasticity is suitable to describe many features of the inelastic response of granular materials. While our frictionless model supports the idea that microscopic friction is not the sole mechanism of macroscopic shear resistance, it underestimates the shear modulus. The frictional model is verified by assigning the experimentally-measured grain properties, and comparing the calculated effective moduli with published experiments. Good agreement between predicted and measured moduli, achieved with no adjustments of material parameters, establishes the physical soundness of the quasi-static approach.

Our results shed light on the important interactions between the microscopic and macroscopic scales. By micromechanical analysis we expose the mechanisms responsible for hysteresis, strain hardening, and stress-induced anisotropy. Our simulations capture rare “jump” events, in which few grains move significantly more than others, causing irreversible variations in the contact force network. Macroscopically, these variations correspond to large stress fluctuations, which significantly affect the bulk properties of a grain pack. These observations demonstrate the sensitivity of the bulk properties to small perturbations in the grain configurations, an intrinsic source of difficulty in predicting the behavior of particulate materials. Further difficulty is related to memory effects, which require information about the loading history to characterize a grain pack. Our observations are supported by published experiments.

We apply QuSGM to geological systems in which micromechanics of sediments is crucial. We examine the micromechanical origins for nonlinear deformation of the weakly-cemented sediments. Mechanisms for inelastic contact deformation, such as closure and opening of microcracks, are modeled by varying the stiffness of each contact according to the local deformation. Our model shows that account of nonlinear cement deformation at the grain-scale is required to reproduce the experimentally-observed bulk response. We use QuSGM to quantify the impact of hydrate dissociation on the mechanical properties of marine sediments. We deduce a degradation of sediment strength from a reduction of its elastic moduli. In conclusion, QuSGM shows great potential for advancing the understanding of granular mechanics, and modeling complex geological systems.

Tadeusz W. Patzek
Dissertation Committee Chair

To my wife, Shirli,

and

my daughters, Yaara and Tamar-Nadine

Contents

| | |
|--|-----------|
| List of Figures | v |
| 1 Introduction | 1 |
| 1.1 Motivation | 2 |
| 1.1.1 The importance of micromechanical evidence | 2 |
| 1.1.2 Complementing experimental data with computational methods | 3 |
| 1.1.3 Limitations of current computational techniques | 4 |
| 1.1.4 Advantages of modeling geologic materials as granular | 5 |
| 1.2 Objectives | 7 |
| 1.3 Review: micromechanical models for particulate matter | 8 |
| 1.3.1 Dimensionality | 8 |
| 1.3.2 Evaluation of grain-scale parameters | 9 |
| 1.3.3 Microstructure | 9 |
| 1.3.4 Boundaries of a grain pack | 11 |
| 1.3.5 Constitutive relations for intergranular interactions | 13 |
| 1.3.6 Modeling a deforming grain pack | 19 |
| 1.4 Overview | 23 |
| 2 A model of a cohesionless granular material | 25 |
| 2.1 Introduction | 25 |
| 2.2 Grain pack characterization | 26 |
| 2.3 Boundary conditions | 26 |
| 2.3.1 The boundaries of a grain pack | 26 |
| 2.3.2 Different types of loading | 28 |
| 2.4 Intergranular interactions between ideally-smooth grains | 28 |
| 2.5 Equilibrium configurations of the grains | 29 |
| 2.5.1 Balance equations | 29 |
| 2.5.2 Search for equilibrium by a variational approach | 30 |
| 2.6 Evaluation of macroscopic parameters of a grain pack | 30 |
| 2.6.1 Strain | 31 |
| 2.6.2 Stress | 31 |
| 2.6.3 Effective elastic moduli | 32 |
| 2.6.4 Porosity | 33 |

| | | |
|----------|---|-----------|
| 2.7 | Simulation results | 35 |
| 2.7.1 | Grain properties | 35 |
| 2.7.2 | Initial pack | 35 |
| 2.7.3 | Model verification | 38 |
| 2.7.4 | Micromechanical analysis | 42 |
| 2.8 | Concluding remarks | 47 |
| 3 | A granular pack model with intergranular friction | 49 |
| 3.1 | Introduction | 49 |
| 3.2 | Modeling a pack of grains | 50 |
| 3.2.1 | Microstructure | 50 |
| 3.2.2 | Microscopic material properties | 51 |
| 3.2.3 | Boundary conditions | 51 |
| 3.3 | Intergranular interactions: inelastic contacts | 51 |
| 3.3.1 | Normal contact forces | 51 |
| 3.3.2 | Tangential contact forces | 52 |
| 3.3.3 | Intergranular torsional couples | 55 |
| 3.3.4 | Intergranular moments | 56 |
| 3.4 | Equilibrium configurations | 57 |
| 3.5 | Macroscopic stress and strain | 58 |
| 3.6 | Simulation results | 59 |
| 3.6.1 | Material properties used in the simulations | 59 |
| 3.6.2 | Initial pack: introduction of frictional loads | 59 |
| 3.6.3 | Model verification | 61 |
| 3.6.4 | Sensitivity analysis | 62 |
| 3.7 | Concluding remarks | 69 |
| 4 | Nonlinear deformation of weakly-cemented sediments | 70 |
| 4.1 | Introduction | 70 |
| 4.2 | Inelastic response of weakly-cemented materials | 71 |
| 4.2.1 | Experimental macroscopic observations | 71 |
| 4.2.2 | Possible mechanisms for nonlinear contact deformation | 73 |
| 4.3 | Conceptual model of a pack of cemented grains | 76 |
| 4.4 | Constitutive relations for cemented grains | 77 |
| 4.4.1 | Normal component of the intergranular forces | 78 |
| 4.4.2 | Tangential component of the intergranular forces | 79 |
| 4.4.3 | Intergranular torques | 80 |
| 4.4.4 | Evolution of the effective contact stiffness | 81 |
| 4.5 | Initial configuration | 82 |
| 4.6 | Solution of the balance equations | 83 |
| 4.7 | The parallel bond model | 84 |
| 4.7.1 | Constitutive rules for intergranular interactions | 85 |
| 4.7.2 | Equilibrium configurations | 88 |
| 4.8 | Simulations of a deforming weakly-cemented sample | 88 |
| 4.8.1 | Reproduction of experimental data | 88 |

| | | |
|----------|--|------------|
| 4.8.2 | Examination of the performance of the numerical algorithm | 90 |
| 4.8.3 | Comparison of intergranular constitutive rules | 91 |
| 4.8.4 | Sensitivity analysis | 93 |
| 4.9 | Concluding remarks | 97 |
| 5 | Impact of hydrate dissociation in marine sediments | 98 |
| 5.1 | Introduction | 98 |
| 5.1.1 | Natural formation of methane hydrates | 99 |
| 5.1.2 | Hydrate distribution within the pore space | 100 |
| 5.1.3 | Chapter outline | 101 |
| 5.2 | Micromechanical impact of hydrate dissociation | 101 |
| 5.2.1 | A numerical hydrate-bearing sediment sample | 101 |
| 5.2.2 | Characterization of the effect of hydrate dissociation | 102 |
| 5.3 | Simulation results | 103 |
| 5.4 | Concluding remarks | 105 |
| 6 | Closure | 106 |
| 6.1 | Summary and conclusions | 106 |
| 6.2 | Future extensions | 108 |
| | Nomenclature | 111 |
| | Bibliography | 117 |
| A | Numerical algorithm | 132 |
| A.1 | Conjugate gradient: minimizing a quadratic criterion | 132 |
| A.2 | Modified algorithm implemented in granular mechanics | 134 |
| A.2.1 | Conjugate gradient for minimization of a non-quadratic criterion . . | 134 |
| A.2.2 | Conjugate gradient implemented in the cemented pack model | 138 |

List of Figures

| | | |
|------|--|----|
| 2.1 | A typical pack used in the numerical simulations. | 27 |
| 2.2 | Labeling of the boundary walls. | 27 |
| 2.3 | Contact geometry and intergranular forces used in the frictionless model. . . | 29 |
| 2.4 | The volume of a deformed grain pair, used in estimating the porosity. . . . | 34 |
| 2.5 | The distribution of the material properties of the grains. | 36 |
| 2.6 | The coordination number of the grains during the sample generation procedure. | 37 |
| 2.7 | A five-grain pack used in verification of the numerical algorithm. | 39 |
| 2.8 | The relative error of the numerical algorithm in simulations of self-similar deformations of a five-grain pack. | 40 |
| 2.9 | Verification against experiments: effective moduli predicted by the friction- less model. | 42 |
| 2.10 | Stress drops and strain hardening. | 44 |
| 2.11 | Correspondence between abrupt change of microstructure and stress drops. | 44 |
| 2.12 | Hysteretic stress-strain response in a loading-unloading cycle. | 45 |
| 2.13 | Microstructural evidence for the development of stress-induced anisotropy. . | 46 |
| 3.1 | The contact geometry and the intergranular loads in the frictional model. . | 53 |
| 3.2 | Intergranular shear force <i>vs.</i> relative displacement. | 54 |
| 3.3 | Intergranular torsional couple <i>vs.</i> relative rotation. | 57 |
| 3.4 | The effective shear modulus and ratio of sliding contacts during sample generation procedure and simulations of uniaxial compression. | 60 |
| 3.5 | Verification against experiments: effective moduli predicted by the frictional model. | 63 |
| 3.6 | Effect of initial packing on the macroscopic moduli. | 65 |
| 3.7 | Effect of the size of the load increments on the macroscopic moduli. . . . | 66 |
| 3.8 | Effect of the intergranular friction coefficient on the macroscopic moduli. . | 68 |
| 4.1 | A typical stress-strain curve from uniaxial compression of a synthetic sand- stone. | 72 |
| 4.2 | Acoustic wave velocities <i>vs.</i> axial stress measured in synthetically- and naturally-cemented sands. | 73 |
| 4.3 | Microcracks in SEM images of synthetic sandstones. | 74 |

| | | |
|------|--|-----|
| 4.4 | Irregular contact between grains bonded by granular cement in a synthetic sandstone. | 75 |
| 4.5 | SEM image showing cement distribution at different cement contents in synthetic sandstones. | 77 |
| 4.6 | Schematic description of a pair of cemented grains in the parallel bond model. | 87 |
| 4.7 | Matching experimental data with the exponential stiffness evolution model | 89 |
| 4.8 | Comparison of stress-strain curves computed by different intergranular constitutive rules. | 92 |
| 4.9 | Effective Young's modulus computed by the different intergranular constitutive rules. | 93 |
| 4.10 | The effect of the stiffness evolution parameters on Young's modulus. | 94 |
| 4.11 | The effect of the intergranular tangential stiffness on the bulk response. . . | 95 |
| 4.12 | The effect of the cement content on the bulk stiffness. | 96 |
| 5.1 | Diagram showing methane solubility and temperature for hydrate-gas-brine equilibrium as a function of depth. | 99 |
| 5.2 | Idealized cross section of the hydrate stability zone along a continental shelf. | 100 |
| 5.3 | Stiffness of artificial HBS samples with variable tetrahydrofuran-hydrate content. | 101 |
| 5.4 | Weakening of a hydrate-bearing sediment caused by hydrate dissociation. . | 104 |
| A.1 | Conjugate gradient algorithm for the minimization of a quadratic criterion. | 134 |
| A.2 | Modified conjugate gradient algorithm employed in our simulations with nonlinear equations. | 135 |
| A.3 | Modified conjugate gradient algorithm, used in simulations with the cemented pack model. | 139 |

Acknowledgments

I wish to express my gratitude to my advisor, Tadeusz Patzek, for guiding and supporting me through this stimulating and intensive period. His professional and personal advice has contributed greatly to my work, and to my academic maturity and independence. I am greatly indebted to my other adviser, Dmitriy Silin from the Lawrence Berkeley Lab, for his endless professional and personal support. By closely following my work and providing constructive advice and criticism, he has greatly improved my professional abilities.

Also gratefully acknowledged is Tarek Zohdi for critical advice throughout my research, and careful review of this dissertation. I am also thankful to Nicholas Sitar, for reviewing the thesis and offering helpful comments. Special thanks are due to Seiji Nakagawa for providing me with invaluable experimental data, and constructive remarks. I also wish to thank Jim Berryman from the Lawrence Berkeley Lab and Jack Dvorkin from Stanford for fruitful discussions.

I want to thank my fellow students, Pascual, Guodong, Katie, Linsey, and Roger, for their support and advice, and my former advisor, Uri Shavit, for laying the foundations to my professional development and for his friendship. I am immensely grateful for the endless support I received from my family, especially my parents, Eli and Dafna Holtzman, and my father and mother in law, Amos and Nadine Breskin. Finally, the love and understanding I received from my wife, Shirli, and daughters, Yaara and Tamar-Nadine, made this work possible.

This work has been partially supported by the Jane Lewis Fellowship from the University of California, Berkeley, and by the Assistant Secretary for Fossil Energy, Office of Natural Gas and Petroleum Technology, through the National Energy Technology Laboratory, under the U.S. Department of Energy, Contract #DE-FC26-05NT42664. Additional support was provided through the unrestricted research gifts from the oil industry to Professor Tadeusz Patzek.

Chapter 1

Introduction

GRANULAR MATERIALS are a collection of discrete particles or “grains”. They constitute a large group of natural and artificial materials, from powders and seeds to sands and boulders, with scales varying from nanometers to meters. These substances are frequently encountered in daily life, making understanding of their behavior important in many practical applications [Jaeger et al., 1996b,a; Behringer & Jenkins, 1997; Herrmann et al., 1998; Behringer et al., 1999; Bagi, 2004; Hinrichsen & Wolf, 2005].

The subject of this dissertation is the mechanics of granular matter, namely the evolution of its mechanical properties under deformation. Complex interactions among grains, together with disordered microstructure and heterogenous stress distribution, lead to highly nonlinear, hysteretic behavior, where small perturbations can significantly alter the bulk response [Behringer et al., 1999]. For example, slight changes in packing density can result in a transition from a solid- to a fluid-like behavior, i.e. loss of shear rigidity, and vice-versa, i.e. jamming [O’Hern et al., 2003]. Consequently, understanding the mechanics of granular materials is among the deepest and most interesting unsolved problems in solid-state physics [O’Hern et al., 2003; Bagi, 2004; Hinrichsen & Wolf, 2005; Walsh et al., 2007]. This challenge is enhanced by the limited data stemming from experimental and computational difficulties.

The purpose of this dissertation is to enhance the understanding of granular mechanics, with applications to geophysical systems, i.e. micromechanics of sediments and rocks. To study the underlying mechanisms that determine the behavior of geological materials, we construct a suite of models. The complex physics of particulate materials poses certain restrictions on computations, which we address by formulating a novel computational technique. The results of our simulations delineate relations between grain-scale

and macroscopic properties. Our model provides important insights into the underlying physics, advancing our ability to predict the mechanical response of granular matter.

This chapter is organized as follows. In Section 1.1 we motivate the problem, highlighting its practical importance and the benefits of modeling a granular pack by grain-scale numerical simulations. The objectives are specified in Section 1.2. In Section 1.3, we review different approaches to micromechanical modeling. Finally, in Section 1.4, we discuss the scope, and provide an overview of this dissertation.

1.1 Motivation

Intensive study of granular mechanics has been motivated by its large socio-economic impact and the intriguing underlying science. Despite the substantial progress in understanding of granular mechanics, many questions remain unsolved [Behringer et al., 1999; Bagi, 2004; Hinrichsen & Wolf, 2005], particularly in the context of geologic materials [Haff, 1997]. Here, we review these unresolved challenges and some of the related applications, which have motivated the approach taken in this dissertation.

1.1.1 The importance of micromechanical evidence

The mechanical properties of a particulate material are determined by the grain properties and the intergranular interactions, see, e.g., Oda et al. [1998], Behringer et al. [1999], Ribière et al. [2005], Muthuswamy & Tordesillas [2006], Kruggel-Emden et al. [2007], Walsh et al. [2007], Cole & Peters [2007], Tavaréz & Plesha [2007], Peña et al. [2008] and the references therein. Consequently, continuum macroscopic models have limited predictive capabilities relative to discrete grain-scale models.

Analysis of grain displacements and contact forces provides crucial insight into mechanisms that control the response of a granular sample. For example, most of the load within a grain pack is carried by relatively few grains, termed “force chains”, see, e.g., Behringer et al. [1999], Majmudar & Behringer [2005], Goldenhirsch & Goldenberg [2005] and the references therein. Minute perturbations of the microstructure, for instance large displacements of several grains, can lead to large fluctuations in the force network, with significant consequences for the mechanical properties of the pack [Behringer et al., 1999; Ribière et al., 2005; Peña et al., 2008]. In cemented materials, heterogenous force distribution can lead to fracturing and failure of the material, which cannot be predicted

from macroscopic averaged quantities such as stress [Potyondy & Cundall, 2004]. Relating the micro- and macro-scale is a fundamental and necessary task in the study of granular matter [Kruijdt & Antony, 2007; Walsh et al., 2007].

1.1.2 Complementing experimental data with computational methods

A major obstacle in understanding granular mechanics is the lack of micromechanical evidence. Technical difficulties restrict measurements at the grain scale, i.e. intergranular forces and grain displacements [Cole & Peters, 2007]. Consequently, computational methods have become a valuable tool in obtaining such data [Kruggel-Emden et al., 2007; Walsh et al., 2007; Cole & Peters, 2007; Tavaréz & Plesha, 2007; Peña et al., 2008]. A review of experimental techniques with their shortcomings follows.

The microstructure, e.g. grain shapes and positions, can be evaluated by two types of procedures: (a) construction of a three-dimensional (3D) image from a sequence of two-dimensional (2D) microscope images [Lin & Cohen, 1982; Tomutsa & Silin, 2004]; and (b) 3D microtomography by magnetic resonance imaging (MRI) [Ng & Wang, 2001] or X-ray tomography [Fu, 2005]. In (a), the sequence of sections is usually obtained by polishing with an abrasive surface. However, the polishing procedure limits the resolution of the sectioning to a micron scale, insufficient to investigate the pore space of materials such as chalk [Tomutsa & Silin, 2004]. Alternatively, focused ion beam can be used for successive removal of layers as fine as ten nanometers [Tomutsa & Silin, 2004]. Regardless of the sectioning technique, damage is introduced, obscuring the analysis [Jin, 2006]. Additionally, these methods are cumbersome.

While microtomography offers limited spatial resolution (~ 1 micron), it is non-destructive, allowing to track grain displacements during an experiment. For instance, Ng & Wang [2001] conducted shear tests inside the magnetic core of MRI equipment. Ribière et al. [2005] used glass beads immersed in index matching oil containing a laser dye, packed within a transparent vessel. Confocal microscopy was used to track the motion of the beads, which appear as dark circles of variable intensity according to their distance from the lens. Behringer et al. [1999] used transparent boundaries to track motions of photoelastic disks.

Measurements of intergranular forces are restricted to either 2D setting, a single pair of grains, or along the sample's boundaries. Forces acting between a single pair of grains can be evaluated through the deformations on their contact interfaces, which can be

measured using laser sensors [Cole & Peters, 2007] or atomic force microscopy [Grierson et al., 2005]. Forces within an assembly of grains can be evaluated using photoelastic materials. When placed between crossed polarizers, these materials produce light patterns according to the strain they experience, from which the stress can be evaluated [Behringer et al., 1999]. Photoelastic surfaces allow force measurements along the boundaries [Corwin et al., 2005]. A 2D force network can be evaluated by loading an array of photoelastic disks, see Behringer et al. [1999], Majmudar & Behringer [2005], Goldenhirsch & Goldenberg [2005] and the references therein.

A methodic investigation of the effect of local microscopic properties on the response of a granular pack requires numerous realizations, varying the type of grains, the microstructure, and the loading scheme, among other factors [Taboada et al., 2006]. The aforementioned short-comings of experimental techniques together with increasing computing capabilities make grain-scale numerical simulations an attractive alternative [Li et al., 2005; Taboada et al., 2006; Kruggel-Emden et al., 2007; Walsh et al., 2007; Cole & Peters, 2007; Peña et al., 2008]. The ability of such simulations to predict the macroscopic properties and reproduce microscopic features such as force chains is encouraging.

1.1.3 Limitations of current computational techniques

The large, highly-nonlinear system of equations corresponding to the large number of grains¹ and the complexity of the intergranular interactions require construction of efficient computational techniques [Vu-Quoc & Zhang, 1999a; Tavaréz & Plesha, 2007]. A delicate balance must be achieved by modeling the complex interactions in a simple manner, while preserving the essential grain-scale physics. For example, the effective medium theory offers a relatively simple analytical solution based on highly-restrictive simplifying assumptions, which limit its applicability, see Section 1.3.6.1.

Lacking sufficient experimental data, studies of granular mechanics heavily rely on numerical grain-scale simulations. Particularly, the Discrete Element Method (DEM) [Cundall & Strack, 1979] is widely used in modeling many types of granular materials. A review of numerical methods in granular mechanics is provided in Section 1.3.6.2; here, we

¹As an example, a $100 \times 10 \times 10 \text{ mm}^3$ sample of sand with average grain radius of $\sim 0.1 \text{ mm}$, packed in a simple-cubic lattice (porosity of $\sim 48\%$), contains $\sim 2.4 \cdot 10^6$ grains. Obviously, the higher packing efficiency of natural samples makes the number of grains even larger [Jaeger & Nagel, 1992]. Computational constraints often restrict simulations to a few thousands of grains.

highlight some of the principal difficulties in these methods, which motivated us to seek for an alternative approach.

In DEM, intergranular interactions are modeled as a dynamic process, accounting for grain inertia. The equilibrium configurations are obtained by explicit numerical integration of Newton’s equation of motion over time. Constraints imposed on the time step make DEM simulations time-consuming [O’Sullivan & Bray, 2004; Tavaréz, 2005; Tavaréz & Plesha, 2007]. To damp grain oscillations and accelerate computations, a damping parameter is often introduced, and its value together with those of material properties such as the grain density and contact stiffness are adjusted [Thornton, 2000; O’Sullivan et al., 2004; Potyondy & Cundall, 2004; Jin, 2006; Peña et al., 2008], sometimes to unrealistic values. Such values may lead to “over-damping” of the grain motion, resulting in a substantial number of grains that are not in mechanical equilibrium. While it is difficult to determine an appropriate time step for the numerical integration, detection of the related instabilities may be masked by other energy-dissipative mechanisms [Tavaréz & Plesha, 2007]. In this dissertation, we propose a technique which does not require numerical integration, avoiding the aforementioned difficulties.

1.1.4 Advantages of modeling geologic materials as granular

Our work is geared towards geophysical applications, involving deformation of soils and rocks. By “soils” we refer to uncemented sediments such as sands, which fall under the classical definition of *cohesionless* granular matter. By “rocks” we refer to cemented sediments, as well as crystalline and metamorphic rocks. In particular, we focus on the poorly-consolidated, weakly-cemented sediments, denoted hereafter as *cohesive* materials. In these highly-porous materials, the grains are bonded together at their contacts by small amounts of cement. Here, we briefly discuss the natural occurrence of these substances, and provide few examples of applications in which knowledge of their mechanical properties is crucial.

Sediments are formed by deposition (also denoted as “settlement” or “sedimentation”) of mineral grains, either transported or formed *in-situ*, followed by compaction and diagenesis [Jin, 2006]. Diagenetic processes include alteration of the minerals by physical, chemical or biological processes. The compaction process is studied in details in this dissertation. As a result of diagenesis, the sediment may become cemented. Particularly,

cement around the contacts can form by deposition of minerals which infiltrate to the pore space in aqueous solution, see, e.g., Bernabè et al. [1992]; Jin [2006]; Garcia & Medina [2007] and the references therein, and pressure dissolution [Tada & Siever, 1989; Dewers & Ortoleva, 1990; Renard et al., 2000; Gratier et al., 2005]. For example, low fluxes of suspensions containing cementing agents, e.g. clay particles, are attracted by capillarity to the pore throats, where cement is deposited [Garcia & Medina, 2007]. In pressure solution, stress concentration at the intergranular contacts causes grains to dissolve. The dissolved minerals can then reprecipitate at adjacent free grain surfaces [Tada & Siever, 1989]. Investigating the mechanical effects of such cementation is an important objective of this work.

Under special circumstances, sediments can have cohesive strength from sources other than cement, and thus exhibit behavior which is somewhat closer to that of a cemented material. For example, in powders or clays made of particles smaller than ~ 10 microns, van der Waals and electrostatic forces are comparable to other forces, e.g. gravity [Visser, 1989]. Alternatively, low saturation of fluids can generate strong capillary forces, enhancing the sediment's stability [Halsey & Levine, 1998]. Finally, ice and gas-hydrates can serve as unstable cement material, for instance in marine sediments [Dvorkin et al., 1999]. The effect of gas-hydrates and their dissociation is explored in this dissertation.

The abundance of related applications and their large socioeconomic impact make understanding of geologic materials crucial. Examples of natural phenomena and industrial applications in which soil and rock micromechanics play a decisive role include:

- *Depositional and diagenetic processes in sediments.* The flow and mechanical properties of sediments and sedimentary rocks are determined by deposition and diagenesis [Jin et al., 2003; Jin, 2006; Garcia & Medina, 2007].
- *Landslides.* A major worldwide hazard, which also has a significant geomorphologic impact, as it often controls long-term slope erosion rates. Determination of landslide initiation, travel mode, and size is crucial, yet not well-known [Aharonov & Katz, 2006; Katsman et al., 2006].
- *Faulting and activation of faults.* Relative shear of fault planes and fault gouges involve fracturing and grain breakage near the fault plane. Faulting is important in understanding tectonics and earthquakes [Guo, 2006; Mair et al., 2007].

- *Geotechnical projects.* Design and stability analysis of an underground structure, foundation, landfill, or soil improvement depends on the subsurface mechanical and flow properties [Tejchman & Wu, 1995].
- *Reservoir engineering.* Water and oil reservoirs are made of porous sediments and rocks. Safe and efficient design and operation of these reservoir requires handling problems such as subsidence, well-bore instability, and sanding, see Saidi et al. [2003] and the references within.
- *Conveying and storing* seeds, soils, and powders [Shimizu, 2002].

1.2 Objectives

The main objective of this work is the study of granular mechanics. We wish to determine the main mechanisms involved in deforming a particulate material, and predict evolution of its properties. In particular, we seek to relate the microscopic and macroscopic properties. The following objectives are set forth to achieve these goals:

1. *Formulation of physically-based mathematical models of granular matter.* Micromechanical models are developed for two type of materials: (a) cohesionless, and (b) weakly-cemented. A crucial component is the formulation of constitutive relations to model the intergranular interactions. Simple, yet comprehensive rules are proposed, involving few parameters which can be evaluated experimentally.
2. *Delineation of important microscopic mechanisms.* Analysis of numerical simulations with the above models together with published experimental data are used to quantify the effects of phenomena observed at the meso-scale on the bulk response. Relating the grain- and macro-scale is considered one of the fundamental challenges in granular mechanics.
3. *Prediction of the mechanical properties of a granular sample.* Successful fulfilment of the former items promotes the ability to predict the macroscopic properties of a granular sample, which are of interest in most practical applications.
4. *Application of granular mechanics to geological systems.* We use our models to study: (a) the impact of cementation on the behavior of weakly-cemented sediments, focusing on the determination of the micromechanical origins for the nonlinear sediment

deformation; and (b) the consequences of hydrate dissociation in unconsolidated sediments.

5. *Development of efficient computational techniques.* Finding the equilibrium configurations of the grains requires numerical solution of a large, highly-nonlinear system of equations. To avoid the difficulties involved in solving these equations by numerical integration, we develop a variational approach, in which the solution is obtained by minimizing the pack’s potential energy. A modified conjugate gradient method is proposed for the minimization.

1.3 Review: micromechanical models for particulate matter

In micromechanical models, also denoted hereafter as “discrete” or “grain-scale”, the material response is predicted from account of the grain-scale physics. Thus, a grain-scale model includes information about the geometrical and material properties of the grains. From these properties, the grain motion is related to the intergranular loads *via* a set of constitutive relations. In this section, we review approaches taken to model the micromechanics of a granular sample, focusing on aspects related to implementation within numerical simulations. We discuss the characterization of a pack of grains, the constitutive rules, and analytical and numerical methods employed to compute the bulk response of the pack.

1.3.1 Dimensionality

Computations and analysis of 2D models are significantly simpler than in 3D, as the number of degrees of freedom is reduced, and “out-of-plane” motion is prohibited [Ghaboussi & Barbosa, 1990]. Moreover, 2D settings allow for easier experimental measurements of grain-scale parameters, for instance of the displacements and forces in an array of photoelastic disks [Behringer et al., 1999]. However, differences in the geometry and kinematics make extrapolation of material properties obtained from a 2D model into the actual 3D geometry questionable [Ghaboussi & Barbosa, 1990; O’Sullivan, 2002; Hazzard & Mair, 2003; Tavarez & Plesha, 2007].

1.3.2 Evaluation of grain-scale parameters

We distinguish between two approaches: (a) “one-to-one” modeling, where each physical grain is modeled explicitly, allowing to evaluate the model parameters from measurements of grain-scale properties, see, e.g., Holtzman et al. [2008b,a]; and (b) grains are model elements used to discretize a porous continuum, in order to compute the effective bulk properties of a heterogeneous medium, see, e.g., Tavaréz & Plesha [2007]. Each “grain” in the model is a volumetric element which may represent both solid grains and pore space. Thus, the model parameters in (b) are the *effective* properties of a granular volume, which may differ significantly from the properties of the *grains* within that volume. While approaches (a) and (b) are conceptually different, they can be implemented with similar computational techniques, e.g., DEM.

The number of grain-scale model parameters depends on the constitutive relations. Simple relations that are based on established theories, such as those described in Section 1.3.5, offer the advantage of having fewer model parameters which can be measured from experiments. In other models, the value of parameters which cannot be measured is often determined by an *ad hoc* process of validating the modeling results with a set of experimental data [Tavaréz & Plesha, 2007]. Tavaréz & Plesha [2007] proposed a methodology to evaluate such grain-scale parameters from given macroscopic properties. The authors relate grain-scale and macroscopic parameters through an analytical solution, obtained for a unit cell containing several particles arranged in a regular manner.

1.3.3 Microstructure

1.3.3.1 Grain shapes

The mechanical properties of a granular sample are affected by the grain shapes. For instance, experimental comparison between round and angular grains shows that the bulk stiffness and the slope angle of a poured granular material increase with grain angularity [Murphy, 1982; Robinson & Friedman, 2002]. Interlocking in angular grains makes the bulk response more anisotropic, see Peña et al. [2008] and the references within, and can increase the amount of plastic grain deformations at high stresses [Murphy, 1982].

Irregular grain shapes, or large deformations of regularly-shaped grains, make the contact geometry complex. In modeling a granular sample, such geometry complicates formulation of the contact detection algorithm [Ghaboussi & Barbosa, 1990; Williams

& O'Connor, 1995] and the intergranular constitutive rules [Munjiza et al., 1995]. The large number of grains in a pack increases the challenge in modeling complex geometries. As a result, the grain shapes are often approximated by spheres (disks in 2D), allowing characterization of the grain size by a single parameter, its radius [Kruggel-Emden et al., 2007; Tavarez & Plesha, 2007], or ellipsoids (ellipses) [Rothenburg & Bathurst, 1991; Lin & Ng, 1997; Vu-Quoc et al., 2000; Jin, 2006]. The small and localized grain deformations exhibited in many cases [Johnson, 1987] justify such approximations even for deformed grains. Alternatively, 2D polygons [Alonso-Marroquin & Herrmann, 2002; Peña et al., 2008], and 3D polyhedra [Ghaboussi & Barbosa, 1990] are used. Irregular grains can be modeled by clusters of spherical grains, bonded together at their contacts [Jensen et al., 1999; Vu-Quoc et al., 2000]. Such approach maintains the computational simplicity, while allowing to model grain damage and fracturing [Jensen et al., 2001; Abe & Mair, 2005].

Modeling grains *via* simple shapes may not be appropriate when inhibition of grain rotations and interlocking are crucial, for instance in granular flow of highly-irregular grains [Ghaboussi & Barbosa, 1990; Tavarez & Plesha, 2007]. Moreover, the assumption of rounded grains can obscure the effect of other parameters. For example, the importance of grain size distribution increases with the angularity of the grains [Mair et al., 2002; Robinson & Friedman, 2002; Guo, 2006]. Nonetheless, the predictive capabilities demonstrated by models employing simple grain shapes (see, e.g., Walsh et al. [2007], Cole & Peters [2007], Tavarez & Plesha [2007] and the references within), imply that, at least for relatively round particulate materials, such a simplification is satisfactory.

1.3.3.2 Packing

Characterization of a disordered packing, e.g. through a fabric tensor [Mehrabadi et al., 1988], is cumbersome. Conversely, it is much simpler to characterize a structured packing of uniform grains. In addition, structural symmetries make computations of the bulk response easier. For example, by assuming infinitesimally-small deformations of a grain lattice, Duffy [1959] obtained a closed-form analytical solution relating the macroscopic stress and strain. O'Sullivan [2002] used structured arrangements to compare experiments and simulations. However, the author reported that material and geometrical heterogeneities diminished the symmetry once the pack was loaded.

Symmetry is highly uncommon in natural materials [Deresiewicz, 1958a; Vaisnys

& Pilbeam, 1975; Goldenhirsch & Goldenberg, 2005]. Since microstructure plays a significant role in determining the mechanical properties of a grain pack, a regular arrangement cannot reliably reflect the behavior of a natural material [O’Sullivan, 2002; Bagi, 2003]. For these reasons, in most models a disordered (“random”) packing is used. In particular, random packing of spherical grains is considered appropriate to model many natural granular systems [Finney, 1970; Bagi, 2003, 2005; Zhang & Makse, 2005; Jin, 2006].

To simulate deformation of a grain pack, a sufficiently dense, irregular initial equilibrium configuration is required [O’Sullivan, 2002; Bagi, 2005]. The density of the packing is usually characterized through the coordination number of the grains [Saidi et al., 2003]. A dense, irregular configuration could be obtained by advanced imaging of a physical sample. However, imaging procedures are cumbersome. Alternatively, an initial configuration could be generated numerically, using either “constructive” or “dynamic” algorithms [Bagi, 2005]. Constructive algorithms are based on geometry alone and thus require relatively small computing time; however, these algorithms may produce arrangements with low coordination numbers, gaps, or anisotropic structure [Bagi, 2005].

In dynamic algorithms, a loose packing is created by placing a relatively small number of grains in a bounded domain. Then, the packing density is increased by either expanding the grains or moving the boundaries closer together. A static equilibrium configuration is found by simulating intergranular interactions, e.g. with DEM. The large number of collisions and grain rearrangements makes such a procedure time-consuming [Bagi, 2005]. A more efficient procedure based on a quasi-static compaction model is presented in Section 2.7.2.

1.3.4 Boundaries of a grain pack

The boundaries in a model of a grain pack represent the outermost parts of the pack, which are in direct interaction with the surroundings. We use the term boundary conditions to refer to the mechanical and geometrical properties of the boundaries. External loading on the pack is modeled by moving the boundaries, forcing the grains to rearrange and deform.

We distinguish between two types of conceptual models, in which the domain represents: (a) an entire sample, such as that used in a triaxial test; and (b) a representative volume element (RVE) of a larger medium, such as a small volume within an *in-situ* geologic

strata or large sample. The different external environment experienced by the outermost grains in (a) and (b) imply that different boundary conditions should be assigned.

In a triaxial test, the sample is encapsulated within the solid walls of a load cell [Jaeger & Cook, 1979]. Regardless of the type of test, if the sample is cohesionless, external physical boundaries are required to keep the pack intact. The regular shape of such boundaries, e.g. a load cell, make it convenient to place the model boundaries at the cell's walls. Since these walls may have properties different than those of the grains, the model parameters and type of interactions between the boundaries and the outermost grains can differ significantly than those which are assigned for the grains within the pack.

Conversely, in an RVE, the interactions with the boundaries represent the physical interactions with the external grains surrounding the RVE, and thus should be as similar as possible to those within the pack itself [Mesarovic & Padbidri, 2005]. The concept of an RVE is often introduced when the size of the domain of interest is too large for direct modeling of its constituents. In granular materials, the large number of grains makes such approach essential.

Common types of boundaries used in modeling an RVE are: (1) solid walls, (2) a peripheral layer of particles, and (3) periodic boundary conditions. The simplest approach is bounding the RVE by solid walls, which are assigned material properties similar to those of the grains. The grains along the boundaries interact with the walls, presumably in a manner similar to the interactions with neighboring grains. However, the different kinematic constraints posed by solid walls introduces boundary effects. These effect may be partially reduced by replacing the solid walls with a peripheral layer of particles, displacing the boundaries by affine motions of these particles [Heyliger & McMeeking, 2001]. Nevertheless, such an irregular surface may lead to the undesired concentrated stresses near the boundaries, caused by interactions with the protruding boundary grains.

In many types of problems, periodic boundary conditions reduce the boundary effects. To model a rectangular granular pack, Martin et al. [2003] proposed the following approach: when a particle protrudes outside the RVE through a given face, an additional “mirror” particle is generated on the opposite face. The mirror particle interacts with other particles on that face. However, mirror particles may still introduce artificial concentrated loads at the boundaries [Mesarovic & Padbidri, 2005].

Boundary effects can lead to quantitative errors, such as overestimated bulk stiffness due to protruding grains, and qualitative errors, where phenomena such as localization

are not reproduced [Procopio & Zavaliangos, 2005; Mesarovic & Padbidri, 2005]. In addition, the analysis of micromechanical models involves evaluation of the macroscopic stress and strain from the grain-scale parameters, which may also be affected by the boundaries [Holt, 2001]. The effect of the boundaries on the interior parts of the pack is reduced by increasing the size of the domain [Mesarovic & Padbidri, 2005]. To limit the influence on the subsequent analysis, e.g. on the evaluation of macroscopic properties, the analysis can be performed on a smaller subdomain, far from the boundaries [Holt, 2001; Mesarovic & Padbidri, 2005].

Finally, we note that in a triaxial test, the presence of the load cell affects the test results [Jaeger & Cook, 1979]. Thus, a relatively large sample is used to minimize these effects. In simulating a triaxial test, the computational constraints on the number of grains may amplify the influence of the boundaries. Furthermore, for simplicity, simulations often use a rectangular domain, while most experiments are performed on cylindrical samples [Jaeger & Cook, 1979]. However, using rectangular samples allows application of three different loads in three perpendicular direction (“polyaxial loading”), as opposed to two only in triaxial² tests on a cylindrical sample. The importance of the intermediate load in determining the sample’s strength, led to the development of experimental techniques for polyaxial testing on rectangular samples [Chang & Haimson, 2000].

1.3.5 Constitutive relations for intergranular interactions

External loading on the boundaries of a grain pack causes the grains to rearrange and deform. Deformation of the grains, and, in a cemented pack, of the cement material, is accompanied by stresses. Micromechanical models use a set of constitutive rules which relate the deformations, evaluated from the relative motion between the grains, to the resultant forces and moments.

If grains experience large, inelastic deformations, the contact geometry and the intergranular interactions become highly complicated [Johnson, 1987]. In such cases, inelastic grain deformations can be modeled through the intergranular constitute rules, see, e.g., Vu-Quoc & Zhang [1999b] and Zhang & Vu-Quoc [2007]. Alternatively, finite elements method (FEM) approximation of each contact region can be employed to compute the force-displacement relations [Munjiza et al., 1995]. In modeling stiff grains, e.g. sands,

²The naming is somewhat misleading: strictly speaking, in a triaxial tests the load is biaxial, with identical loads in two principal directions. Accordingly, a polyaxial test is often called “true triaxial”.

it is often assumed that grains experience small deformations, with negligible grain damage or fracturing. This assumption is based on the experimental observation that, unless exceedingly high stresses are applied, individual grains exhibit very little damage [Deresiewicz, 1958a; Vaisnys & Pilbeam, 1975]. Similarly, in cemented grain packs, most of the damage occurs within the cement material [Bernabè et al., 1992; Yin & Dvorkin, 1994; Holt, 2001; Saidi et al., 2003].

Using linear-elasticity to model grain deformations, together with simplified grain and contact geometry, allows development of closed-form, analytical expressions for the constitutive rules. In particular, the contact theories of Hertz [1882], Mindlin & Deresiewicz [1953] and Deresiewicz [1954] are often employed in constructing quasi-static rules. For a wide range of materials undergoing small deformations, the Hertzian model is considered an adequate description of the force component acting normal to the contact interface, see Johnson [1987], Dintwa et al. [2008] and the references therein. Similarly, the models of Mindlin and Deresiewicz adequately describe intergranular shear (Johnson [1987], Dobry et al. [1991], Vu-Quoc & Zhang [1999a] and the references therein) and torsion [Johnson, 1987; Segalman et al., 2005].

In this dissertation, we formulate constitutive rules based on the theories of Hertz, Mindlin, and Deresiewicz. Below, we summarize the underlying assumptions and main concepts employed in these theories, where the essential formulae are provided in Sections 2.4 and 3.3. In Chapter 4 we develop constitutive rules for cemented grains; a literature review of such rules follows in Section 1.3.5.3.

1.3.5.1 Hertzian contact theory

The Hertzian contact theory accounts for the normal compressive force developed at the interface between two bodies (grains) pressed against each other. The following assumptions are employed in this theory:

- (1) Ideally smooth (“frictionless”) contact surfaces.
- (2) Stresses are highly concentrated in a region close to the contact interface.
- (3) The contact area is much smaller than the size of each grain.
- (4) The contact area is much smaller than the radius of curvature of the grains.
- (5) The deformation of each grain is small enough to be approximated by linear-elasticity.

- (6) The material of each of grain is isotropic and homogeneous.

From the first assumption, it follows that only normal tractions are transmitted across grain contacts. The contact surfaces are considered sufficiently smooth to ignore the effect of microscopic irregularities, e.g. asperities, which could lead to high variations in the contact stresses. To simplify the mathematical formulation, the geometry of the grain surface near the contact interface is approximated by a second-order polynomial.

Assumption (2) is based on the physical observation that stresses decrease rapidly with the distance from the contact interface. Thus, the stresses in the contact region do not critically depend upon details far away from that region, such as shape of the distant portions of the grains or the way they are supported. This insensitivity allows to approximate each grain as infinite in size relative to the contact region. Combining the latter approximation with assumptions (3) and (4), the geometry of each grain is modeled by a half-space, semi-infinite in extent and bounded by a planar surface. The contact area (circular for spherical grains) is modeled as a plane which lies within this planar surface.

Based on the former assumptions, together with (5) and (6), the stresses and strains developed away from the contact region are neglected, assuming remote parts of the grains experience rigid body motion. Furthermore, if a grain is compressed against several grains, the locality of the small stresses allows the forces to be evaluated independently. To obtain an analytical solution using the theory of linear elasticity, a boundary-value problem is formulated with the following boundary conditions: at the contact interfaces, prescribed normal displacements; along the other boundaries, zero tractions. Analytical expression is obtained by adopting a known solution in terms of the stresses satisfying these conditions. The solution admits an axisymmetric pressure distribution, and the resultant force is found by integration over the contact area.

Hertzian theory is often used to evaluate the normal force component acting between non-smooth particles, assuming that the effect of the loads caused by frictional resistance on the normal component is negligible [Johnson, 1987]. This hypothesis was verified numerically [Dintwa et al., 2008], and justified theoretically for the spacial case of identical grain properties, as well as for dissimilar properties if the coefficient of static friction between the grains, μ , is much less than unity [Johnson, 1987].

An extension of Hertz's theory to more general settings, accounting for dynamics, inelastic deformations and rough surfaces, can be found in Johnson [1987]. For a review of

such “extended” models, and their implementation in numerical simulations, see Kruggel-Emden et al. [2007].

1.3.5.2 Mindlin-Deresiewicz contact theory

A model for the loads associated with frictional resistance at the contact between two bodies, denoted hereafter as “frictional loads”, was presented by Cattaneo [1938] and independently by Mindlin [1949]. The authors considered the special case of monotonic tangential load applied with a fixed normal compression. Extensions for simultaneous variations in the normal and tangential loads [Mindlin & Deresiewicz, 1953] and torsional oscillations [Deresiewicz, 1954] are described below. Since intergranular torsion has little effect on the macroscopic stress, see Section 3.5, we focus here on the tangential component.

In developing their theory, Mindlin and Deresiewicz adopted some of the assumptions listed in the previous section. Each grain is modeled as a linear-elastic half-space, undergoing small and localized deformations. The effect of the frictional loads on the normal force is assumed negligible, such that the normal force component can be computed independently, using Hertz’s theory. Two modes of contact are considered: (a) stick (or, “no-slip”); and (b) slip. If the entire contact area is in stick, the contact surfaces do not move relative to each other. Thus, relative lateral motion of the bodies deforms the region around the contact in shear. In slip, portions of the contact surfaces move relative to each other. Employing Coulomb friction model, if the entire surfaces slip (“slide”), the resultant tangential force Q is evaluated by $Q = \mu P$, where P is the normal force. Thus, sliding is expected if the angle between the oblique force and the contact area exceeds $\tan^{-1}(\mu)$.

With the assumption of no-slip, kinematic boundary conditions computed from the relative displacements between the grains are prescribed. Solution of a boundary-value problem with these conditions predicts infinite stress at the edge of the contact area [Mindlin, 1949]. Thus, “partial slip” (otherwise denoted by “micro-slip”) is considered: a portion of the contact area is slipping, while the remainder is in stick³. The slipping area is found by assuming Coulomb’s model holds point-wise, meaning that the tangential tractions can be computed as the product of the normal tractions and the friction coefficient, μ . Under fixed normal compression, the model predicts slip at the outer edges of the con-

³Partial slip is not expected if the grains are loaded by an oblique force with the ratio of tangential to normal forces held fixed: if this ratio is smaller than μ , slip will occur over the entire contact area; otherwise, it will not occur at all [Walton, 1978; Johnson, 1987]

tact area, spreading inwards as the tangential load is increased⁴. As the tangential force approaches the product of the normal force and the friction coefficient, the stick region shrinks to a point, and the bodies slide.

Experiments show that slip causes energy dissipation, related to plastic deformation by shearing of surface asperities [Johnson, 1987]. Dissipation makes the deformation process path-dependent, where forces depend on the loading path. As an example, consider loading by a fixed normal force, while increasing the tangential force. Slip will spread from the outer annulus inwards, directed along the direction of the tangential force. Now, if the tangential load is subsequently decreased, the process does not simply reverse. Instead, slip in the *opposite* direction begins at the edge of the contact [Johnson, 1987]. In consideration of this path-dependency, the contact tractions are determined by following, in incremental steps, the load history [Johnson, 1987; Elata & Berryman, 1996]. At each step, the compliance relating the incremental force and displacement is evaluated according to the loading scheme, e.g. if the normal and tangential components increase, decrease, or remain fixed.

In a similar manner, Mindlin [1949] and Lubkin [1951] solved for the torsional couples induced by monotonic rotation between two bodies. The authors show that slip in a circumferential direction can develop at the edge of the contact area. The latter work was extended for small oscillatory loading by Deresiewicz [1954]. In these models, torsion is assumed to be decoupled from the tangential component.

1.3.5.2.1 Related models. The path-dependency makes implementation of the theory of Mindlin and Deresiewicz in problems involving multiple contacts cumbersome [Vu-Quoc & Zhang, 1999a]. Computational difficulties led to the development of simpler models, which reduce the path-dependency [Elata & Berryman, 1996]. For example, Vu-Quoc & Zhang [1999a] considered fewer loading schemes, and demonstrated implementation of their model in DEM simulations. Walton & Braun [1986] proposed a model which ignores the effect of the normal force increment, considering only tangential loading or unloading. A further simplification is obtained by ignoring partial slip, i.e. assuming either perfect stick or sliding [Chang et al., 1992; Jenkins & Strack, 1993], or ignoring slip altogether by assuming an infinitely large friction coefficient [Johnson & Norris, 1997]. Such simplifications make the force-displacement relation path-independent.

⁴For spherical bodies, slip will occur in an outer annulus.

The large number of grains requires a balance between accuracy and efficiency. While some of the models described above may not be appropriate if the details of an individual contact are of interest [Elata & Berryman, 1996], the importance of some of these details is reduced when a large grain pack is considered. For instance, models using a contact law which ignores frictional loads can describe many features of the inelastic response of granular materials [Goldenhirsch & Goldenberg, 2005; Holtzman et al., 2008b].

The model of Vu-Quoc & Zhang [1999a] was extended in Vu-Quoc & Zhang [2001] and Zhang & Vu-Quoc [2007] to account for inelastic grain deformations. For theories accounting for dynamic loading and inelastic grain deformations, see Johnson [1987].

1.3.5.3 Constitutive relations for cemented grains

Here, we review constitutive rules which are used to model cemented particulate materials. In most models, the complex geometry of cement deposited around the grain contacts [Jin, 2006; Brouste et al., 2007] is approximated by simpler shapes. Additionally, cement is often assumed to deform as linear elastic. The validity of the last assumption is examined in Chapter 4.

Most often, the cemented contacts are modeled by a spring of fixed stiffness. For example, to simulate brittle failure of rocks, Jin et al. [2003] represented interactions between each pair of cemented grains by an elastic spring, modeling cement failure by removing the spring. In Jiang et al. [2006], a set of springs distributed within the contact area is used to evaluate the rolling resistance between grain pairs.

To evaluate the stiffness and strength of the cemented contacts, Potyondy & Cundall [2004] developed a “parallel bond” model. The authors evaluate the loads in the grain-grain and grain-cement portions of each contact independently, through two sets of constitutive rules. The total load at each contact is computed by superimposing the two components. This approach allows to use contact mechanics theories for the grain-grain portion. The cemented portion is modeled by a linear-elastic beam, evaluating its strength and stiffness from existing analytical solutions. Potyondy [2007] extended the model in Potyondy & Cundall [2004] to represent corrosion due to cement dissolution in silicate rocks, by assigning a damage-rate law for each bond.

The widely-used models of Dvorkin et al. [1991, 1994] are based on contact mechanics theories. Dvorkin et al. [1991] developed force-displacement relations for two elastic

grains bonded by an elastic cement layer, with either: (a) an arbitrarily-shaped cement layer loaded by relative normal and lateral grain displacements, ignoring the grain deformations; and (b) a straight cement layer loaded by normal grain compression, using the “elastic foundation” model [Johnson, 1987]. The latter, (b), was verified by experiments in photoelastic disks [Sienkiewicz et al., 1996] and FEM simulations [Zang & Wong, 1995].

Dvorkin et al. [1994] extended the model in Dvorkin et al. [1991] by accounting for the tangential force component, considering two types of cement distribution: (a) exclusively at the contacts; and (b) coating the grains. The model requires numerical evaluation of several parameters. Closed-form expressions for upper and lower bounds, assuming either rigid grains or cement layer, were proposed by Zhu et al. [1996a], and later extended in [Zhu et al., 1996b] to account for visco-elastic materials. Dvorkin & Nur [1996] demonstrated good agreement between the elastic moduli predicted by a mean-field approximation employing the model in Dvorkin et al. [1994], and experimentally-measured moduli.

Garcia & Medina [2007] proposed an approach which accounts for arbitrarily-shaped cement deposited: (a) at the contacts; (b) around each grain; and (c) at the pore bodies. The grain-grain interactions are modeled through molecular dynamics simulations (see Section 1.3.6.2), whereas the deformation of cement is evaluated by discretizing the cement volume into a lattice, considering cement as particles placed at the lattice nodes. The interactions among the cement particles are modeled *via* a spring-dashpot-slider system. Finally, FEM approximation can be used to model complex cement geometry and non-linear deformations, e.g. within the framework of the finite-discrete elements method [Munjiza et al., 1995]; however, such approach is computationally cumbersome.

1.3.6 Modeling a deforming grain pack

1.3.6.1 Analytical solutions

Closed-form analytical solutions for the deformation of a structured packing of identical spherical grains have been proposed in the literature [Duffy & Mindlin, 1957; Deresiewicz, 1958b; Duffy, 1959; Thurston & Deresiewicz, 1959]. These solutions are based on computations performed on a unit cell, assuming deformations that are sufficiently small to neglect distortion of the packing. Closed-form expressions for the stress-strain relations are computed for an infinite periodic medium.

Extensions to irregular packings under finite macroscopic deformations, known as “Mean Field” or “Effective Medium Theory” (EMT), are obtained by relating the grain and the macroscopic scales by spatial averages, see, e.g. Digby [1981], Walton [1987], Jenkins & Strack [1993], Johnson et al. [1998] and Pride [2005]. Here, we briefly outline the principles; a thorough discussion of the method appears in Goddard [1990]. EMT is based on the assumption that the macroscopic work done in deforming the pack is the sum of the works done against the intergranular forces, replacing the latter by a spatial average [Makse et al., 2001]. The average work associated with each contact is estimated with the following assumptions: (a) the center of each grain displaces according to the macroscopic strain, such that its motion can be projected from the macroscopic strain; and (b) the distribution of contacts is spherically symmetric, allowing averaging of the forces over all possible contact orientations. The loads at the contacts are computed from the projected grain displacements, through a set of constitutive rules, cf. Section 1.3.5. The stress is computed by a spatial average of the forces acting inside a granular volume. Additional simplified assumption often used is that of affine motion, ignoring grain rotations.

Walton [1987] used the above to evaluate the effective elastic moduli from the grain properties, employing the contact model in Walton [1978]. In spite of the restrictive simplifying assumptions, Walton’s theory provides a reasonably-accurate approximation for the bulk modulus under high confining stresses [Makse et al., 2004; Pride, 2005]. However, the theory generally fails to reproduce the shear modulus, as well as the evolution of the moduli in relatively low confining stresses [Goddard, 1990; Makse et al., 1999; Pride, 2005]. Numerical simulations suggests that Walton’s theory fails to predict the shear modulus because of the assumption of affine motion, which neglects stress relaxation during shear through grain rotations [Makse et al., 2001, 2004]. To explain the discrepancy between Walton’s theory and experiments, Goddard [1990] proposed two alternative mechanisms: (1) deviations from Hertzian law, related to a surface asperities or grain angularity; and (2) variations in the coordination number caused by buckling of force chains.

Consolidated aggregates can be modeled within the framework of EMT, by an introduction of appropriate constitutive relations, see Pride [2005] and the references therein. For example, Elata & Dvorkin [1996] used the model of cemented contacts by Dvorkin et al. [1994] within the framework of EMT in Digby [1981].

1.3.6.2 Grain-scale numerical simulations

Here, we review several techniques for simulating a deforming grain pack. We focus on the widely-used DEM, originally proposed by Cundall & Strack [1979]. Detailed description of the method can be found in O’Sullivan [2002], Bicanic [2004], Jin [2006] and Tavaréz [2005]. In DEM, interactions among the grains are treated as a dynamic process, accounting for the grain inertia. The method consists of three major computational steps, performed sequentially at each time step: (a) contact detection; (b) evaluation of the intergranular loads; and (c) integration of the equations of motion to compute the grain displacements.

Step (a) is trivial for spherical grains, yet involves elaborate algorithms for more complex shapes [Williams & O’Connor, 1995]. Step (b) employs a set of constitutive rules and corresponding parameters. In step (c), the linear and angular accelerations of each grain are computed from Newton’s second law. The linear and angular grain velocities and displacements are evaluated by repeated numerical integration over time of the equations of motion. A subsequent configuration is computed using the grain displacements, and the analysis is repeated. A sequence of grain configurations is produced, describing the evolution of the deformation process in time.

The second-order integration is usually performed using an explicit central difference method, making the algorithm conditionally stable, depending on the time step used [O’Sullivan & Bray, 2004; Tavaréz & Plesha, 2007]. Determining an appropriate time step is difficult, especially in nonlinear problems where the minimal step size changes during the simulations [Tavaréz & Plesha, 2007]. Moreover, it may be difficult to detect numerical instabilities because of the different energy-dissipative mechanisms. The constraints imposed on the time step make DEM simulations time-consuming [O’Sullivan & Bray, 2004; Tavaréz & Plesha, 2007]. To accelerate computations and damp grain oscillations, a numerical damping parameter is often introduced, and its value together with those of material properties such as the grains density and their contact stiffness are adjusted [Thornton, 2000; O’Sullivan et al., 2004; Tavaréz, 2005; Potyondy & Cundall, 2004; Jin, 2006; Peña et al., 2008], sometime to unrealistic values. Such adjustments affect the mechanical properties of the pack, and may result in “over-damping” of the grain motion, leaving a substantial number of grains away from a stable equilibrium [Thomas & Bray, 1999].

Related methods which use explicit time integration include molecular dynamics and cellular automata. Unlike DEM, where only grains in contact interact, in molecular dynamics the particles follow a negative gradient of a global potential, that depends on the positions of remote grains [Haile, 1992]. Thus, molecular dynamics is most suitable to model particles which interact by forces of attraction, such as atomic forces between molecules and gravitational forces between planets. Recently, Garcia & Medina [2007] employed molecular dynamics to simulate deformation of a cemented grain pack.

Cellular automata, originally used to model gases and liquids, can be applied in granular mechanics, see, e.g, Budhu et al. [1999], Kozicki & Teichman [2005] and the references therein. A porous rock volume is represented by a lattice, where each lattice cell can be occupied by either a portion of a solid particle or the pore space. The interactions between cells occupied by solids can be chosen to mimic contact between two particles, or otherwise between two adjacent pieces of a single particle, allowing to model particle damage. At each time step, each particle may move from its current cell to an adjacent cell, avoiding overlaps. Obviously, such models impose artificial kinematic restrictions. The large number of cells and the small time steps required in the numerical integration makes the algorithm cumbersome.

A dynamic model which employs implicit time integration of the equations of motion is utilized in Thomas [1997] and Thomas & Bray [1999]. The authors modeled a 2D array of disks using the discontinuous deformation analysis (DDA) method introduced by Shi [1988]. DDA employs minimization of potential energy and the penalty method to solve for the displacements of blocks. Consequently, a system of linear equations is solved at each time step [Thomas, 1997]. To maintain stability of the algorithm and obtain a physically meaningful solution, a small time step must be taken [Thomas & Bray, 1999]. Tavarez [2005] points out that, in modeling granular mechanics, the constraints on the time step reduces the merits of using an implicit scheme.

Finally, in problems in which dynamics is of lesser importance, the aforementioned difficulties can be avoided by employing a quasi-static model. O'Hern et al. [2003] simulated deformation of a pack of ideally-smooth particles, finding the equilibrium configurations by minimizing a potential function. Minimization was performed iteratively, using the conjugate gradient algorithm. Renouf & Alart [2005] discussed the implementation of conjugate gradient methods in granular mechanics, including the account of interparticle friction. Recently, Holtzman et al. [2008b,a] proposed a computational technique to simu-

late 3D quasi-static deformation of a grain pack, in which the equilibrium configurations are found by minimizing the potential energy of the pack. This technique is described in details in this dissertation.

1.4 Overview

We develop a conceptual model of a granular material, implemented within a computational framework, termed Quasi-Static Granular Model (QuSGM). In QuSGM, the mechanical properties of a granular sample are evaluated by simulating its deformation. A 3D irregular pack of spherical grains is loaded by incremental displacements of its boundaries. Intergranular interactions are modeled by a set of constitutive relations, based on contact mechanics theories. The macroscopic stress and strain, and the effective elastic moduli are computed from the intergranular forces and displacements. We use a quasi-static model, describing deformation as a sequence of static equilibrium configurations. At a given (“reference”) configuration, incremental displacements of the boundaries force the grains to deform and rearrange into a new (“current”) configuration. To obtain an equilibrium configuration, we employ a variational approach, finding the grain displacements and rotations that provide a minimum of an energy functional. This minimum is computed using a modified conjugate gradient algorithm.

Under the assumption of perfectly elastic contacts, the energy functional is evaluated from the total potential energy of the pack, including the strain energy stored in the deformed grains, and the gravitational energy. The physical basis for our approach is the principle of minimum potential energy [Timoshenko & Goodier, 1970], frequently applied to solve multi-body problems, e.g. in structural engineering. When considering energy dissipation by sliding, we employ the principle of least work [Timoshenko & Goodier, 1970], and evaluate the functional from the work done against the intergranular loads.

This dissertation is organized as follows. Chapters 2–3 are concerned with the development of a mathematical model for cohesionless granular matter. To model the intergranular interactions, we consider two types of constitutive rules: (1) “frictionless”, assuming ideally smooth grains (Chapter 2); and (2) “frictional”, including the effect of intergranular friction (Chapter 3). We verify our model against published experiments. We demonstrate the physical soundness of our model by its ability to predict the mechanical properties of a sample, given its grain properties, with no adjustments of material parame-

ters. Our results provide a relation between the grain- and macro-scale, revealing essential mechanisms responsible for hysteresis, strain hardening, and stress-induced anisotropy.

We apply QuSGM to geological systems, in which micromechanics of sediments and rocks is crucial. In Chapter 4 we study the micromechanical origins of the nonlinear deformation of weakly-cemented sediments, introducing several suites of constitutive relations to account for possible microscopic deformation mechanisms. We show that account of nonlinear cement deformations at the grain-scale is required to reproduce the experimentally-observed nonlinear bulk response. In Chapter 5 we use QuSGM to quantify the impact of hydrate dissociation on the mechanical properties of marine sediments. We demonstrate degradation in sediment strength as a reduction in the macroscopic elastic moduli. Concluding remarks are provided in Chapter 6. Details of the numerical algorithm used to solve for the equilibrium configurations are presented in Appendix A.

*Who could ever calculate the path of a molecule?
How do we know that the creations of worlds are not
determined by falling grains of sand?*

– VICTOR HUGO
Les Misérables (1862)

Chapter 2

A model of a cohesionless granular material

2.1 Introduction

WE STUDY the mechanics of cohesionless granular materials through grain-scale simulations. A micromechanical model is presented, assuming ideally-smooth (“frictionless”) grains. Under this assumption, the grains can rotate and slide relative to each other without developing resistive forces at their contacts. Thus, the only intergranular loads developed are normal compressive contact forces. We justify the frictionless assumption by the following hypothesis: in a dense pack of rounded grains, the size of the asperities associated with surface roughness that resist lateral and angular displacements is much smaller than the size of the grains themselves. Consequently, the bulk response, e.g. macroscopic stress, is mostly affected by the normal force components. Numerical simulations [Thornton & Antony, 1998; Thornton, 2000; Krut & Antony, 2007] and analytical computations [Rothenburg & Bathurst, 1989; Goldenhirsch & Goldenberg, 2005] support this hypothesis.

The outline of this chapter is as follows. The mathematical model and computational algorithm, formulated within the framework of QuSGM, are provided in Sections 2.2–2.6. In Sections 2.2–2.3 we characterize a grain pack and its boundaries. The constitutive relations governing the intergranular interactions are given in Section 2.4. The methodology of obtaining the equilibrium configurations is summarized in Section 2.5. Section 2.6 describes the evaluation of the macroscopic parameters. Section 2.7 presents the simulation results. The values of material parameters used in the simulations, taken from published experiments, are listed in Section 2.7.1. In Section 2.7.2, a procedure to generate the initial

packing is outlined. In Section 2.7.3, the accuracy of the computational algorithm and the predictive capabilities of the model are examined. Micromechanical analysis is presented in Section 2.7.4. This analysis allows linking microscopic and macroscopic observations, by which we demonstrate mechanisms responsible for the path-dependent, hysteretic response typical of granular materials. Finally, concluding remarks are provided in Section 2.8. Essential results from this chapter were published in Holtzman et al. [2008b].

2.2 Grain pack characterization

We model granular matter as a heterogeneous, irregular (“random”) 3D packing of spherical grains, see Figure 2.1. Under the assumption of frictionless contacts, ignoring intergranular shear and moments, the configuration of a pack of spheres can be described *via* their positions and radii. At each reference configuration, the deformation caused by perturbing the boundary conditions is characterized by the displacements of the grains relative to the reference configuration. Thus, a 3D pack of N grains has $3N$ degrees of freedom. Labeling the grains with a single index, $i = 1, 2, \dots, N$, we denote the radius of grain i by R_i . The grain displacement is $\mathbf{u}_i = \mathbf{r}_i - \mathbf{r}_i^0$, where \mathbf{r}_i is the radius-vector of the grain center, and superscript 0 denotes the reference configuration, see Figure 2.3. The unknowns are written as a vector of generalized coordinates, $\boldsymbol{\theta} = [\mathbf{u}_1 \dots \mathbf{u}_N]^T$, where \mathbf{u}_i are row vectors, and superscript T denotes the transpose.

We model each grain as a homogenous and isotropic linearly-elastic body, which undergoes small deformations with no grain fracturing or breakage. Thus, the material of grain i is characterized by its Young’s modulus, E_i , and Poisson’s ratio, ν_i . The grain’s density, ρ_i , is of lesser importance; while gravity stabilizes a loose packing, its effect is negligible relative to the contact forces in a dense, stressed pack.

2.3 Boundary conditions

2.3.1 The boundaries of a grain pack

We model external loading by relative displacements of the pack’s boundaries. The boundaries are represented by solid planar walls which interact with the outermost grains. We align the domain with a cartesian coordinate system, labeling each boundary with a single index, $w = 1, 2, \dots, 6$, where each pair of parallel walls, $w = l$ and $w = l + 3$,

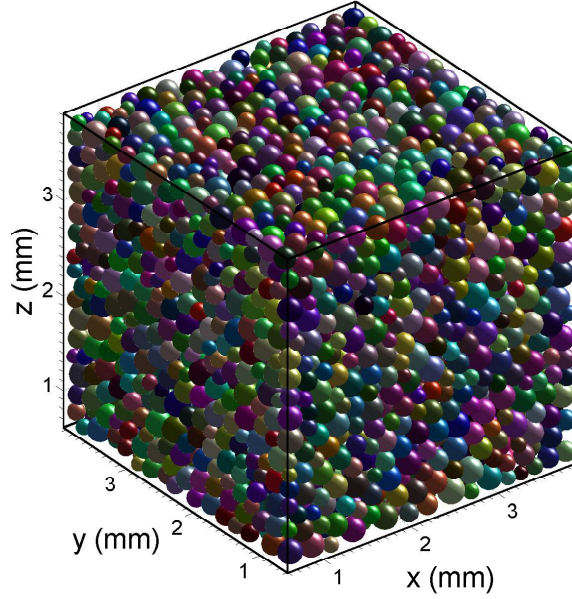


Figure 2.1: A typical pack with 5036 grains used in the numerical simulations.

is associated with a principal direction ($l = 1, 2, 3$), see Figure 2.2. The position of a planar boundary w is determined from its orientation, specified by an inward unit normal, $\hat{\mathbf{n}}_w$, and an arbitrary point on the plane, \mathbf{x}_w , see Figure 2.3. The displacement of the boundary is denoted by \mathbf{u}_w . To compute the intergranular interactions with the outermost grains, the material properties of the walls must be specified; here, we model the walls as linear elastic solids, with Young's modulus and Poisson's ratio of E_w and ν_w , respectively.

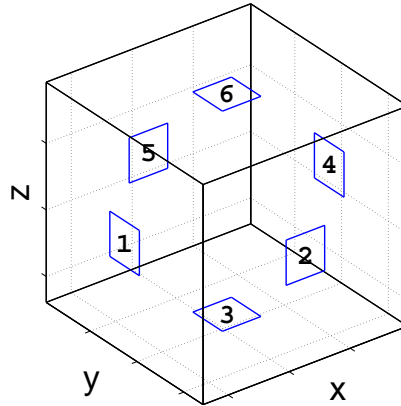


Figure 2.2: Labeling the boundary walls using a single index, $w = 1, 2, \dots, 6$.

2.3.2 Different types of loading

In laboratory testing, deformations are applied by controlling either: (a) the external force applied to the boundaries; or (b) the boundary displacements. Here, we enforce boundary displacements, and compute the resulting forces on the boundaries. In our model, the macroscopic stress and strain are computed from these boundary forces and displacements, see Section 2.6. We simulate isotopic (often denoted as “hydrostatic”) or polyaxial loading by enforcing identical or different normal strains in three perpendicular directions, respectively. A triaxial test is simulated by applying two identical strains in two perpendicular (“lateral”) directions. Application of uniaxial strain models loading of a laterally-confined pack, where lateral stresses develop due to the confinement.

2.4 Intergranular interactions between ideally-smooth grains

We model intergranular interactions through a constitutive relation based on the contact theory of Hertz [1882], neglecting cohesive or frictional loads. Let a pair of grains, i and j be in contact. The contact area is a planar disk of radius a_{ij} , computed by

$$a_{ij} = (R_{ij}h_{ij})^{1/2} \quad (2.1)$$

The magnitude of the normal compressive force acting at the contact is

$$\|\mathbf{P}_{ij}\| = \frac{4}{3}E_{ij}(R_{ij})^{1/2}(h_{ij})^{3/2} \quad (2.2)$$

where

$$R_{ij} = (1/R_i + 1/R_j)^{-1} \quad (2.3a)$$

$$E_{ij} = [(1 - \nu_i^2)/E_i + (1 - \nu_j^2)/E_j]^{-1} \quad (2.3b)$$

are effective geometric and elastic coefficients associated with this contact, respectively [Hertz, 1882]. Here $\|\boldsymbol{\xi}\| = (\boldsymbol{\xi} \cdot \boldsymbol{\xi})^{1/2}$ denotes the magnitude of vector $\boldsymbol{\xi}$. The above equations are applicable to a grain-boundary contact by assigning an infinite radius to the planar wall, i.e. $R_{iw} = R_i$. The normal compression is quantified by the mutual approach, $h_{ij} \geq 0$,

$$h_{ij} = R_i + R_j - \|\mathbf{r}_{ij}\| \quad \text{for grain-grain contact} \quad (2.4a)$$

$$h_{iw} = R_i - (\mathbf{r}_i - \mathbf{x}_w) \cdot \hat{\mathbf{n}}_w \quad \text{for grain-boundary contact} \quad (2.4b)$$

where $\mathbf{r}_{ij} = \mathbf{r}_i - \mathbf{r}_j$, see Figure 2.3. The normal force acting on grain i at the contact with another grain j or a wall w is directed along \mathbf{r}_{ij} or $\hat{\mathbf{n}}_w$, respectively. Thus, zero moment relative to the center of the grain is associated with the normal force.

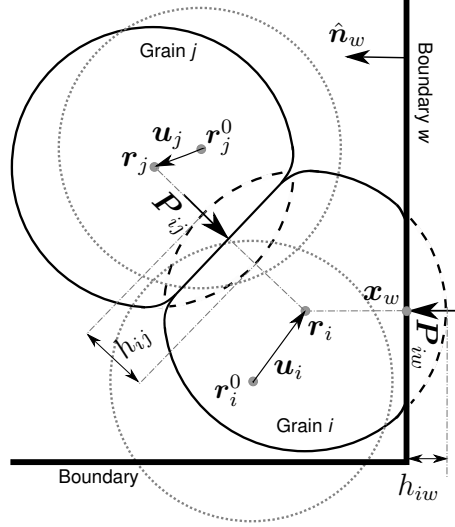


Figure 2.3: Contact geometry and intergranular forces used in the frictionless model. The reference configuration of the grains and boundary walls is marked with grey dotted lines. The dashed lines show the shapes of the undeformed grains in the current configuration.

2.5 Equilibrium configurations of the grains

2.5.1 Balance equations

At equilibrium, the grain configuration satisfies the force and moment balance equations. Under the assumption of frictionless grains, the moments are zero, reducing the balance equations force equilibrium,

$$\mathbf{F}_i = \sum_{j=1}^{N_g^i} \mathbf{P}_{ij} + \sum_{w=1}^{N_b^i} \mathbf{P}_{iw} - m_i g \hat{\mathbf{e}}_z = \mathbf{0} \quad (2.5)$$

where \mathbf{F}_i is the sum of forces acting on grain i , $\hat{\mathbf{e}}_z$ is a unit vector pointing opposite to the direction of gravity, g is the gravity acceleration, and the grain mass is $m_i = (4/3)\pi R_i^3 \rho_i$. Here N_g^i and N_b^i denote the number of contacts of grain i with other grains and boundaries, respectively. The coordination number of grain i is $N^i = N_g^i + N_b^i$. Note that the set of contacts for each grain varies with the deformation of the pack, introducing additional nonlinearity to that instituted by the contact laws.

2.5.2 Search for equilibrium by a variational approach

Each equilibrium configuration is characterized by the generalized coordinates, $\boldsymbol{\theta}$, which satisfy Eq. (2.5). We employ a variational approach, obtaining each configuration by finding a local minimum of an energy functional, Π , with respect to $\boldsymbol{\theta}$. Using the principle of minimum potential energy [Timoshenko & Goodier, 1970], we evaluate Π from the potential energy of the grains. The potential energy is a function of the grain deformations (strain energy) and the gravitational potential of the grains. The elastic strain energy of a pair of grains in contact is equal to the sum of work done on each grain to deform it. This work equals the dot product of the force with the displacement increment, integrated over the total displacement. Thus, the strain energy, $U_{ij(n)}$, stored in the deformed contact region between grains i and j is (cf. Eq. (9.15) in Landau & Lifshitz [1986]):

$$U_{ij(n)} = \frac{8}{15} E_{ij} (R_{ij})^{1/2} (h_{ij})^{5/2} \quad (2.6)$$

The total potential energy of the pack is computed by summing the strain energy over all contacts¹, and the gravitational potentials over all grains,

$$\Pi(\boldsymbol{\theta}) = \sum_{i=1}^N \left\{ \frac{1}{2} \sum_{j=1}^{N_g^i} U_{ij(n)} + \sum_{w=1}^{N_b^i} U_{iw(n)} + m_i g (\mathbf{r}_i \cdot \hat{\mathbf{e}}_z - z^*) \right\} \quad (2.7)$$

where z^* is an arbitrary fixed reference elevation.

We find the minimum of Π numerically. The search is performed iteratively, by modifying the conjugate gradient algorithm to accommodate the nonlinearity of the system, see Appendix A. The gradient of Π with respect to $\boldsymbol{\theta}$ is

$$\nabla_{\boldsymbol{\theta}} \Pi = -[\mathbf{F}_1 \dots \mathbf{F}_N]^T \quad (2.8)$$

where the sum of forces, \mathbf{F}_i , is written as a row vector. Thus, zero gradient of Π is equivalent to the balance of forces.

2.6 Evaluation of macroscopic parameters of a grain pack

The scale of most practical problems involves analysis of macroscopic parameters, such as stress, strain, effective elastic moduli, and porosity. In addition, most of the

¹The factor of 1/2 arises because the strain energy $U_{ij(n)}$ in Eq. (2.7) is the energy stored in each *pair* of deformed grains due to their contact, which is counted twice when summing over all *grains*.

experimental evidence is macroscopic. Here, we develop simple procedures to evaluate these parameters from the grain-scale parameters computed in our simulations. We note that the concept of stress and strain in a granular assembly is not clearly defined, see Bagi [1996], Bagi [2006], Goldenhirsch & Goldenberg [2005] and the references therein.

2.6.1 Strain

The macroscopic strain is evaluated here from the displacements of the boundary walls. The strain tensor, ϵ , is defined by

$$\epsilon = \frac{1}{2} [\nabla_{\mathbf{x}} \mathbf{u} + (\nabla_{\mathbf{x}} \mathbf{u})^T] \quad (2.9)$$

where \mathbf{x} is a radius-vector to the center of an infinitesimal volume, and \mathbf{u} is the center's displacement [Landau & Lifshitz, 1986]. We estimate ϵ numerically by replacing the derivatives in Eq. (2.9) with finite differences. For a rectangular domain, the normal strain in the l -direction ($l = 1, 2, 3$) is

$$\epsilon_{mn} = \frac{L_l - L_l^{\sigma=0}}{L_l^{\sigma=0}} \quad (m = n = l) \quad (2.10)$$

where L_l and $L_l^{\sigma=0}$ are the domain's length in that direction, in the *current* and *undeformed* (“initial”) configuration, respectively. The undeformed configuration is defined here by the first appearance of appreciable stresses during compaction of a loose packing, see Section 2.7.2. In the simulations presented in this dissertation, only normal strains are applied, keeping the boundary walls orthogonal to each other. We use the convention of positive stress and strain in compression.

The parameter defined in Eq. (2.10) is the commonly used “engineering strain” [Rees, 2006]. Alternatively, replacing $L_l^{\sigma=0}$ in Eq. (2.10) with the value at the *reference* configuration, L_l^0 , such that the numerator, $dL_l = L_l - L_l^0$, is a small increment, $dL_l \ll L_l^0$, yields an approximation for the “logarithmic” or “natural” strain, dL_l/L_l^0 . While the natural strain is closer to the formal definition of strain as a differential quantity [Landau & Lifshitz, 1986], we use the engineering strain to compare with experimental data.

2.6.2 Stress

The average stress tensor, σ , is evaluated from the loads applied by the boundaries on the outermost grains. The normal stress at each boundary wall w is estimated from

the normal component of an equivalent external force, P_w^{ext} , divided by its area, A_w . The external normal force is calculated from the sum of the normal contact forces on the wall, $P_w^{ext} = \sum_{i=1}^{N_g^w} \|\mathbf{P}_{iw}\|$, where N_g^w is the number of grains in contact with boundary w . The normal stress in the l -direction is computed by averaging these quantities for the corresponding boundaries,

$$\sigma_{mn} = \frac{1}{2} \left(\frac{P_{w=l}^{ext}}{A_{w=l}} + \frac{P_{w=l+3}^{ext}}{A_{w=l+3}} \right) \quad (m = n = l) \quad (2.11)$$

To confirm the validity of Eq. (2.11), we compare with the averaged Cauchy stress [Christoffersen et al., 1981],

$$\langle \boldsymbol{\sigma} \rangle_{V_{tot}} = \frac{1}{V_{tot}} \sum_{ij=1}^{N_c} (\mathbf{f}_{ij} \otimes \mathbf{r}_{ij}) \quad (i \neq j) \quad (2.12)$$

where V_{tot} is the sample volume, N_c is the number of contacts in the pack, and \mathbf{f}_{ij} is the force exerted on grain i by grain j . To account for the interactions with the boundaries, we modify the expression in Eq. (2.12), obtaining

$$\langle \boldsymbol{\sigma} \rangle_{V_{tot}} = \frac{1}{V_{tot}} \sum_{i=1}^N \left[\sum_{j=1}^{N_g^i} \mathbf{f}_{ij} \otimes \mathbf{r}_{ij} + \sum_{w=1}^{N_b^i} \mathbf{f}_{iw} \otimes \hat{\mathbf{n}}_w (R_i - h_{iw}) \right] \quad (i \neq j) \quad (2.13)$$

If oblique forces are considered, as in the models presented in Chapters 3–4, \mathbf{f}_{ij} is computed from the sum of the normal and tangential force components. Here, only normal compressive forces are considered, and the expression in Eq. (2.13) reduces to

$$\langle \boldsymbol{\sigma} \rangle_{V_{tot}} = \frac{1}{V_{tot}} \sum_{i=1}^N \left[\sum_{j=1}^{N_g^i} \hat{\mathbf{r}}_{ij} \otimes \hat{\mathbf{r}}_{ij} \|\mathbf{P}_{ij}\| \|\mathbf{r}_{ij}\| + \sum_{w=1}^{N_b^i} \hat{\mathbf{n}}_w \otimes \hat{\mathbf{n}}_w \|\mathbf{P}_{iw}\| (R_i - h_{iw}) \right] \quad (i \neq j) \quad (2.14)$$

Here $\hat{\mathbf{r}}_{ij} = \mathbf{r}_{ij} / \|\mathbf{r}_{ij}\|$. The tensor products $\hat{\mathbf{r}}_{ij} \otimes \hat{\mathbf{r}}_{ij}$ and $\hat{\mathbf{n}}_w \otimes \hat{\mathbf{n}}_w$ are computed for all pairs of bodies in contact. Eq. (2.14) yields values similar to those obtained from Eq. (2.11).

2.6.3 Effective elastic moduli

We quantify the evolution of the bulk mechanical properties with the deformation by discretizing the load path and evaluating a set of constant effective elastic moduli for

each load interval. The moduli for each interval are evaluated by fitting each stress-strain interval with Hooke's law. Hooke's law for a homogenous, isotropic medium is

$$\boldsymbol{\sigma} = \lambda \text{tr}(\boldsymbol{\epsilon}) \hat{\mathbf{I}} + 2G\boldsymbol{\epsilon} \quad (2.15)$$

where $\boldsymbol{\sigma}$ is the stress tensor, $\text{tr}(\boldsymbol{\epsilon})$ is the trace of the strain $\boldsymbol{\epsilon}$, and $\hat{\mathbf{I}}$ is a second order unit tensor. The moduli λ and G are Lamé's coefficient and the shear modulus, respectively. Other elastic moduli can be evaluated from λ and G [Landau & Lifshitz, 1986].

The values evaluated from Eq. (2.15) represent the bulk-averaged moduli of an effective homogeneous and isotropic elastic medium. The moduli evaluated for isotropic medium using different pairs of directions² are similar. However, the material response can become anisotropic if: (a) the loading is highly anisotropic [Johnson et al., 1998]; and (b) if the pack's size is too small [Goldenhirsch & Goldenberg, 2005]. To avoid anisotropy, we: (a) apply relatively isotropic loads; and (b) construct packs with sides not smaller than ~ 15 grain diameters. The degree of loading isotropy required to maintain isotropic response depends on the size of the pack, as well as the grain properties and their spatial arrangement, and was determined by trial and error. By taking these measures, the moduli computed in different directions are practically identical.

2.6.4 Porosity

Porosity is the volumetric fraction of the pore space relative to the total volume of the sample. To compute the porosity we approximate the shape of each pair of deformed grains, i and j , by two overlapping spheres. The intersection of their surfaces defines a disk of radius ρ_{ij} [Harris & Stocker, 1998],

$$\rho_{ij} = \frac{1}{2r_{ij}} [(R_i - R_j - r_{ij})(-R_i + R_j - r_{ij})(R_i + R_j - r_{ij})(R_i + R_j + r_{ij})]^{1/2} \quad (2.16)$$

Here $r_{ij} = \|\mathbf{r}_{ij}\|$. The solid volume of the deformed pair is computed by subtracting the overlapping region, the volume of two spherical caps, from the total volume of the two spheres, $4\pi (R_i^3 + R_j^3) / 3$, see Figure 2.4. The volume of the spherical cap associated with

²In polyaxial loading, there are three possible combinations (pairs) from which the moduli can be evaluated, whereas in uniaxial (triaxial) loading there are only two.

sphere i is

$$V_{ij}^{cap} = \frac{\pi}{6} (R_i - \|\mathbf{R}_{ij}\|) \left[3\rho_{ij}^2 + (R_i - \|\mathbf{R}_{ij}\|)^2 \right] \quad \text{for grain-grain contact} \quad (2.17a)$$

$$V_{iw}^{cap} = \pi h_{iw}^2 \left(R_i - \frac{h_{iw}}{3} \right) \quad \text{for grain-boundary contact} \quad (2.17b)$$

where the radius-vector

$$\mathbf{R}_{ij} = -\hat{\mathbf{r}}_{ij} (R_i^2 - \rho_{ij}^2)^{1/2} \quad (2.18)$$

connects the center of grain i to the initial contact point with another grain j . The total solid volume in the sample is computed by subtracting the sum of volumes of all spherical caps, from the total volume of all spheres (undeformed shapes). Thus, the porosity is

$$\phi = 1 - \frac{1}{V_{tot}} \sum_{i=1}^N \left[\frac{4}{3} \pi R_i^3 - \sum_{j=1}^{N_g^i} V_{ij}^{cap} - \sum_{w=1}^{N_b^i} V_{iw}^{cap} \right] \quad (2.19)$$

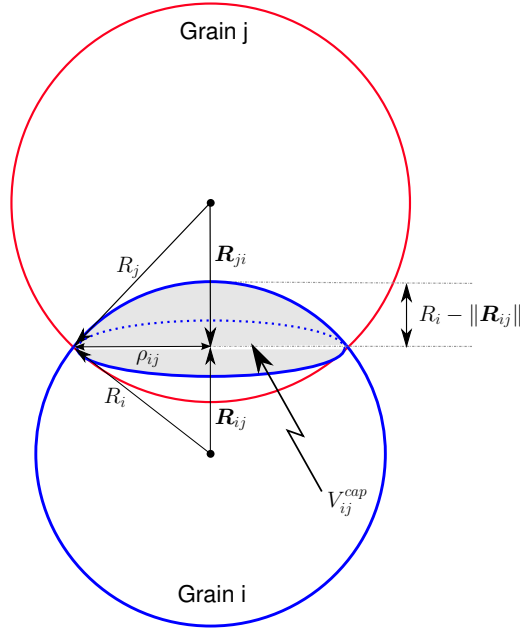


Figure 2.4: Schematic description of a pair of grains in contact, used in estimating the porosity. The solid volume of a deformed grain i is evaluated by subtracting the volume of a spherical cap V_{ij}^{cap} (shaded) from the undeformed spherical volume.

2.7 Simulation results

2.7.1 Grain properties

In simulations, we assign the grain properties from published experiments. To model heterogenous materials such as elastic sediments, we assign the grains radii from a uniform distribution³, and elastic moduli of the grain material from a normal distribution, see, e.g., Figure 2.5. We model three types of grains: (a) quartz sand, (b) glass beads, and (c) methane-hydrates. Table 2.1 lists the numerical values for each material, borrowed from (a) Yong & Warkentin [1975] and Domenico [1977]; (b) Domenico [1977] and Makse et al. [1999]; and (c) Guerin [2000]. In Table 2.1, \bar{E} , $\bar{\nu}$, \bar{K} , and \bar{G} denote the mean values of Young’s modulus, Poisson’s ratio, bulk and shear modulus, with bar denoting their arithmetic mean, and *s.d.* their standard deviation. To minimize the deflections of the walls, they are assigned stiffer elastic moduli, $E_w = 100\bar{E}$ and $\nu_w = 0.495$. The sample’s name provides the grain type and quantity: for instance, *G5036* denotes a pack of 5036 glass beads.

Table 2.1: Numerical values of grain properties used in simulations. See text for sources.

| | Quartz sand | Glass beads | Methane-hydrates |
|-------------------------------|-------------|-------------|------------------|
| R_i (mm) | 0.07–0.13 | 0.07–0.13 | 0.07–0.09 |
| ρ_i (g/cm ³) | 2.65 | 2.42 | 0.9 |
| \bar{E} (GPa) | 100 | 70 | 6.6 |
| $\bar{\nu}$ | 0.15 | 0.2 | 0.32 |
| \bar{K} (GPa) | 47.6 | 38.9 | 6.1 |
| \bar{G} (GPa) | 43.5 | 29.2 | 2.5 |
| <i>s.d.</i> | 0.1 | 0.1 | 0 |

2.7.2 Initial pack

In analogy with the initial conditions required in a dynamic model, our quasi-static formulation requires specification of a reference configuration of the grains and the boundaries at the beginning of each load increment. In particular, simulations require a

³Note that the sample generation procedure involves grain expansion, which results in a slight deviation from the originally uniform distribution, see Section 2.7.2.

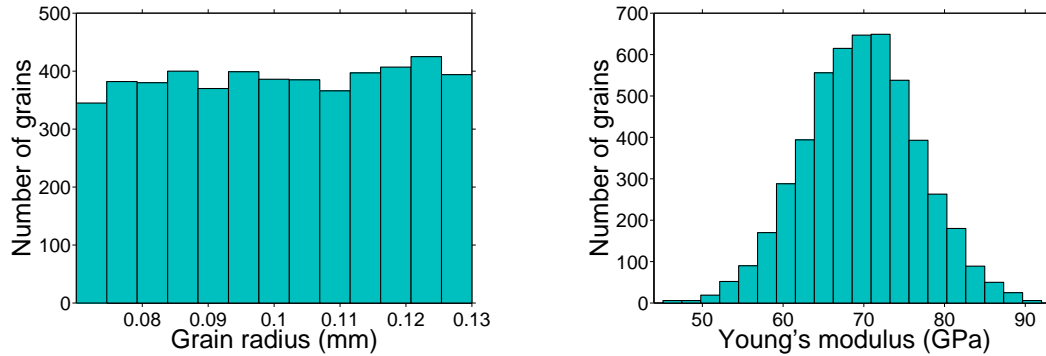


Figure 2.5: The distribution of grain sizes (left) and Young's modulus (right) for a sample of 5036 glass beads, denoted by *G5036*.

sufficiently dense, irregular initial equilibrium configuration [O'Sullivan, 2002; Bagi, 2005]. Here, we describe a procedure to generate such initial configuration, using QuSGM.

The procedure starts with a loose irregular arrangement. Here, a loose arrangement is obtained by selecting a portion of a large pack generated using DEM simulations by Jin [2006]. Planar boundaries are placed around the selected portion, removing all grains which are intersected by these boundaries. The simulations by Jin [2006] were performed to model sedimentation, letting the grains settle under gravity until their velocities vanish. At this stage, the coordination number of about 55% of all grains within the selected portion and 45% of the interior grains is less than four, which means they are not in stable mechanical equilibrium⁴. Interior grains are defined by a distance from the boundaries greater than the maximum grain diameter. The larger number of unstable grain near the boundaries may be a consequence of removing the grains intersected by the boundaries.

Next, the packing density is increased by isotropic compaction of the domain, and expansion of unstable grains. Grain expansion is performed since moving only the boundaries may be insufficient to eliminate unstable grains. To increase stability of the pack, we expand unstable grains until they contact at least 4 other grains, where each contact is in minimal compression⁵ defined by $h_{ij} \geq 10^{-5} \bar{R}$. Here, \bar{R} is the arithmetic mean of the grain radii. Then, an equilibrium configuration is sought using our QuSGM model with frictionless contacts. This process is repeated until the coordination number of most grains satisfies $N^i \geq 4$, and appreciable contact forces develop. The confining stress

⁴Jin [2006] produced denser packings by simulating compaction.

⁵The minimal value of h_{ij} was determined by trial and error.

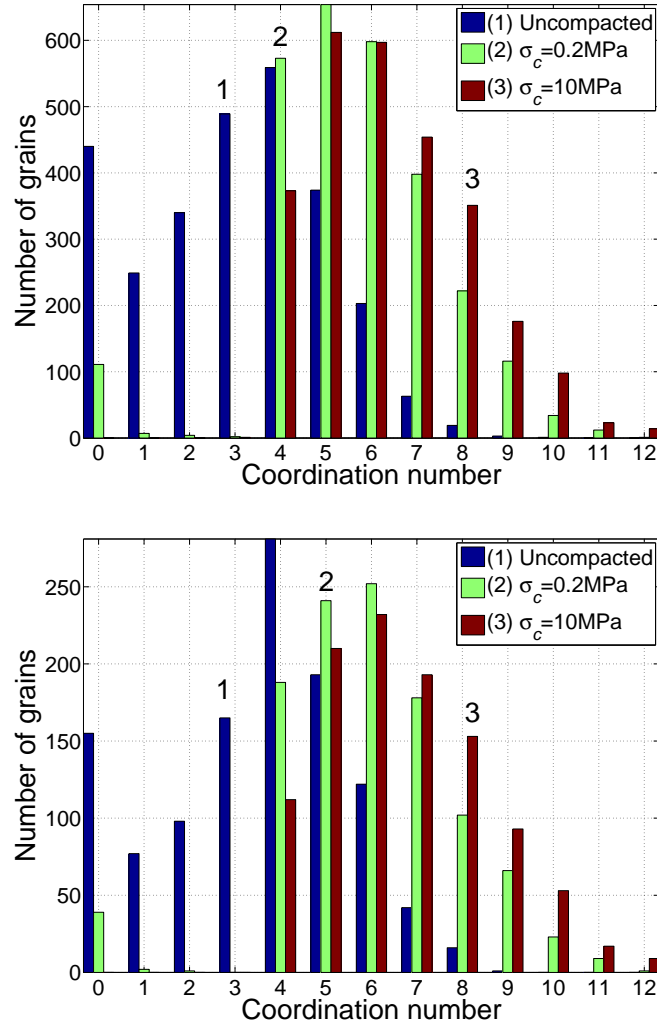


Figure 2.6: The distribution of the coordination number, N^i , of all grains (top) and of the interior grains only (bottom), at different stages of the generation procedure of sample *Q2699*: (1) initial, uncompacted pack selected from DEM simulations of settlement under gravity by Jin [2006]; (2) following isotropic compaction to low stresses of $\sigma_c = 0.2 \text{ MPa}$; and (3) following further compaction to $\sigma_c = 10 \text{ MPa}$, shown for comparison. Compaction was simulated by our QuSGM model with frictionless contacts.

at the end of this process is denoted by $\sigma_c^{\mu=0}$. Note that complete elimination of unstable grains may not be possible because of grain size variations: the opening between large grains can be large enough to contain a small grain, not in stable equilibrium [Thornton & Antony, 1998]. Such “floating” grains are believed to exist in natural sediments [Potyondy & Cundall, 2004].

We demonstrate evolution of the packing density through the coordination number. The distribution of the coordination number of all grains and of the interior grains only is given in Figure 2.6, for different stages of the sample generation procedure: (1) initial, uncompacted pack selected from DEM simulations of settlement under gravity by Jin [2006]; (2) following isotropic compaction to low stresses of $\sigma_c=0.2$ MPa; and (3) following further compaction to $\sigma_c=10$ MPa, shown for comparison. The confining stress, σ_c , is defined by $\sigma_c = \text{tr}(\boldsymbol{\sigma})/3$.

Note that we do not simulate here a deposition process, in which grain collisions are important [Jin, 2006]. Otherwise, the use of QuSGM provides a dense arrangement in static equilibrium with a smaller computing effort than using dynamic algorithms, cf. Section 1.3.3.2.

2.7.3 Model verification

Verification is a crucial stage in the development of a model. A numerical computational technique is physically-sound and has predictive capabilities only if: (1) the numerical scheme is stable and accurate; (2) the mathematical model adequately represents the underlying physical phenomena; and (3) the physical properties are modeled by parameters with clear physical meaning, that can be measured in an experiment.

Accuracy of a numerical solution can be evaluated by comparison with an exact, analytical solution. Yet, for an irregular, heterogenous domain such as a random packing of grains, exact solutions are not available. Thus, we test our numerical algorithm for an idealized problem of a structured packing undergoing self-similar deformations, see Section 2.7.3.1.

However, data from structured arrangements do not provide a comprehensive verification of the model, since a regular pack deforms differently than an irregular one [O’Sullivan, 2002; Bagi, 2003]. In addition, a regular packing is uncommon in natural materials, and is extremely difficult to produce in a laboratory; even an initially structured packing may distort under deformation because of inevitable material and geometrical heterogeneities [O’Sullivan, 2002]. For these reasons, we verify our model for an irregular packing by comparing our predicted effective elastic moduli with experimental data and EMT computations, see Section 2.7.3.2. In these experiments, artificial grains (glass beads) were used, reducing the uncertainty involved in the estimation of the grain properties.

2.7.3.1 Accuracy of the numerical algorithm

Few closed-form solutions exist for the deformation of a structured packing of identical grains caused by a small perturbation, see, e.g., Duffy & Mindlin [1957], Deresiewicz [1958b], Duffy [1959] and Thurston & Deresiewicz [1959]. However, the numerical error may grow with the size of the macroscopic strain. Thus, we test our numerical algorithm in the case of large deformations of a small structured packing. To allow analytical solution we preserve the symmetric structure by imposing self-similar deformations.

A pack of five identical grains whose centers form a pyramid, is deformed by shrinking all distances between the grain centers uniformly, see Figure 2.7. The distance between the centers of a pair of grains, r_{ij} , reduces to $(1 - \varepsilon)r_{ij}$. We compute analytically the intergranular forces from the given grain displacements, using Eq. (2.2). The contact network and force directions remain constant. Due to symmetry, it suffices to evaluate the forces at one of the four contacts between the bottom grains, in addition to the force between the top grain and a bottom grain. The pack is bounded by planar boundary walls. The boundary displacements required to simulate self-similar deformation are computed from the force balance equations.

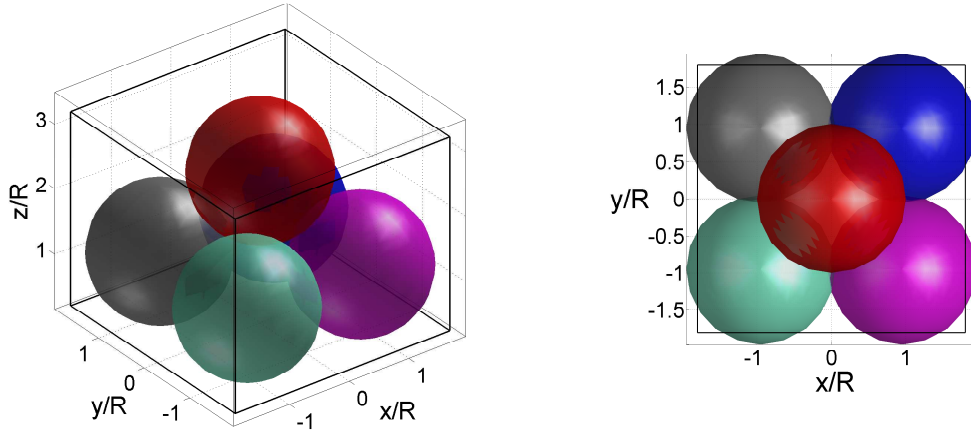


Figure 2.7: A structured five-grain pack used to evaluate the performance of our numerical algorithm. The figure shows (a) three-dimensional view (left plot); and (b) planar x-y view (right) of the deformed pack. Starting with an initial pack with adjacent grains merely touching each other, the plots show the result of self-similar deformation with strain of $\varepsilon=0.05$.

The accuracy of the numerical result is evaluated by comparing the numerically-computed distance between the top grain and a bottom grain, r_{ij}^N , with the analytical result, r_{ij}^A . Figure 2.8 shows the relative error, $(r_{ij}^A - r_{ij}^N)/r_{ij}^A$, vs. the strain factor, ε .

The relative error decreases with the size of the strain. In the simulations, symmetry for the bottom grains was preserved: the difference between the length of the centerline connecting each pair of adjacent bottom grains was of the order of the machine's floating-point relative accuracy⁶.

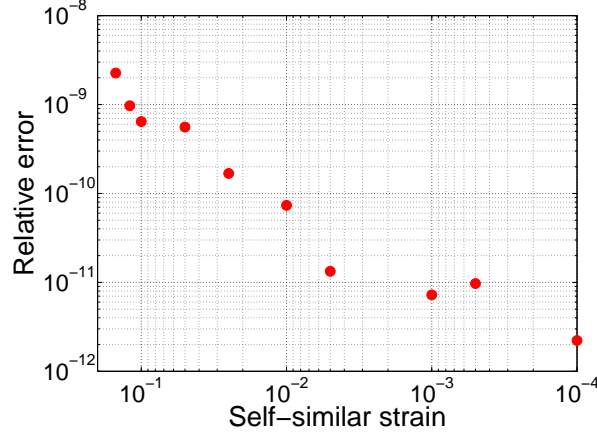


Figure 2.8: The relative error of numerical solution, $(r_{ij}^A - r_{ij}^N) / r_{ij}^A$, vs. the self-similar strain factor, ε , for a five-grain pack undergoing self-similar deformations. The error is evaluated by comparison to an analytical solution.

2.7.3.2 Verification against experimental data

To verify our model against experiments we simulate uniaxial compression of a sample of glass beads, *G5036*. The moduli computed from these simulations are plotted in Figure 2.9 vs. confining stress, σ_c . Also presented are data from acoustic experiments on glass beads with material properties similar to those used in our simulations, and the following grain radii (in mm): (1) 0.035–0.045 [Domenico, 1977]; (2) 0.023 [Makse et al., 1999]; and (3) 0.10–0.15 [Yin, 1993], with unspecified distributions. Finally, we present the results of DEM simulations and EMT computations by Makse et al. [1999], using a contact model that prohibits sliding. In the DEM simulations, radii were equally distributed between 0.095 and 0.105 mm, whereas for the EMT predictions a uniform grain diameter of 0.10 mm was assumed [Makse et al., 1999]. The experimental values of the elastic moduli were evaluated from the acoustic compressional (v_p) and shear (v_s) velocities by using the

⁶The floating-point relative accuracy on the desktop used in our simulations was 2^{-52} .

following relations, valid for a planar wave in an infinite medium [Makse et al., 2004]

$$v_p = \sqrt{\frac{K + \frac{4}{3}G}{\rho_b}} \quad (2.20a)$$

$$v_s = \sqrt{\frac{G}{\rho_b}} \quad (2.20b)$$

where ρ_b is the bulk density of the sample. The numerical values of the moduli from Yin [1993] and Makse et al. [1999] have been obtained by digitizing Figure 1 in Makse et al. [1999]. The data from Domenico [1977] is computed from the velocities reported by the author.

Our bulk modulus estimates are in good agreement with the experimental data, with values slightly lower than the data. In addition, at confining stresses higher than ~ 2 MPa, the evaluated growth rate of the shear modulus agrees with the data. At the same time, our model strongly underestimates the reported shear modulus values. In particular, the evaluated shear modulus drops sharply at low stresses, predicting loss of shear rigidity as the mean coordination number approaches 6 and the porosity exceeds $\sim 37\%$. We associate the discrepancy between our predictions and the data with the assumption of frictionless contacts. Unlike the bulk modulus, the shear modulus greatly depends on intergranular shear forces. For example, DEM simulations shows that loss of rigidity is predicted at lower packing densities when friction is accounted for [Makse et al., 2004].

Our simulations show a decrease in the rate of moduli growth with confining stress, from a power law of $\sigma_c^{0.45}$ to $\sigma_c^{0.33}$. This transition, while observed in experiments and justified by theory, is not predicted by the EMT in Walton [1987]. The discrepancy between the EMT predictions and experimental data is discussed in Goddard [1990], Makse et al. [1999, 2004], Pride [2005] and the references therein. Our model provides additional theoretical justification. Increasing the confining stress increases both the packing density and stiffness, while decreasing their growth rates. The dependence of the packing density on σ_c is intuitive: as the pack becomes denser, further compaction becomes more difficult. The relation between the contact stiffness and σ_c can be predicted from the Hertzian contact law (cf. Eq. (2.2)): the normal contact stiffness is the derivative of the force, $\|\mathbf{P}_{ij}\|$, with respect to the deformation, h_{ij} , where the latter is, on average, directly related to the confining stress. The growth rate of the normal stiffness is proportional to the second derivative of $\|\mathbf{P}_{ij}\|$, with a power law of $(h_{ij})^{-1/2}$ which indicates a reduction in growth rate of the stiffness with increasing σ_c .

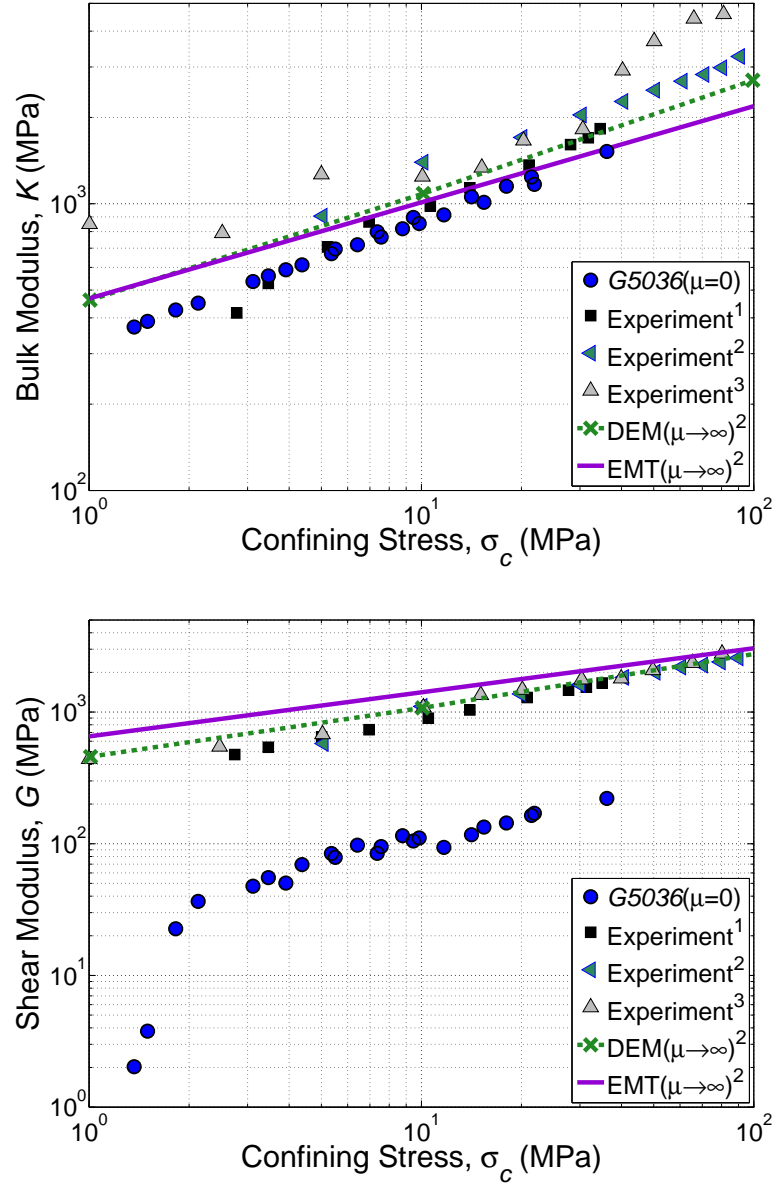


Figure 2.9: The effective bulk (K , top) and shear (G , bottom) modulus *vs.* confining stress, σ_c . The moduli evaluated from simulations using our frictionless model are compared with the results of acoustic experiments in glass beads, as well as DEM and EMT computations. Superscripts 1–3 refer to the data published in Domenico [1977], Makse et al. [1999], and Yin [1993], respectively.

2.7.4 Micromechanical analysis

In Section 1.1.1, the importance of the micromechanical evidence and the relation between the meso- and macro-scale was discussed. Here, the presented analysis demon-

strates mechanisms responsible for the inelastic response typical of granular materials.

2.7.4.1 Hysteresis, strain hardening and fluctuations in the contact network

Upon applying external loading to a granular pack, the loads are distributed in a highly heterogeneous manner: most of the load is carried by relatively few grains, that create “force chains”. Force chains have been observed in experiments, see Oda et al. [1982], Behringer et al. [1999], Majmudar & Behringer [2005], Goldenhirsch & Goldenberg [2005] and the references therein, and simulations, e.g. Radjaï et al. [1996], Thornton & Antony [1998], Peters et al. [2005], Makse et al. [2004], Muthuswamy & Tordesillas [2006], Peña et al. [2008], and Tordesillas [2007]. In our simulations, we observe force chains by tracking the contact forces larger than a certain threshold.

Heterogeneity with regard to the intergranular forces is a source of intrinsic unpredictability for granular systems. This is because even small perturbations, for instance small displacements of the grains, can alter these force chains significantly [Behringer et al., 1999]. Fluctuations in the force chains can lead to large variations in the overall response; for example, in the form of stress drops [Tordesillas, 2007; Peña et al., 2008] or changes in the frequency response of waves propagating through the medium, see Behringer et al. [1999] and the references therein. These fluctuations are often associated with frictional resistance and slip (“stick-slip”) between grains [Behringer et al., 1999; Duran, 2000].

Here, we demonstrate that stick-slip is not the only source for fluctuations. In the absence of frictional slip, our simulations show correspondence between abrupt changes in the slope of the stress-strain curve and substantial variations in the contact force network, see Figures 2.10–2.11. Some of these variations are irreversible, leading to hysteretic bulk response. Tracking hysteresis *via* grain-scale parameters can be done quantitatively using the fabric tensor [Liou & Pan, 2003]. Qualitatively, we observe that these noticeable variations are correlated with relatively large displacements experienced by several grains, corresponding to strain localization [Bagi, 2006]. These displacements are possible at particular combinations of contact forces and geometry, as grains are “pushed” through constrictions. Following such events, the local sets of contacts and the shapes of these constrictions are altered significantly, so that a reverse-perturbation of the boundary conditions cannot restore the original configuration. In loading, grain rearrangements lead to convex stress-strain curve, which we interpret as strain hardening, see Figure 2.10.

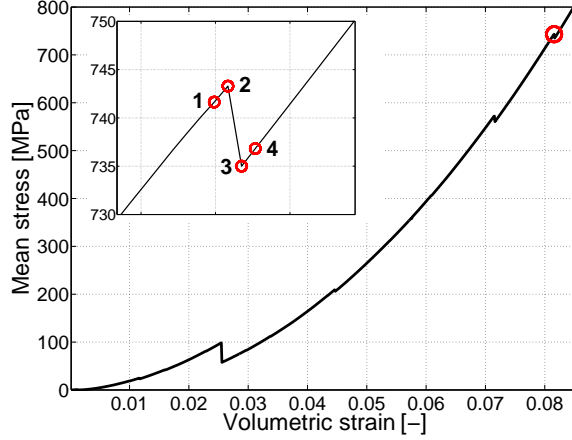


Figure 2.10: Mean stress, σ_c , vs. volumetric strain, $\epsilon_v = \text{tr}(\epsilon)$, in simulations of isotropic loading on sample *Q306*. Increasing slope corresponds to strain-hardening. Several stress drops are evident. The top-left corner of the plot shows a zoom into one of these stress drops (encircled), highlighting four consecutive configurations (marked by 1–4). The force chains and grain displacements within these four configurations are plotted in Figure 2.11.

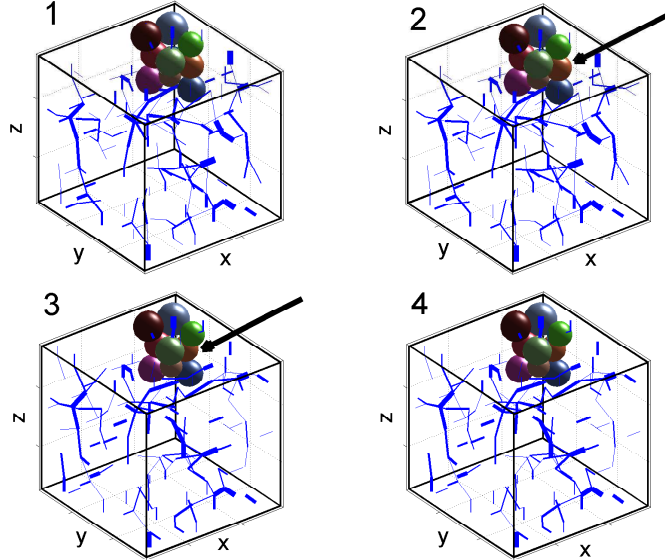


Figure 2.11: Consecutive snapshots showing abrupt change of microstructure. Sample *Q306* is loaded by incremental isotropic strain of $\Delta\epsilon=5 \cdot 10^{-5}$. For each configuration (1–4), we plot a cluster of grains, and the force chains defined by $\tau_{FC}=0.1$, where the line width is proportional to their magnitude. Note the abrupt change from 2→3, e.g. in the position of the brown grain (see arrow), which corresponds to the stress drop highlighted in Figure 2.10.

To visualize an abrupt change of microstructure, we plot several grains and the force chains in four consecutive configurations, following isotropic loading with strains

increments of $\Delta\epsilon=5 \cdot 10^{-5}$ on sample *Q306*, see Figure 2.11. The plot shows the largest contact forces that fall within a certain percentile, τ_{FC} ; for instance, $\tau_{FC}=0.1$ correspond to the largest 10% forces. While the strain increments are small enough so that changes between configurations 1 and 2 as well as 3 to 4 are unnoticeable, an abrupt change between configurations 2 and 3 is evident both in the force chains and the positions of the grains. For instance, the large displacement of the brown grain (see arrow) corresponds to the stress drop highlighted in Figure 2.10. These rare “jumps” events, in which a grain moves significantly more than others, have been observed in experiments on glass beads, and were found to have a significant effect on the macroscopic properties [Ribi re et al., 2005].

To demonstrate the hysteretic macroscopic response which results from the aforementioned microstructural variations, we simulate a polyaxial loading-unloading cycle on sample *Q2654*, see Figure 2.12. In loading, an event in which several grain “jumps” occur, corresponding to a stress drop, is encircled. During unloading, this event is not reversed, and the unloading stress-strain curves deviate from the ones in loading.

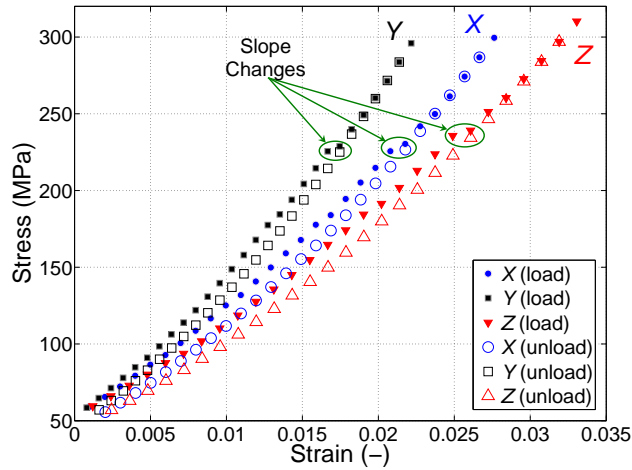


Figure 2.12: Stress-strain curves obtained from simulating a polyaxial loading-unloading cycle on sample *Q2654*. Hysteresis, evident as different loading and unloading stress-strain curves, is correlated to a rare event of grain “jumps” which is marked by an abrupt change in the slopes of the curves (encircled).

2.7.4.2 Stress-induced anisotropy

Recent studies have suggested that anisotropy plays an important role in granular mechanics, see Oda et al. [1998] and the references therein. Anisotropy can be induced when

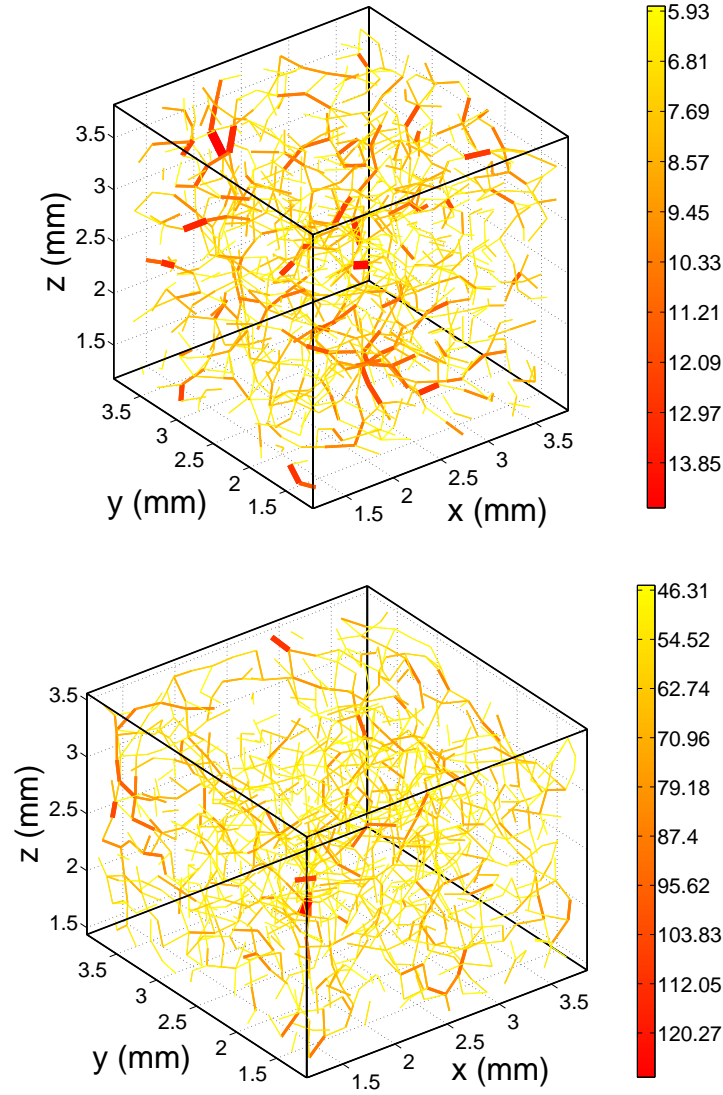


Figure 2.13: Development of stress-induced anisotropy shown as a change in directions of the largest contact forces. Forces are plotted with line width and color corresponding to their magnitude. The color bar shows the force magnitudes, in N. Two configurations of sample *Q2654* are shown, under: (a) isotropic loading (top plot); and (b) anisotropic loading (bottom). The percentage of forces in the axial (vertical) direction increases from 28% to 37%, while the expected value for a uniform distribution is 29%.

the material is subjected to anisotropic loading, e.g. shear distortion [Oda et al., 1982, 1998; Johnson et al., 1998]. In general, grain angularity can be a source of anisotropy, regardless of the state of stress, associated with the anisotropic contact network [Oda et al., 1998]. Stress-induced anisotropy was observed in our simulations. To investigate the underlying mechanisms, we analyze the directions of the largest contact forces. In Figure 2.13 we plot

the force chains defined by $\tau_{FC} = 0.1$ for two configurations of sample *Q2654*, under: (a) isotropic stress of 0.11 GPa; and (b) anisotropic load with axial and lateral stresses of 1.39 and 1.28 GPa, respectively. The axial load was applied in the vertical direction, along the z axis. To quantify the change in force directions, we compute the number of forces which are directed between 45–90 degrees of the horizontal (x-y) plane.

The percentage of forces that fall inside the vertical cone defined by the above angles increases from 28% in configuration (a) to 37% in (b), where the percentage for a uniform distribution is 29%. Thus, while under isotropic loads the force directions are uniformly distributed, under anisotropic loads they are preferentially aligned with the main loading direction. Similar observations were made in experiments [Oda et al., 1982, 1998; Majmudar & Behringer, 2005] and simulations [Thornton & Antony, 1998]. Macroscopically, while the moduli evaluated for different directions are similar in (a), they differ by several percents in (b), indicating a macroscopically anisotropic response.

2.8 Concluding remarks

We have studied the micromechanics of cohesionless granular materials, namely the relations between the grain- and the macro-scale. A quasi-static micromechanical model has been formulated and implemented within numerical simulations, using a variational approach. A granular sample is modeled as a 3D disordered pack of elastic spherical grains, loaded by incremental displacements of its boundaries. Interactions among the grains are modeled through the contact theory of Hertz [1882]. Each equilibrium configuration is found by minimizing the total potential energy of the pack, using a modified conjugate gradient algorithm. The macroscopic stress, strain and effective moduli are computed from the intergranular forces and the deformation of the pack. Our approach, termed QuSGM, yields an efficient computational procedure, which is also used to generate a dense initial arrangement.

We have verified our model against published experimental data, using similar grain properties. Our model requires only few material parameters, which are obtained from published experiments. The good agreement between predicted and measured values of the effective bulk modulus, achieved with no adjustments of parameters, demonstrates the physical soundness of our model.

By micromechanical analysis, we describe mechanisms responsible for hysteresis,

strain hardening, and stress-induced anisotropy. In particular, we show that variations in the contact force network lead to irreversible changes in grain configurations. Microscopically, these changes correspond to infrequent “jump” events in which few grains move significantly more than others. Macroscopically, these variations correspond to large fluctuations in the stress-strain relations, and thus have significant effect on the bulk properties. Our observations are supported by experimental evidence [Oda et al., 1998; Behringer et al., 1999; Ribière et al., 2005; Majmudar & Behringer, 2005; Tordesillas, 2007; Peña et al., 2008]. The sensitivity of mechanical properties of granular materials to small perturbations in grain configurations poses a challenge in predicting these properties [Behringer et al., 1999]. The results of our simulations are a step towards better understanding of granular mechanics, and consequently the ability to predict their behavior.

Our results confirm that the bulk modulus mainly depends on the normal contact forces [Thornton, 2000; Kruyt & Antony, 2007], and that grain-scale elasticity is suitable to describe many features of the inelastic response of granular materials [Goldenhirsch & Goldenberg, 2005]. While our model supports the idea that microscopic friction is not the sole mechanism of macroscopic shear resistance [Peña et al., 2008], it underestimates the shear modulus, predicting loss of shear rigidity at packing densities higher than those experimentally observed. We attribute this deficiency to the assumption of frictionless grains. In Chapter 3, the current model is extended to account for shear and sliding at the contacts, allowing for more accurate predictions of the moduli.

Chapter 3

A granular pack model with intergranular friction

3.1 Introduction

THE RESULTS of the previous chapter demonstrate that modeling granular matter as a collection of elastic grains results in inelastic bulk response. Moreover, by assuming ideally-smooth grains we have shown that microscopic friction is not the sole mechanism of macroscopic shear resistance [Peña et al., 2008]. Nevertheless, this assumption leads to an underestimation of the macroscopic stiffness, mostly the shear modulus. In this chapter, we extend the model presented in Chapter 2 to account for the effect of friction.

Friction resists relative displacements and rotations of the grains, through forces and moments (“frictional loads”) at the contact interfaces. Modeling the effect of friction is challenging, because of energy dissipation associated with slip between the grains. Dissipation makes the force-displacements relations at each contact path-dependent. To model deformation of a pack of grains within the framework of QuSGM, we introduce a set of incrementally path-independent constitutive rules, based on the contact theories of Hertz, Mindlin and Deresiewicz. Employing a variational approach, a sequence of equilibrium configurations is computed by minimizing the work against the intergranular loads performed within each load increment.

In the first part of this chapter, Sections 3.2–3.5, we formulate the mathematical model. The characterization of a grain pack, including its microstructure, material properties and boundaries is given in Section 3.2. In Section 3.3 we present the constitutive rules which govern the intergranular interactions. In Section 3.4, we provide the methodol-

ogy to obtain the equilibrium configurations. The definition of the macroscopic stress and strain is discussed in Section 3.5. The second part of this chapter, Section 3.6, presents the simulation results. First, the values of model parameters, taken from published experiments, are specified in Section 3.6.1. The generation procedure for the initial packing, namely the introduction of intergranular frictional loads, is discussed in Section 3.6.2. In Section 3.6.3, the numerical accuracy and the physical soundness of our model are demonstrated by comparing its predictions with analytical solution and experimental data. The sensitivity analysis presented in Section 3.6.4 shows our model's robustness with respect to the size of the incremental load steps, and quantifies the effect of the initial packing and the intergranular friction coefficient. Finally, Section 3.7 gathers the main conclusions of the chapter. Important results from this chapter have been published in Holtzman et al. [2008a].

3.2 Modeling a pack of grains

3.2.1 Microstructure

The current description of a grain pack follows concepts similar to those delineated in Section 2.2: a granular sample is modeled through irregularly-packed spherical grains. The grains are linearly-elastic, undergoing small and localized deformations. The geometry of the pack is characterized by the grain radii and center coordinates. Additionally, determination of the frictional contact loads requires tracking the grain rotations. Given the grain properties and the intergranular loads at a reference configuration, a pack of N grains has $6N$ degrees of freedom: the grains displacements and rotations.

We denote the displacement and rotation of grain i ($i = 1, 2, \dots, N$) by \mathbf{u}_i and $\mathbf{\Omega}_i$, respectively. We use the right-hand convention, where $\mathbf{\Omega}_i$ denotes the rotation of grain i by an angle $\|\mathbf{\Omega}_i\|$, around an axis passing through the grain's center and directed along $\mathbf{\Omega}_i$. To make the units of all variables uniform, the rotation of each grain is multiplied by its radius, R_i . Our variables are written as a vector of generalized coordinates, $\boldsymbol{\theta} = [\mathbf{u}_1 \dots \mathbf{u}_N \quad \mathbf{\Omega}_1 R_1 \dots \mathbf{\Omega}_N R_N]^T$, where \mathbf{u}_i and $\mathbf{\Omega}_i$ are row vectors.

3.2.2 Microscopic material properties

In addition to the parameters described in Section 2.2, introduction of friction requires specification of the static coefficient of friction between the grains, μ_{ij} . While the grain's radius R_i , density ρ_i , and, to some extent, elastic moduli, E_i and ν_i , can be readily evaluated from experiments, the intergranular friction coefficient is not a well-defined parameter [Pohlman et al., 2006]. The difficulty in estimating the value of μ_{ij} stems from the fact that intergranular frictional resistance depends on several parameters, such as grain surface roughness, contact area, and velocity, as well as molecular interactions [Li et al., 2005]. As a result, the friction coefficient may vary with the deformation, and with the type of experiment from which it is obtained [Pohlman et al., 2006]. In addition, for a small contact area, such as that between slightly deformed spherical grains, the applicability of Coulomb's law of friction is questionable [Li et al., 2005].

3.2.3 Boundary conditions

Kinematic boundary conditions are prescribed in a manner similar to that in Section 2.3, through the displacements of planar solid walls which interact with the outermost grains in the pack. The interactions between these grains and the boundaries include the effect of friction, through frictional loads.

3.3 Intergranular interactions: inelastic contacts

In this section, we formulate the constitutive rules that govern the intergranular interactions, relating the forces and moments to the relative displacements and rotations between the grains. These rules are based on the contact theories of Hertz [1882], Mindlin & Deresiewicz [1953] and Deresiewicz [1954].

3.3.1 Normal contact forces

At each contact, we resolve the contact force into normal and tangential components. Following Mindlin & Deresiewicz [1953], we assume that the normal component is unaffected by other load components [Johnson, 1987; Dintwa et al., 2008], and determine the normal force using the Hertzian model, cf. Section 2.4.

3.3.2 Tangential contact forces

Intergranular friction resists relative lateral displacements and rotations of two grains in contact through a shear (“tangential”) load at the contact interface. In this section, we present a contact model to determine the tangential force, based on the theory by Mindlin & Deresiewicz [1953].

Consider a reference configuration with a pair of grains in contact, i and j . Grain i is loaded by a shear force, \mathbf{Q}_{ij}^0 , acting tangentially to the contact plane, and a normal force, \mathbf{P}_{ij}^0 , see Figure 3.1(b). We assume that a small perturbation of the boundary conditions causes small linear and angular grain displacements. These displacements correspond to a relative tangential displacement of grain i with respect to j , $\mathbf{u}_{ij(s)}$. The perturbed tangential force, \mathbf{Q}_{ij} , is calculated by adding an increment to the unperturbed value,

$$\mathbf{Q}_{ij} = \mathbf{Q}_{ij}^{0,p} - k_{ij(s)} \mathbf{u}_{ij(s)} \quad (3.1)$$

Here $k_{ij(s)}$ denotes the shear resistance (“stiffness”) of that contact. Following Walton [1993], we account for the reorientation of the contact interface by projecting the force \mathbf{Q}_{ij}^0 onto the current contact plane by $\mathbf{Q}_{ij}^{0,p} = \|\mathbf{Q}_{ij}^0\| \hat{\mathbf{t}}_{ij}$, see Figure 3.1(b). The unit vector $\hat{\mathbf{t}}_{ij} = \mathbf{T}_{ij} \mathbf{Q}_{ij}^0 / \|\mathbf{T}_{ij} \mathbf{Q}_{ij}^0\|$ characterizes the direction of the projected force, where $\mathbf{T}_{ij} = \hat{\mathbf{I}} - \hat{\mathbf{r}}_{ij} \otimes \hat{\mathbf{r}}_{ij}$. For a contact with a boundary w , $\mathbf{T}_{iw} = \hat{\mathbf{I}} - \hat{\mathbf{n}}_w \otimes \hat{\mathbf{n}}_w$. The relative tangential displacement, $\mathbf{u}_{ij(s)}$, is

$$\mathbf{u}_{ij(s)} = \mathbf{T}_{ij}(\mathbf{u}_i - \mathbf{u}_j) + \boldsymbol{\Omega}_i \times \mathbf{R}_{ij} - \boldsymbol{\Omega}_j \times \mathbf{R}_{ji} \quad \text{for grain-grain contact} \quad (3.2a)$$

$$\mathbf{u}_{iw(s)} = \mathbf{T}_{iw}(\mathbf{u}_i - \mathbf{u}_w) + \boldsymbol{\Omega}_i \times \mathbf{R}_{iw} \quad \text{for grain-boundary contact} \quad (3.2b)$$

where \times denotes the vector product, and

$$\mathbf{R}_{ij} = -\hat{\mathbf{r}}_{ij} (R_i^2 - \rho_{ij}^2)^{1/2} \quad \text{for grain-grain contact} \quad (3.3a)$$

$$\mathbf{R}_{iw} = -\hat{\mathbf{n}}_w (R_i - h_{iw}) \quad \text{for grain-boundary contact} \quad (3.3b)$$

are radius-vectors connecting the center of grain i to the center of the contact area with another grain j or a boundary w , see Figure 3.1(a). The parameter ρ_{ij} is defined in Eq. (2.16).

If slip occurs between the contact interfaces, the force-displacement relation becomes path-dependent [Mindlin & Deresiewicz, 1953]. In the model by Mindlin & Deresiewicz [1953], as well as its simpler variants, e.g. Walton & Braun [1986] and Vu-Quoc &

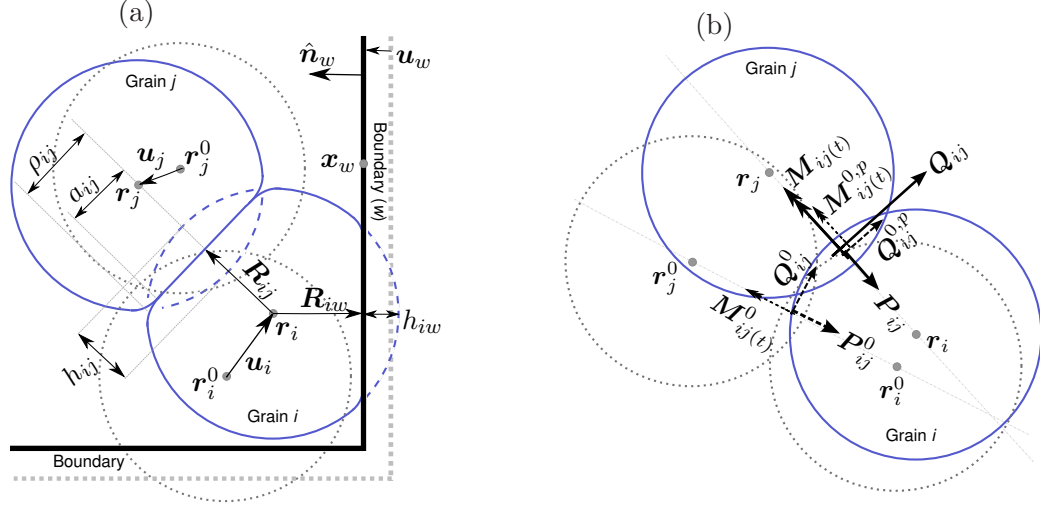


Figure 3.1: (a) Schematic description of contact geometry. The reference configuration of the grains and boundary walls is marked with grey dotted lines. The dashed lines show the shapes of the undeformed grains in the current configuration. (b) The loads on grain i due to its contact with grain j , at the reference and current configuration, marked by dashed and solid arrows, respectively. The reference loads are projected onto the current contact area to account for its rotation.

Zhang [1999a], this dependency is modeled by varying the shear stiffness with the current load and the load history. Thus, estimation of the shear force requires knowledge of the deformation path, including the normal force increment. Here, we simplify computations by linearizing the incremental force-displacement relation. This linearization is justified by the assumption of small grain displacements [Norris & Johnson, 1997]. Within linear approximation, we neglect the effect of the normal force increment on \mathbf{Q}_{ij} relative to that of the reference value, \mathbf{P}_{ij}^0 , decoupling the tangential and normal force increments.

We model friction by Coulomb law, assuming that the tangential force cannot exceed $\mu_{ij}\|\mathbf{P}_{ij}\|$ [Walton & Braun, 1986]. As the shear force approaches this threshold, larger portions of the contact interfaces slip, until sliding occurs. While sliding, the force magnitude is determined by Coulomb's law, $\|\mathbf{Q}_{ij}\| = \mu_{ij}\|\mathbf{P}_{ij}\|$, independently of the stiffness. To model this hysteretic behavior, we evaluate the stiffness by

$$k_{ij(s)} = \begin{cases} \tilde{k}_{ij(s)} & \|\tilde{\mathbf{Q}}_{ij}\| \leq \mu_{ij}\|\mathbf{P}_{ij}\| \\ k'_{ij(s)} & \|\tilde{\mathbf{Q}}_{ij}\| > \mu_{ij}\|\mathbf{P}_{ij}\| \end{cases} \quad (3.4)$$

where $\tilde{\mathbf{Q}}_{ij} = \mathbf{Q}_{ij}^{0,p} - \tilde{k}_{ij(s)} \mathbf{u}_{ij(s)}$, cf. Eq. (3.1), and

$$\tilde{k}_{ij(s)} = 8a_{ij} \left(\frac{2 - \nu_i}{G_i} + \frac{2 - \nu_j}{G_j} \right)^{-1} \quad (3.5a)$$

$$k'_{ij(s)} = \frac{1}{\|\mathbf{u}_{ij(s)}\|^2} \left\{ \mathbf{Q}_{ij}^{0,p} \cdot \mathbf{u}_{ij(s)} + \left[\left(\mathbf{Q}_{ij}^{0,p} \cdot \mathbf{u}_{ij(s)} \right)^2 + \left(\mu_{ij}^2 \|\mathbf{P}_{ij}\|^2 - \|\mathbf{Q}_{ij}^{0,p}\|^2 \right) \|\mathbf{u}_{ij(s)}\|^2 \right]^{1/2} \right\} \quad (3.5b)$$

Here G_i is the shear modulus of the material of grain i . The value of $\tilde{k}_{ij(s)}$ is predicted by Mindlin & Deresiewicz [1953] for the case of negligible slip, expected at the onset of either loading or unloading, see Figure 3.2. Neglecting partial slip, we assume that each load increment results in either complete slip or complete stick. Sliding is modeled by reducing the stiffness value as the force approaches the sliding threshold. The reduced value, $k'_{ij(s)}$, makes the shear force equal to the threshold, and vanishes if the sliding threshold has been reached. The physical meaning of the stiffness coefficient implies that it must be non-negative. Thus, we put $k'_{ij(s)} = 0$ if the term inside the square brackets in Eq. (3.5b) becomes negative.

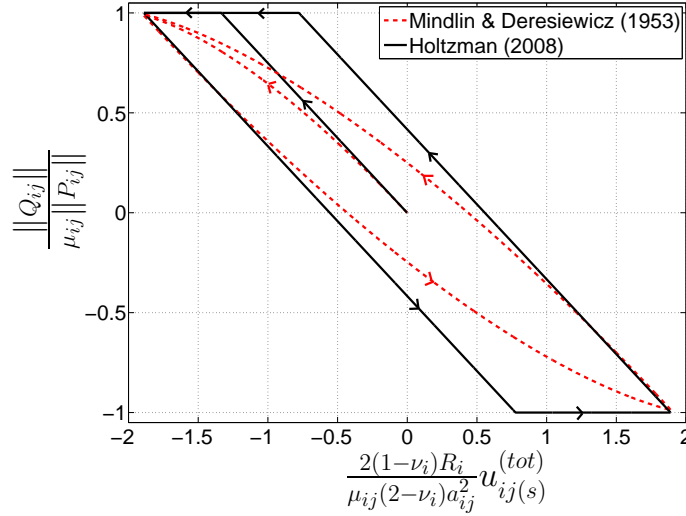


Figure 3.2: The intergranular shear force, $\|\mathbf{Q}_{ij}\|$, vs. the relative shear displacement since contact is established, $u_{ij(s)}^{(tot)}$. The shear force is computed using our model, Eqs. (3.4)–(3.5), and the model in Mindlin & Deresiewicz [1953], for a loading-unloading-reloading cycle (see arrows), assuming a fixed normal force. The plot shows the magnitudes of the respective vectorial quantities normalized to a non-dimensional form, neglecting the change in the force direction. The shear stiffness, $k_{ij(s)}$, corresponds to the slope of the lines.

Within linear approximation, we use the unperturbed force, \mathbf{P}_{ij}^0 , rather than \mathbf{P}_{ij} ,

in Eqs. (3.4)–(3.5). Similarly, we use the corresponding unperturbed values of the radius of disk of intersection, ρ_{ij}^0 , and contact radius, a_{ij}^0 . To justify the latter we expand the expression in Eq. (2.1) as a Taylor's series, noting that the linear term in the expansion can be omitted since $|h_{ij} - h_{ij}^0|/h_{ij}^0 \ll 1$ is implied by the smallness of the perturbation.

3.3.3 Intergranular torsional couples

Relative torsion between a pair of grains creates a torsional couple at their contact interface [Lubkin, 1951; Deresiewicz, 1954]. In this section we propose a torque-rotation relation based on the model of Deresiewicz [1954]. We formulate an incremental-wise path-independent law, using an approach similar to that in Section 3.3.2. We note that in cohesionless materials, the contribution of the intergranular torsion to the averaged macroscopic stress is negligible, see Section 3.5. However, in a cemented grain pack, torsion may determine the strength of each contact [Hills, 1986]. To enable modeling of cement and its failure, we account for torsion in our model.

Consider a pair of grains, i and j , loaded at a reference configuration by a torsional couple, $\mathbf{M}_{ij(t)}^0$, and a normal force, \mathbf{P}_{ij}^0 . Following a perturbation, relative torsion between the grains, $\boldsymbol{\Omega}_{ij(t)}$, increments the torque by

$$\mathbf{M}_{ij(t)} = \mathbf{M}_{ij(t)}^{0,p} - k_{ij(t)} \boldsymbol{\Omega}_{ij(t)} \quad (3.6)$$

where the stiffness $k_{ij(t)}$ describes the contact's resistance to torsion. The effect of reorientation of the contact interface is modeled by rotating the reference torque, $\mathbf{M}_{ij(t)}^{0,p} = \left\| \mathbf{M}_{ij(t)}^0 \right\| \text{sgn} \left(\mathbf{M}_{ij(t)}^0 \cdot \hat{\mathbf{r}}_{ij} \right) \hat{\mathbf{r}}_{ij}$, see Figure 3.1(b). Here sgn denotes the sign function. For a contact with a boundary w , $\mathbf{M}_{iw(t)}^{0,p} = \left\| \mathbf{M}_{iw(t)}^0 \right\| \text{sgn} \left(\mathbf{M}_{iw(t)}^0 \cdot \hat{\mathbf{n}}_w \right) \hat{\mathbf{n}}_w$. The torsion of grain i relative to j , $\boldsymbol{\Omega}_{ij(t)}$, is

$$\boldsymbol{\Omega}_{ij(t)} = [(\boldsymbol{\Omega}_i - \boldsymbol{\Omega}_j) \cdot \hat{\mathbf{r}}_{ij}] \hat{\mathbf{r}}_{ij} \quad \text{for grain-grain contact} \quad (3.7a)$$

$$\boldsymbol{\Omega}_{iw(t)} = (\boldsymbol{\Omega}_i \cdot \hat{\mathbf{n}}_w) \hat{\mathbf{n}}_w \quad \text{for grain-boundary contact} \quad (3.7b)$$

Slip at the contact interfaces may occur in a circumferential direction, making the torque-rotation relation path-dependent [Deresiewicz, 1954]. For simplicity, we linearize the torque-rotation relation to decouple the torque from the normal force increment. To limit the torque by the expected value in sliding [Lubkin, 1951], $M_{ij(t)}^{max} = (3\pi/16) a_{ij} \mu_{ij} \|\mathbf{P}_{ij}\|$,

we compute the stiffness by

$$k_{ij(t)} = \begin{cases} \tilde{k}_{ij(t)} & \|\tilde{\mathbf{M}}_{ij(t)}\| \leq M_{ij(t)}^{max} \\ k'_{ij(t)} & \|\tilde{\mathbf{M}}_{ij(t)}\| > M_{ij(t)}^{max} \end{cases} \quad (3.8)$$

where $\tilde{\mathbf{M}}_{ij(t)} = \mathbf{M}_{ij(t)}^{0,p} - \tilde{k}_{ij(t)} \boldsymbol{\Omega}_{ij(t)}$, cf. Eq. (3.6), and

$$\tilde{k}_{ij(t)} = \frac{16}{3} a_{ij}^3 \left(\frac{1}{G_i} + \frac{1}{G_j} \right)^{-1} \quad (3.9a)$$

$$k'_{ij(t)} = \frac{1}{\|\boldsymbol{\Omega}_{ij(t)}\|^2} \left\{ \mathbf{M}_{ij(t)}^{0,p} \cdot \boldsymbol{\Omega}_{ij(t)} + \left[\left(\mathbf{M}_{ij(t)}^{0,p} \cdot \boldsymbol{\Omega}_{ij(t)} \right)^2 + \left(\left(M_{ij(t)}^{max} \right)^2 - \|\mathbf{M}_{ij(t)}^{0,p}\|^2 \right) \|\boldsymbol{\Omega}_{ij(t)}\|^2 \right]^{1/2} \right\} \quad (3.9b)$$

Here, $\tilde{k}_{ij(t)}$ is the stiffness associated with negligible slip, i.e. at the onset of torsional loading or unloading [Deresiewicz, 1954]. To enforce the torsional threshold the stiffness is reduced to $k'_{ij(t)}$, which vanishes at sliding, see Figure 3.2. Similar to Eq. (3.5b), we put $k'_{ij(t)} = 0$ if the term inside the square brackets in Eq. (3.9b) becomes negative. Finally, within linear approximation, we determine $M_{ij(t)}^{max}$ and $k_{ij(t)}$ by using the unperturbed values \mathbf{P}_{ij}^0 and a_{ij}^0 in Eq. (3.8)–(3.9).

3.3.4 Intergranular moments

Assuming small grain deformations, the normal force component does not produce an appreciable moment relative to the center of the grain. At the same time, the tangential force, \mathbf{Q}_{ij} , is associated with a moment relative to the center of grain i ,

$$\mathbf{M}_{ij(s)} = \mathbf{R}_{ij} \times \mathbf{Q}_{ij} \quad (3.10)$$

The total moment relative to the center of grain i is

$$\mathbf{M}_{ij} = \mathbf{M}_{ij(s)} + \mathbf{M}_{ij(t)} \quad (3.11)$$

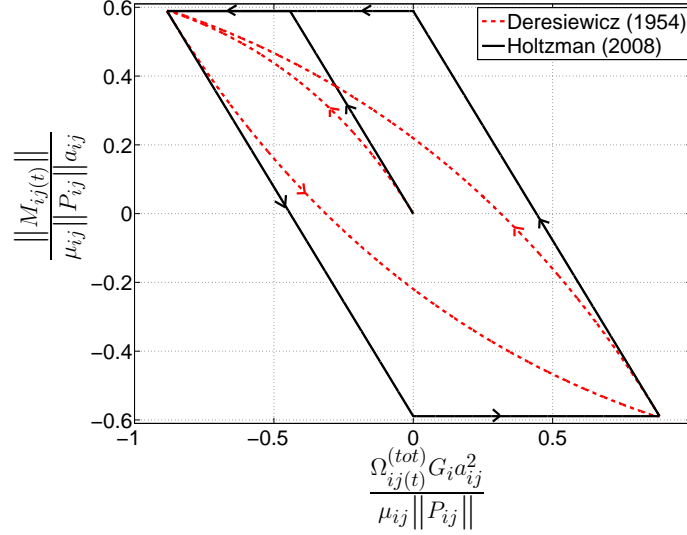


Figure 3.3: The intergranular torsional couple, $\|M_{ij(t)}\|$, *vs.* the relative torsion since contact is established, $\Omega_{ij(t)}^{(tot)}$. The torque is computed using our model, Eq. (3.8)–(3.9), and the model in Deresiewicz [1954], for a loading-unloading-reloading cycle (see arrows), assuming a fixed normal force. The plot shows the magnitudes of the respective vectorial quantities, normalized to a non-dimensional form. The torsional stiffness, $k_{ij(t)}$, corresponds to the slope of the lines.

3.4 Equilibrium configurations

An equilibrium configuration is characterized by a set of generalized coordinates, $\boldsymbol{\theta}$, which satisfy the force and moment balance for each grain,

$$\mathbf{F}_i = \sum_{j=1}^{N_g^i} (\mathbf{P}_{ij} + \mathbf{Q}_{ij}) + \sum_{w=1}^{N_b^i} (\mathbf{P}_{iw} + \mathbf{Q}_{iw}) - m_i g \hat{\mathbf{e}}_z = \mathbf{0} \quad (3.12a)$$

$$\mathbf{M}_i = \sum_{j=1}^{N_g^i} (\mathbf{M}_{ij(s)} + \mathbf{M}_{ij(t)}) + \sum_{w=1}^{N_b^i} (\mathbf{M}_{iw(s)} + \mathbf{M}_{iw(t)}) = \mathbf{0} \quad (3.12b)$$

where \mathbf{M}_i is the sum of moments acting on grain i . Within QuSGM, a variational approach is employed to find these configurations by minimizing an energy functional, Π , with respect to $\boldsymbol{\theta}$. According to the principle of least work [Timoshenko & Goodier, 1970], Π is computed from the work done against the loads on the grains following a perturbation,

$$\Pi(\boldsymbol{\theta}) = - \sum_{i=1}^N \left\{ \frac{1}{2} \sum_{j=1}^{N_g^i} W_{ij} + \sum_{w=1}^{N_b^i} W_{iw} - m_i g (\mathbf{u}_i \cdot \hat{\mathbf{e}}_z) \right\} \quad (3.13)$$

where W_{ij} is the work against the loads acting on grain i due to its contact with grain j ,

$$W_{ij} = W_{ij(n)} + W_{ij(s)} + W_{ij(t)} \quad (3.14)$$

Here, $W_{ij(n)}$, $W_{ij(s)}$, and $W_{ij(t)}$ are the works performed against normal and tangential contact forces, and torsional couples, respectively. We evaluate $W_{ij(n)}$ by computing the elastic strain energy according to Hertz theory, related to normal compression, cf. Eq. (2.6),

$$W_{ij(n)} = - (8/15) E_{ij} (R_{ij})^{1/2} \left[(h_{ij})^{5/2} - (h_{ij}^0)^{5/2} \right] \quad (3.15)$$

The works against the shear and torsional loads are evaluated by integrating the product of these loads and the corresponding displacements, over the displacements following the perturbation. We do not account for heat or vibrations associated with sliding; instead, we assume they are instantaneously dissipated through the boundaries. Assuming that, following a perturbation, the contact loads change monotonically, the work terms are evaluated by numerical integration using a midpoint rectangular rule,

$$W_{ij(s)} = \mathbf{Q}_{ij}^{0,p} \cdot \mathbf{u}_{ij(s)} - \frac{1}{2} k_{ij(s)} \|\mathbf{u}_{ij(s)}\|^2 \quad (3.16a)$$

$$W_{ij(t)} = \mathbf{M}_{ij(t)}^{0,p} \cdot \mathbf{\Omega}_{ij(t)} - \frac{1}{2} k_{ij(t)} \|\mathbf{\Omega}_{ij(t)}\|^2 \quad (3.16b)$$

In sliding, the stiffness vanishes and Eq. (3.16) evaluates the inelastic work of a fixed force and torque with respect to the displacements.

We obtain a local minimum of Π numerically, see Section 2.5. Here, the zero gradient of Π with respect to $\boldsymbol{\theta}$, $\nabla_{\boldsymbol{\theta}} \Pi = -[\mathbf{F}_1 \dots \mathbf{F}_N \quad \mathbf{M}_1/R_1 \dots \mathbf{M}_N/R_N]^T$, provides the balance of forces and moments.

3.5 Macroscopic stress and strain

The macroscopic parameters, namely stress, strain, and elastic moduli are evaluated according to the procedures described in Section 2.6. In particular, the stress is evaluated from the intergranular loads acting on the boundaries, cf. Eq. (2.11). However, the presence of frictional loads implies that the resultant load on the boundaries may include shear and torsion, corresponding to macroscopic shear stresses. If the pack behaves isotropically, the normal strains applied in the principal directions should yield normal stresses only.

To verify that no appreciable shear stresses develop, we compute the total moment applied by the normal and tangential contact forces on the walls with respect to the pack's center. The averaged shear stress can be evaluated from an equivalent force couple. Since

this force couple is at least 2 orders of magnitude smaller than the resultant normal forces, we neglect the shear stresses.

Next, we show that the contribution of torsional couples to the averaged stress is negligible, see also Goddard [1990]. For each torsional couple acting on the walls, we compute an equivalent torque applied with respect to the pack's center. The smallness of the contact area makes the arm of an equivalent force couple much smaller than the size of a single grain. Thus, unless torsion acts very close to the pack's center, the torque it applies is negligible relative to that of a contact force.

3.6 Simulation results

3.6.1 Material properties used in the simulations

The material properties used in the simulations are provided in Table 2.1. Because of the difficulties in estimating the value of the intergranular friction coefficient, see Section 3.2.2, we use a range of values and conduct sensitivity analysis. For glass beads, values of $\mu=0.1$ – 0.3 were measured [Klaas et al., 2005; Li et al., 2005], and used in simulations [Thornton, 2000; Li et al., 2005; Muthuswamy & Tordesillas, 2006; Peña et al., 2008]. In most simulations, we use $\mu=0.3$ for all intergranular and grain-boundary contacts, where μ denotes a uniform coefficient for all contacts. Additional simulations with $\mu=0.5$ and $\mu=0$ are presented.

3.6.2 Initial pack: introduction of frictional loads

Section 2.7.2 describes a procedure to generate a dense irregular packing, involving only normal grain compression. In loose packings, for instance compacted by vibrations, frictional loads may be negligible [Makse et al., 2000]. Consequently, a frictionless pack can be used as the initial configuration in simulating deformation of a loose sample.

Here, we begin the simulations with a relatively dense packing, and thus introduce tangential forces and moments in the initial pack. We generate this pack by the following procedure: (a) a dense packing is created with the frictionless model, cf. Section 2.7.2; followed by (b) transition to a frictional model, introducing frictional loads.

In phase (b), frictional loads are introduced by uniaxial compression of the pack with account for friction. Uniaxial compression creates sufficiently large frictional loads by

forcing relative lateral and torsional grain displacements. Conversely, we find that isotropic loading results in smaller grain rearrangements. This result is intuitive: in a structured arrangement of identical grains, isotropic compression creates a self-similar deformation, with only normal compression between the grains. While our packing is irregular, the degree of load anisotropy is correlated with the number of rearrangements.

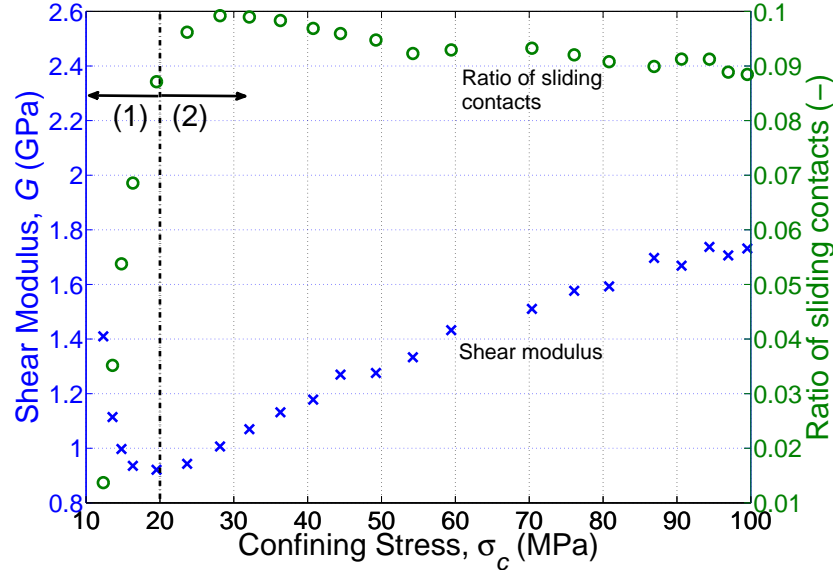


Figure 3.4: The effective shear modulus, G , and ratio of sliding contacts *vs.* confining stress, σ_c , evaluated from sample *G2740* with intergranular friction of $\mu=0.3$, during: (1) sample generation procedure, phase (b); and (2) uniaxial test simulation. The two stages are distinct by a dash-dot line.

During the first part of phase (b), marked by (1) in Figure 3.4, a rapid buildup of frictional loads is observed. This buildup, a consequence of the initially-zero frictional loads, corresponds to a stiffer response than experimentally observed. In particular, the shear modulus, G , predicted at that stage, is overestimated, see Figure 3.4. As the confining stress, σ_c , increases, the initially high G values decrease. This seemingly abnormal behavior results from the generation procedure. Once the frictional loads are well-developed, part (2), the moduli increase with σ_c .

We track progress of the generation procedure through the number of contacts experiencing sliding. The ratio of sliding contacts to total number of contacts is plotted in Figure 3.4. At each contact, sliding is determined by the ratio between the tangential and normal contact forces. At the beginning of phase (b), the tangential forces are zero,

with no sliding. As the generation procedure continues, part (1), the tangential forces increase, initially faster than the normal forces, leading to a rapid increase in the sliding ratio. The shear modulus, G , decreases as sliding increases. When the transition to the frictional contact model is complete, part (2), this artificial growth of the tangential forces stops, and the sliding ratio becomes relatively constant, ~ 0.09 – 0.11 . This “saturation”, also observed in simulations by Thornton [2000] and Peña et al. [2008], marks the end of our generation procedure.

3.6.3 Model verification

3.6.3.1 Accuracy of the numerical algorithm

The path-dependency of the constitutive laws requires following, in incremental steps, the load history [Johnson, 1987; Elata & Berryman, 1996]. Since an analytical solution is unavailable, a comprehensive verification of our numerical algorithm is not possible. Instead, we simulate deformations that produces normal contact forces only, and verify that our algorithm predicts such loads. We use a similar pack to that described in Section 2.7.3.1, deformed in a self-similar manner. Consequently, the relative displacements between contacting grains are in the direction of their centerline, corresponding to compressive strains. To inhibit grain rotations, we assume ideally-smooth boundaries. The analytical solution to this problem is thus identical to the one obtained assuming frictionless grains.

Similarly to the simulations with ideally-smooth grains, symmetry for the bottom grains is preserved. The relative error, measured as the deviation from a self-similar deformation, $(r_{ij}^A - r_{ij}^N) / r_{ij}^A$, is $\sim 10^{-11}$ – 10^{-9} . Here, r_{ij}^A and r_{ij}^N denote the distance between the top grain and a bottom grain, computed analytically and numerically, respectively. This error is slightly higher than in the frictionless model, see Figure 2.8. The error is increased because tangential forces develop due to the deviations from self-similar deformations and small ($\sim 10^{-9}$) grain rotations. While these forces are small compared to the normal components (by a factor of $\sim 10^{-9}$ – 10^{-8}), they increase the geometrical error and cause further departure from self-similar deformation.

3.6.3.2 Verification against experimental data

We verify our model against experimental data, for the general case of irregular packing. We use the published data from acoustic measurements in packs of glass beads, as well as the DEM simulations and EMT calculations, presented in Section 2.7.3.2. The use of artificial grains allows for a better controlled experiment relative to one performed on geologic materials, mainly because of the irregular grain shapes in the latter.

To evaluate the effective moduli of a pack of frictional grains, we simulated two uniaxial strain tests, using two initial packs generated by: (i) isotropic compression of sample *G2740* to $\sigma_c^{\mu=0}=4$ and $\sigma_c^{\mu=0}=10$ MPa in phase (a); followed by (ii) uniaxial compression with the friction coefficient $\mu=0.3$ to $\sigma_c=9$ and $\sigma_c=19$ MPa in phase (b), see Section 3.6.2. To examine the effect of the intergranular friction coefficient (Section 3.6.4.3), the latter simulation ($\sigma_c^{\mu=0}=10$ MPa) was reproduced with $\mu=0.5$. In Figure 3.5 we plot the effective elastic moduli *vs.* confining stress, σ_c , evaluated from these simulations and the published data. Good agreement between our estimates and the experimental data, achieved with no adjustment of material parameters, verifies the physical soundness of our model.

We stress that the effective moduli are not uniquely defined by the grain properties alone; they also depend on the spatial distribution of these properties, and, possibly, on the loading history [Magnanimo et al., 2008]. This indeterminacy is enhanced by sensitivity of the bulk response to small perturbations, leading to emergent properties: small variations in grain configurations can result in significantly different properties [Behringer et al., 1999; Holtzman et al., 2008b]. Inevitable uncertainty in characterizing grain configurations, makes exact reproduction of an experiment by numerical simulations impossible, and leads to large scatter in experimental data, e.g., see Figure 3.5.

3.6.4 Sensitivity analysis

3.6.4.1 Sensitivity to the initial packing

The mechanical properties of a grain pack during testing depend on the initial packing, the loading path, and the final state of stress. The initial pack has a loading history of itself, i.e. prior to the beginning of the test. Thus, characterization of the initial pack should include its microstructure, intergranular loads, and possibly the load history of each contact. Our sample generation procedure involves “activation” of frictional resistance by uniaxial loading, see Section 3.6.2, affecting the initial packing, and thus can

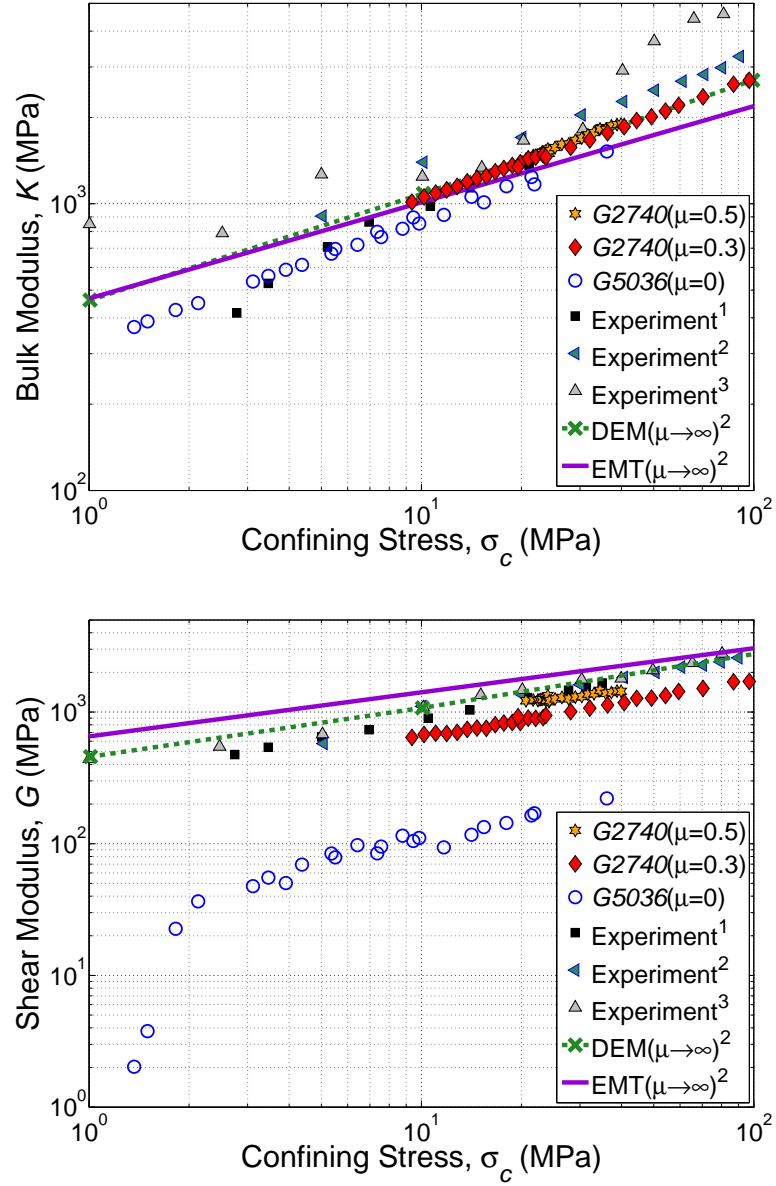


Figure 3.5: The effective bulk (K , top) and shear (G , bottom) modulus *vs.* confining stress, σ_c . The moduli evaluated from simulations are compared with the results of acoustic experiments in glass beads, as well as DEM and EMT computations. Superscripts 1–3 refer to the data published in Domenico [1977], Makse et al. [1999], and Yin [1993], respectively.

be considered as part of the load history.

To examine the effect of the initial packing, we conduct a series of uniaxial test simulations on different initial packs. To generate these packs, sample *G2740* has been

compacted isotropically up to stresses of $\sigma_c^{\mu=0} = 4, 10, 20, 41, 54$ and 74 MPa in phase (a) of the generation procedure, followed by application of uniaxial strain with a friction coefficient of $\mu=0.3$ in phase (b). The resulting initial packs are denoted by $G2740(4)$, $G2740(10)$, $G2740(20)$, $G2740(41)$, $G2740(54)$, and $G2740(74)$. While these packs contain similar grains, their microstructure, and consequently their mechanical properties, may differ due to different loading paths [Magnanimo et al., 2008].

In Figure 3.6, the effective moduli of these packs are plotted *vs.* confining stress, σ_c , evaluated during: (1) phase (b) of the generation procedure; and (2) uniaxial test simulation. Results for samples $G2740(10)$ and $G2740(41)$ are highlighted in the plot. Comparing the moduli evaluated at similar confining stresses, we observe that the bulk modulus is lower for samples with higher $\sigma_c^{\mu=0}$ values. While the bulk modulus predicted from simulations on $G2740(4)$ and $G2740(10)$ is relatively similar ($\sim 1\%$ variation), the difference with other initial samples, e.g. $G2740(41)$, increases to $\sim 10\%$. The shear modulus exhibits smaller sensitivity, with relatively small variations among the different simulations.

To investigate these seemingly counterintuitive observations, we calculate the mean normal contact force within the pack, \bar{P} . At a given confining stress, \bar{P} is higher in packs with lower $\sigma_c^{\mu=0}$. This difference reflects the different load paths during the generation procedure. Lower $\sigma_c^{\mu=0}$ means that uniaxial strain loading started at a lower stress, indicating that the sample has experienced larger axial stress and lower lateral stress. The stronger loading anisotropy implies more grain rearrangements, see Section 3.6.2, which increase the packing density and consequently the normal forces (\bar{P}). Thus, since the bulk modulus is mainly affected by the normal contact forces, it increases with \bar{P} , while the shear modulus shows lesser sensitivity.

3.6.4.2 Sensitivity to the size of load increments

In our simulations, loading is applied in increments. Each load increment corresponds to a perturbation of the boundary conditions, sufficiently small so that the size of the relative grain displacements justify linearization of the constitutive relations, see Section 3.3. The tradeoff between the size of the load increments and the number of increments imposes a constraint on the increment's size. In this section, we test our model robustness with respect to the size of the load increments.

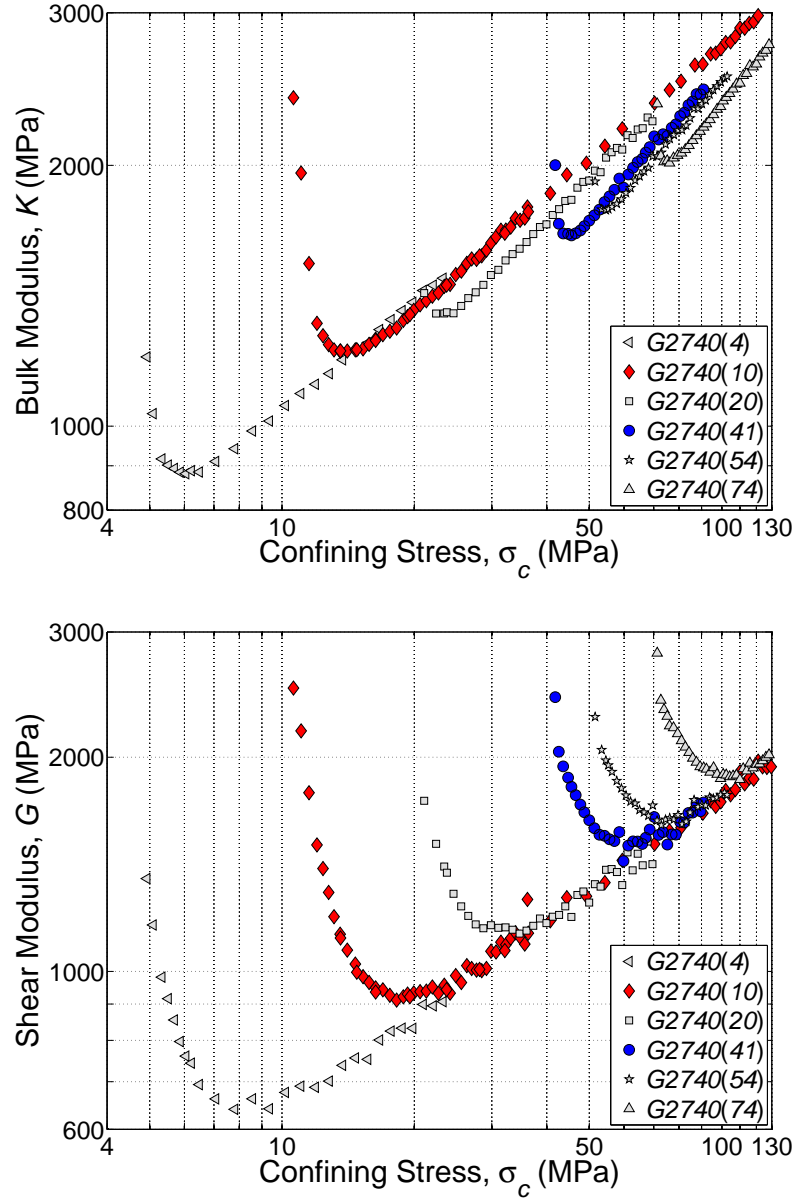


Figure 3.6: The effective bulk (K , top) and shear (G , bottom) modulus *vs.* confining stress, σ_c , evaluated during: (1) sample generation procedure, phase (b); and (2) uniaxial compression test simulations, conducted on sample $G2740$ with intergranular friction of $\mu=0.3$. Six simulations were conducted on initial packs generated with different stresses during phase (a), $\sigma_c^{\mu=0}$. At a given σ_c , K is lower for samples with higher $\sigma_c^{\mu=0}$ values, e.g. it is lower for $G2740(41)$ than for $G2740(10)$, whereas G shows lesser sensitivity.

To examine sensitivity to the increment's size, we compare simulations on sample $G2740$, applying different strain increments. In Figure 3.7, we plot the moduli evaluated

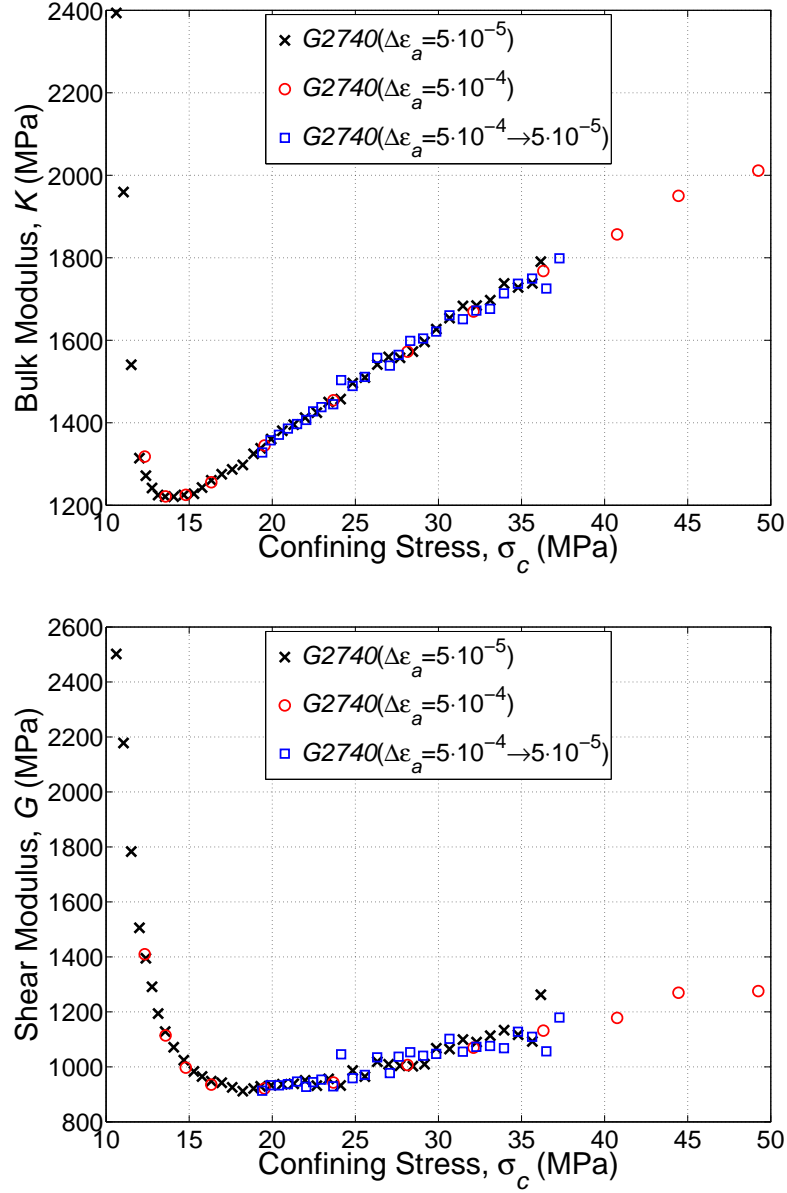


Figure 3.7: The effective bulk (K , top) and shear (G , bottom) modulus *vs.* confining stress, σ_c , evaluated during: (1) sample generation procedure, phase (b); and (2) uniaxial compression test simulations, conducted on sample $G2740$ with intergranular friction of $\mu=0.3$. We plot results from three simulations, with uniaxial strains of $\Delta\epsilon_a=5 \cdot 10^{-4}$, $\Delta\epsilon_a=5 \cdot 10^{-5}$, and their combination. The small differences demonstrate our model's robustness with respect to the size of the load increments.

during: (1) phase (b) of the generation procedure (Section 3.6.2), and (2) uniaxial test simulation, *vs.* confining stress. We present results from two simulations using axial strains of $\Delta\epsilon_a=5 \cdot 10^{-5}$ and $\Delta\epsilon_a=5 \cdot 10^{-4}$, in addition to a simulation in which the strain

was reduced from $\Delta\epsilon_a=5 \cdot 10^{-4}$ during the generation procedure to $\Delta\epsilon_a=5 \cdot 10^{-5}$ at the uniaxial test. The small differences imply that our model is robust with respect to $\Delta\epsilon_a$.

3.6.4.3 Effect of the intergranular friction coefficient

The effects of intergranular friction on the bulk response, the microstructure, and the way forces are transmitted within a sample, were studied in Behringer et al. [1999], Thornton [2000], Goldenberg & Goldenhirsch [2005], Anthony & Marone [2005], Cui & O'Sullivan [2006], Pohlman et al. [2006], Muthuswamy & Tordesillas [2006] and Peña et al. [2008]. For example, experiments and simulations show that the angle of repose is correlated with the intergranular friction coefficient [Cui & O'Sullivan, 2006; Pohlman et al., 2006; Peña et al., 2008]. Note that frictional resistance at each contact is not uniquely determined by the friction coefficient. In our model, this resistance is computed by: (1) the friction coefficient, μ , and the normal force magnitude, $\|\mathbf{P}_{ij}\|$, if sliding occurs; (2) the tangential and torsional stiffness, $k_{ij(s)}$ and $k_{ij(t)}$, if the contact does not slide. The sliding threshold, and, on the verge of sliding, the stiffness values, $k'_{ij(s)}$ and $k'_{ij(t)}$, depend on μ and $\|\mathbf{P}_{ij}\|$.

To investigate the sensitivity of the effective moduli to the friction coefficient, μ , we compare the moduli predicted from two simulations, with $\mu=0.3$ and $\mu=0.5$, and $\sigma_c^{\mu=0}=10$ MPa, see Section 3.6.3. The moduli are plotted in Figure 3.8 *vs.* confining stress. As expected, the moduli increase with the friction coefficient. In particular, the shear modulus strongly depends on the intergranular friction.

To complete this analysis, we study the effect of extreme μ values. Our simulations show that a frictionless model ($\mu=0$) underestimates the stiffness and strength of the pack, in particular under shear. For example, it predicts loss of shear rigidity, $G \rightarrow 0$, at relatively high packing densities, see Section 2.7.3.2. Similar observations were made by Makse et al. [2004]. Conversely, Makse et al. [2004] demonstrated that a model which prohibits sliding ($\mu \rightarrow \infty$) overestimates G . Note that macroscopic stiffness and strength do not increase significantly when the friction coefficient increases above a certain value (e.g., $\mu=0.6$ in Muthuswamy & Tordesillas [2006]). Similar saturation of other macroscopic parameters with respect to μ was observed in simulations [Thornton, 2000] and experiments [Blair et al., 2001]. This trend may signal that mechanisms other than grain sliding become dominant [Muthuswamy & Tordesillas, 2006].

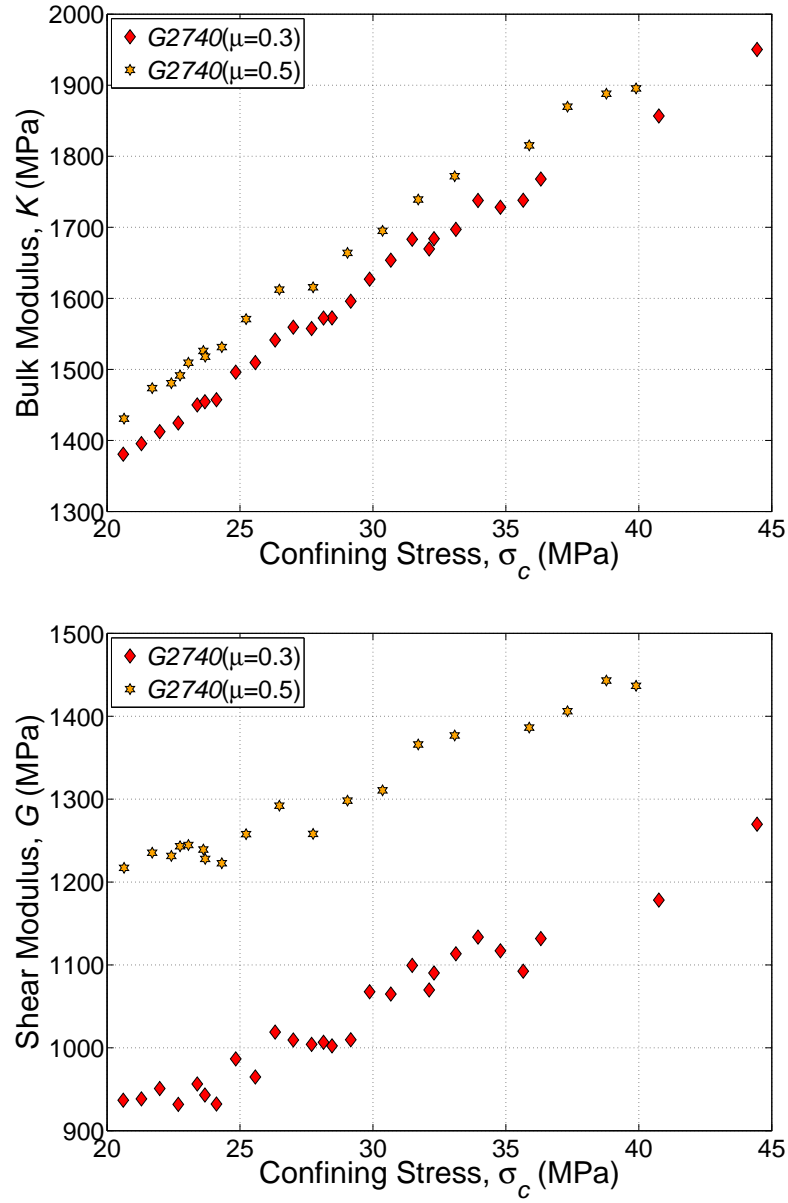


Figure 3.8: The effective bulk (K , top) and shear (G , bottom) modulus *vs.* confining stress, σ_c , evaluated from two simulations on sample $G2740$, with different intergranular friction coefficients, $\mu=0.3$ and $\mu=0.5$. The effective moduli, in particular G , increase with the friction coefficient.

3.7 Concluding remarks

To evaluate the mechanical properties of a cohesionless granular material, we have presented a micromechanical model within the framework of QuSGM. The intergranular interactions, including friction and sliding, are modeled by a set of constitutive relations based on the contact theories of Hertz, Mindlin, and Deresiewicz. The equilibrium grain configurations are computed by minimizing an energy functional. Employing the principle of least work, this functional is evaluated from the work against the intergranular loads.

We have verified our model's predictive capabilities against published experimental data. The grain-scale parameters used in the simulations are taken from published experiments. Good agreement between predicted and measured values of the effective moduli is achieved with no adjustments of material parameters, confirming the physical soundness of our model. The robustness of our model with respect to the size of the load increment has also been demonstrated.

Sensitivity analysis confirms that the stiffness of a grain pack increases with the intergranular friction coefficient. The shear modulus is more sensitive to the intergranular friction than the bulk modulus, which mainly depends on the normal contact forces. We conclude that proper account of intergranular frictional resistance is required to predict the response of a grain pack, in particular under shear. Modeling intergranular friction faces several problems. It is difficult to evaluate the friction coefficient, which can vary with the deformation. Moreover, the validity of a Coulomb-type friction law at the grain-scale needs further investigation [Behringer et al., 1999].

Examining the effect of the initial packing, we show that different loading paths within the generation procedure result in different packs with variable properties. Thus, the grain properties do not uniquely define a grain pack: the loading history, as well as spatial distribution of the grain properties, strongly affect the macroscopic properties. Indeterminacy is enhanced by the sensitivity of the macroscopic properties to small perturbations, and rare events in the form of large displacements of individual grains. Combining our simple yet physically-based computational technique with experimental evidence, allows to relate the grain- and macro-scale, and predict the behavior of granular materials.

Chapter 4

Nonlinear deformation of weakly-cemented sediments: a paradigm?

4.1 Introduction

WE STUDY the mechanics of weakly-cemented granular materials in which the grains are bonded together by small amounts of cement, through grain-scale simulations. Cementation of grain contacts is related to the deposition of minerals which infiltrate the pore space in aqueous solution [Bernabè et al., 1992; Jin et al., 2003; Jin, 2006] or are dissolved by pressure dissolution of rock material [Tada & Siever, 1989; Dewers & Ortoleva, 1990; Renard et al., 2000; Gratier et al., 2005]. Poorly-consolidated sedimentary rocks in oil and water reservoirs may cause problems such as subsidence, well-bore instability, and sanding, see Saidi et al. [2003] and the references within.

Earlier, we concluded that the complex, inelastic behavior of particulate materials is attributed to: (a) variations of the intergranular contact area with the deformation; (b) path-dependent intergranular force-displacement relation due to frictional slip; and (c) variations in the contact network. In cemented materials, cement constraints relative motions of the grains, unless the intergranular loads exceed the cement's strength. Thus, introduction of cement is expected to regularize the deformation process, reducing the nonlinearity of the bulk response [Dvorkin et al., 1991]. This hypothesis underlies many of the models found in the literature, e.g. Dvorkin et al. [1991], Dvorkin et al. [1994], Jin et al. [2003] and Potyondy & Cundall [2004]. However, experimental observations are in odds with the above hypothesis, showing significant variations in the mechanical properties of

weakly-cemented sediments with deformation. Determination of micromechanical origins for the nonlinear sediment deformation is the main objective of this chapter.

To investigate the micromechanics of cemented materials, i.e. relate the overall response of a sample to the grain and cement properties, we simulate deformation of a cemented pack within the framework of QuSGM. We introduce the effect of cement at the contacts through a set of constitutive relations. To account for inelastic deformations of the cemented contacts, we relate the contact stiffness to the deformation it experiences. We present several models that represent different types of microscopic deformation mechanisms. Our simulations reveal that matching experimental data requires account of nonlinear contact deformations, e.g. through the constitutive rules. Conversely, models based on the concept of linear-elastic cement deformation, fail to reproduce the data.

This chapter is organized as follows. In Section 4.2, we overview published experimental evidences of nonlinear deformation of cemented samples, and discuss possible mechanisms. A conceptual model of a cemented grain pack is presented in Section 4.3, and implemented through a set of constitutive rules in Section 4.4. The construction of a numerical pack is discussed in Section 4.5. In Section 4.6, we provide a methodology by which the equilibrium configurations are obtained. In Section 4.7, an alternative approach is proposed, using a “parallel bond” model. Unlike the models described above, in which *effective* parameters represent the properties of *both* the grains and the cement, in the parallel bond model the grain-grain and grain-cement interactions are treated *separately*, using two sets of constitutive rules. Section 4.8 provides the simulations results. In Section 4.8.1, we demonstrate the ability of an exponential constitutive relation to reproduce experimental data. The performance of the numerical algorithm is discussed in Section 4.8.2. In Section 4.8.3, we compare the results obtained by using the different constitutive rules we proposed. The physical meaning of our model parameters and their effect on the bulk response are discussed in Section 4.8.4. Section 4.9 concludes this chapter.

4.2 Inelastic response of weakly-cemented materials

4.2.1 Experimental macroscopic observations

The mechanical properties of weakly-cemented materials cannot be described by a linear-elastic model with constant elastic moduli. In uniaxial compression of synthetic and

naturally cemented sediment samples, the stress-strain curve is nonlinear [Jaeger & Cook, 1979; Martin & Chandler, 1994; David et al., 1998; Nakagawa & Myer, 2001; Holt, 2001; Saidi et al., 2003], see Figure 4.1. Another expression of nonlinear behavior is variations of the elastic moduli with the deformation [Murphy, 1982; Martin & Chandler, 1994; Saidi et al., 2003; Nakagawa, 2008]. Nakagawa [2008] measured wave velocities during a uniaxial loading-unloading cycle in cemented samples, see Figure 4.2. Five packs of quartz grains with an initial porosity of $\sim 35\%$ were cemented by different quantities of soda-lime glass¹. A sample of Berea sandstone was also tested. An increase of the velocities with stress, corresponding to an increase in the elastic moduli, cf. Eq. (2.20), is especially noticeable in the weakly-cemented, more porous packs, particularly at low stresses. Inelastic response is evident even under relatively low stresses. For example, the unloading-reloading cycles in Figure 4.1 do not coincide with the main stress-strain curves, implying inelastic deformation [Jaeger & Cook, 1979], whereas acoustic emissions detected immediately after loading are correlated with formation of microcracks [Holt, 2001].

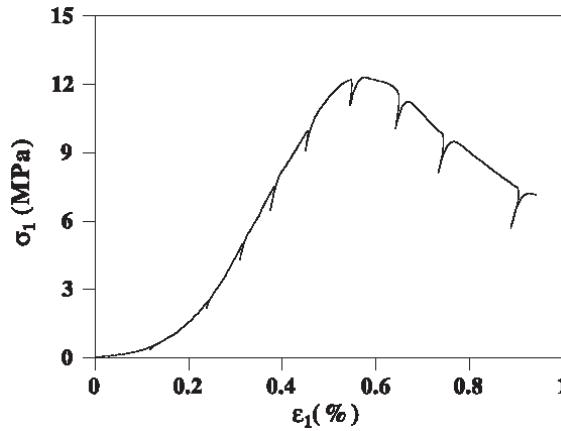


Figure 4.1: A typical stress-strain curve from uniaxial compression of quartz grains bonded by Portland cement. The initially convex curve, corresponding to strain hardening, becomes approximately linear with further compression. Additional loading results in softening (concavity), and finally failure (peak) followed by post-failure behavior (negative slope). Small unloading-reloading cycles were performed to estimate Young's modulus, see Figure 4.7. Adapted from Saidi et al. [2003].

The conventional explanation for the deviation from linear-elastic response is through closure and formation of microcracks in the cemented contacts [Jaeger & Cook, 1979; Martin & Chandler, 1994]. Martin & Chandler [1994] divide a typical stress-strain

¹Compaction was applied to obtain the densest pack (7.3%) in Figure 4.2.

curve, e.g. Figure 4.1, into several regions, which correspond to different stages of deformation: (a) as loading begins, the first region is marked by convexity of the curve, related to closure of pre-existing microcracks; (b) once these cracks close, the material is considered elastic, with a relatively linear response; (c) slight concavity is associated with formation of new cracks which reduce the overall stiffness of the material. These cracks are “stable”, in the sense that further cracking requires to increase the load. This behavior is accompanied by dilatation; (d) as the stress increases above a certain level, the total volumetric strain reverses, marking the onset of unstable crack growth, and sliding along surfaces created by coalescent cracks; (e) the stress-strain peaks, after which the stress begins to decrease with additional strain. The stress at the peak is commonly referred to as the “failure strength”.

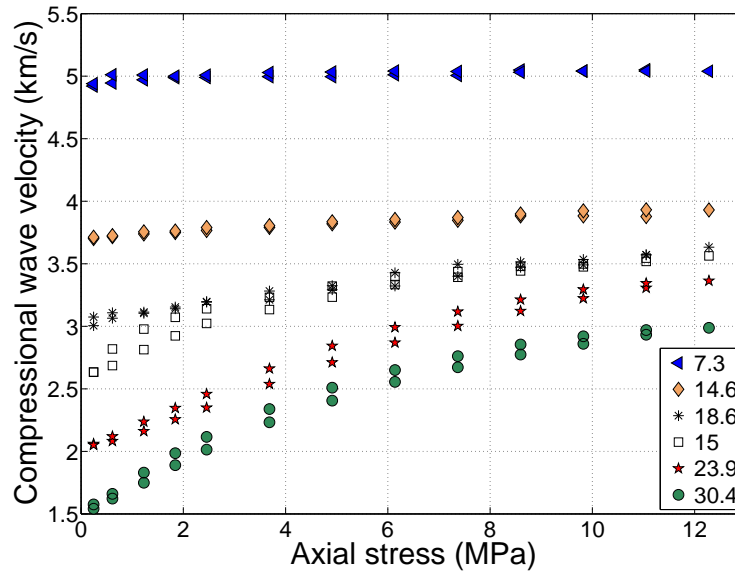


Figure 4.2: Compressional acoustic wave velocities *vs.* axial stress. Velocities were measured by Nakagawa [2008] in five synthetic packs with different porosities, denoted by the legend entries (in %), and a sample of Berea sandstone (15%), during uniaxial loading-unloading cycle. The lower velocities correspond to loading. In the weakly-cemented packs, velocities increase significantly with stress, particularly at lower stresses.

4.2.2 Possible mechanisms for nonlinear contact deformation

In this work, we focus on the initial stages of loading, (a)–(b), namely strain-hardening followed by the so-called elastic regime. A fundamental question immediately arises regarding the sources of the observed nonlinearities. In particular, are the main

mechanisms similar to nonlinear deformation of the *grains* and variations in the *contact network* in uncemented materials, or, are they attributed to nonlinear deformation of the *cement* itself? To answer this question, we examine several possible mechanisms for nonlinear contact deformation: (1) formation, closure, and reopening of microcracks; (2) changes in the geometry of the cemented contact interfaces; and (3) propagation of deformation into heterogeneous cement and grain materials.

Microcracks exist in most cemented particulate materials, at different scales, from interatomic dislocations to fractures [Kranz, 1983]. Acoustic emissions soon after loading begins are experimental evidence of early development of microcracks [Holt, 2001]. Microcracks are evident in the scanning electron microscopy (SEM) images in Figure 4.3.

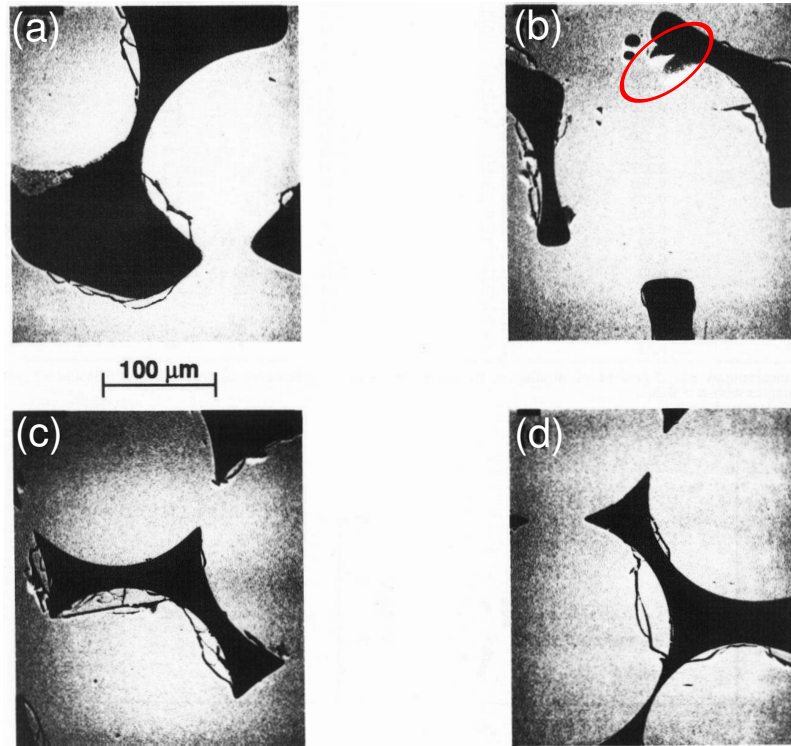


Figure 4.3: SEM images of four synthetic sandstones with porosities of (a) 0.17, (b) 0.29, (c) 0.37, and (d) 0.39. A pack of glass beads (in white, pore space in black) was sintered by heat. Microcracks are evident, both within the grains, far from the contact area, as well as in the cement material bridging the grains (encircled). Adapted from Berge et al. [1995].

Geometrical nonlinearities are related to variations in the cemented contact area and plastic deformation of asperities. The contact interfaces can be quite irregular, especially in the presence of cement which is itself granular, see Figure 4.4. Thus, the contact

mechanics cannot be described by theories assuming smooth surfaces, e.g. Hertzian. Consider, for example, compression of two cemented grains with an irregular contact surface. The initially small contact area corresponds to a smaller resistance to compression. Concentration of the stress over the small area will result in inelastic deformation of asperities made of granular cement. This deformation, in turn, will significantly increase the contact area, and thus the contact stiffness. For grains bonded by a soft cement layer, we propose the following intuitive explanation: in extension, the layer becomes thinner, and thus more susceptible to further deformation; conversely, compression makes the cement denser, and thus less compliant. Similarly, shear of asperities and micro-slip is expected to yield inelastic shear and torsional deformations.

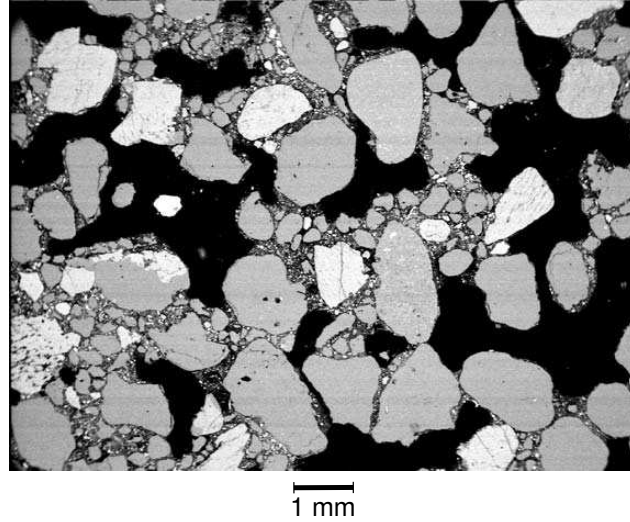


Figure 4.4: SEM images of sand grains bonded by Portland cement. The pores appear in black. The sand grains are the larger particles (mean diameter of ~ 0.8 mm), and the granular cement consists of the smaller particles (few microns), both in grey. The volumetric fraction of the cement is $\sim 9\%$. Adapted from Saidi et al. [2005].

Finally, material heterogeneity can result in nonlinear contact deformation. We consider a contact region to be heterogenous if: (a) softer cement coats a large portion of the contact interface, forming a soft layer between the stiffer grains; and (b) the grains themselves are heterogenous, due to variable mineralogy or as a result of weathering. Let us consider, for example, two bodies which are stiffer from the inside, with a softer exterior. Under the assumption of localized deformations [Johnson, 1987], compression initially results in deformation mainly within the softer material. As compression increases, the deformation propagates into the deeper, stiffer portions of the bodies, corresponding to an

increase in the effective contact stiffness.

In weakly-cemented materials, we hypothesize that mechanisms (1)–(3) may become dominant over those which govern the behavior of uncemented materials. To examine this hypothesis, we model nonlinear contact deformation by correlating the effective stiffness of each contact to the deformation it experiences, and compare the bulk properties with experimental data.

4.3 Conceptual model of a pack of cemented grains

Characterizing the properties of a cemented contact is a difficult task. The geometry of cement deposited around the grain contacts is complex [Jin, 2006; Brouste et al., 2007]. Experimental evaluation of the contact geometry, for instance from SEM images [Berge et al., 1995; David et al., 1998; Holt et al., 2005] or thin sections [Yin, 1993], is cumbersome. Additionally, the cement material can be highly heterogenous, cf. Figure 4.4. Consequently, formulating constitutive relations which account for the geometry and material properties of a cemented contact requires complex numerical analysis, for instance by FEM [Munjiza et al., 1995]. Alternatively, the grain and contact geometry can be approximated by a simpler shape, allowing to obtain an semi-analytical solution [Dvorkin et al., 1991, 1994]. Employing either techniques makes computations in a large grain pack time consuming.

In our model, the detailed account of the contact geometry and material properties is replaced by the following conceptual model: for each pair of cemented grains, the cemented contact region is modeled as a beam, which undergoes deformations due to relative motions of the grains. We formulate simple constitutive rules, which relate the intergranular loads and deformations *via* a set of effective parameters. Thus, these parameters represent the effect of the cement and grain materials, and the contact geometry.

To evaluate the deformations imposed by the relative grain displacements, we consider an idealized sample: an irregular packing of spherical grains. A physical example of such a pack is shown in Figure 4.5. Note that we consider samples with small amounts of cement which *bonds* the grains together, excluding samples with larger amounts of cement which *coats* the grains and significantly increases the contact area. The sample with 4% cement content in Figure 4.5 is an example of the latter.

The models presented in this chapter are based on QuSGM, describing the de-

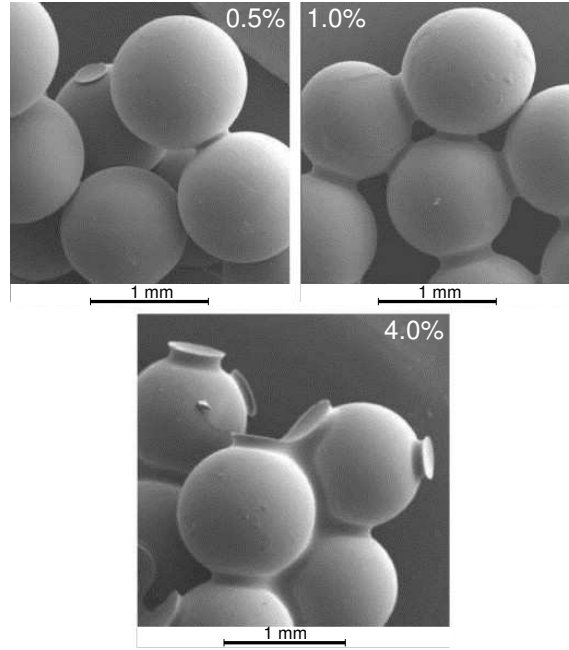


Figure 4.5: SEM images of synthetic sandstones made of epoxy-cemented glass beads, with cement/glass beads weight percentage of 0.5, 1.0, and 4.0%. We model weakly-cemented packs in which cement is localized at the grain contacts (e.g. the 0.5% and 1.0% samples), and exclude those with higher cement content, in which cement is coating the grains (4.0%). Adapted from Holt et al. [2005].

formation by a sequence of equilibrium configurations. Simulations begin with an *initial*, undeformed configuration. The pack is loaded by incremental displacements of its boundaries. Let us consider a pair of cemented grains. At a given *reference* configuration, a perturbation of the boundary conditions alters the intergranular load, F^0 . The *current* load, $F = F^0 + \Delta F$, is found by adding a load increment ΔF , which is computed from an incremental constitutive rule, $\Delta F = k\Delta X$. Evaluation of the effective stiffness parameter k , which includes information on the properties of the grains and the cement, is the subject of the next section.

4.4 Constitutive relations for cemented grains

The constitutive rules presented in the following sections are based on the contact mechanics theories of Hertz [1882], Mindlin & Deresiewicz [1953] and Deresiewicz [1954]. These theories, developed for cohesionless grains, are modified here to accommodate the effect of cement by: (a) assigning effective contact properties; and (b) restricting relative

grain displacements by prohibiting grain sliding. To model nonlinear cement deformation, we propose several rules for the evolution of the effective stiffness with the deformation. Our models do not account for fracturing of grains. Experimental evidence suggests that grain breakage occurs under very high stresses, and the cement material, usually weaker than the grains, breaks first [Bernabè et al., 1992; Yin & Dvorkin, 1994; Holt, 2001]. Furthermore, we do not model complete failure of the cement material, i.e. loss of cohesion at the contact, which can be justified by the assumption that the bulk response is mainly controlled by the behavior of the intact cemented contacts [Holt, 2001].

4.4.1 Normal component of the intergranular forces

In this section, we formulate a force-displacement relation for the normal component, based on Hertzian contact law. We follow the usual assumption that the normal force component is unaffected by shear and torsion, and can be computed independently [Johnson, 1987; Dintwa et al., 2008].

Let us consider a pair of cemented grains, i and j . At a given reference configuration, the deformation of the cement and grain materials imposes a normal force, \mathbf{P}_{ij}^0 , on grain i . The force can be compressive or tensile. A similar force in the opposite direction is applied on grain j . Following a small perturbation, the force becomes

$$\mathbf{P}_{ij} = \mathbf{P}_{ij}^{0,p} - k_{ij(n)}^* \mathbf{u}_{ij(n)} \quad (4.1)$$

where the effective normal stiffness $k_{ij(n)}^*$ denotes the resistance of that contact to compression and tension. To account for the reorientation of the contact interface, the unperturbed force, \mathbf{P}_{ij}^0 , is rotated by $\mathbf{P}_{ij}^{0,p} = \|\mathbf{P}_{ij}^0\| \operatorname{sgn}(\mathbf{P}_{ij}^0 \cdot \hat{\mathbf{r}}_{ij}) \hat{\mathbf{r}}_{ij}$, see Figure 3.1(b). For a contact with a boundary w , $\hat{\mathbf{r}}_{ij}$ is replaced with the outward normal to that boundary, $\hat{\mathbf{n}}_w$. The grain-boundary and grain-grain interactions are treated in a similar manner, i.e. using identical constitutive rules. The normal component of the displacement of grain i relative to grain j , $\mathbf{u}_{ij(n)}$, is computed by

$$\mathbf{u}_{ij(n)} = \hat{\mathbf{r}}_{ij} \otimes \hat{\mathbf{r}}_{ij} (\mathbf{u}_i - \mathbf{u}_j) \quad \text{for grain-grain contact} \quad (4.2a)$$

$$\mathbf{u}_{iw(n)} = \hat{\mathbf{n}}_w \otimes \hat{\mathbf{n}}_w (\mathbf{u}_i - \mathbf{u}_w) \quad \text{for grain-boundary contact} \quad (4.2b)$$

The normal stiffness $k_{ij(n)}^*$ is evaluated through a Taylor's expansion of the Hertzian contact law, cf. Eq. (2.2), with respect to the mutual approach, h_{ij} . Keeping only the linear

term, $\Delta \|\mathbf{P}_{ij}\| \approx \frac{\partial \|\mathbf{P}_{ij}\|}{\partial h_{ij}} \bigg|_{h_{ij}^0} dh_{ij}$, provides an estimate for the force increment in Eq. (4.1), $-k_{ij(n)}^* \mathbf{u}_{ij(n)}$. Assuming that $\Delta \|\mathbf{P}_{ij}\|$ is directed along the normal displacement, $\mathbf{u}_{ij(n)}$, the stiffness is evaluated by replacing the differential dh_{ij} in the above with $\|\mathbf{u}_{ij(n)}\|$,

$$k_{ij(n)}^* = 2E_{ij}a_{ij}^* \quad (4.3)$$

where E_{ij} is an effective elastic parameter used in Hertz theory, cf. Eq. (2.3), and a_{ij}^* is the effective contact radius which includes the effect of cement. In obtaining Eq. (4.3) we use the relation between the contact radius and the mutual approach from Hertzian theory, $a_{ij} = (R_{ij}h_{ij})^{1/2}$, where R_{ij} is defined in Eq. (2.3).

Simulations begin with an initial, undeformed configuration, see Section 4.5. The values measured at the initial configuration are denoted by superscript (c). The initial effective radius, $a_{ij}^{*(c)}$, is evaluated by

$$a_{ij}^{*(c)} = a_{ij}^{(c)} + a_{ij}^{CEM} = (1 + \kappa) a_{ij}^{(c)} \quad (4.4)$$

where $a_{ij}^{(c)} = (R_{ij}h_{ij}^{(c)})^{1/2}$ and $a_{ij}^{CEM} = \kappa a_{ij}^{(c)}$ are the portions of the contact radius associated with the grain-grain and grain-cement contact, respectively. The initial contribution of the cement to the effective area is quantified through κ , representing the increase in the contact radius following cementation. Thus, κ is related to the cement content, as well as its geometry and material properties. We use a uniform value of κ for all contacts. In the limiting case of negligible amount of cement, $\kappa \rightarrow 0$, the effective radius approaches that predicted by Hertz theory, $a_{ij}^* \approx a_{ij}$. In Section 4.4.4 we propose several models that link the evolution of the stiffness $k_{ij(n)}^*$ to the local deformation.

4.4.2 Tangential component of the intergranular forces

Consider a pair of cemented grains, i and j , loaded by a force acting tangentially to the contact plane, \mathbf{Q}_{ij}^0 , see Figure 3.1(b). A perturbation results in small relative tangential displacement of the contact interfaces, $\mathbf{u}_{ij(s)}$, and alters the tangential force, according to

$$\mathbf{Q}_{ij} = \mathbf{Q}_{ij}^{0,p} - k_{ij(s)}^* \mathbf{u}_{ij(s)} \quad (4.5)$$

where $k_{ij(s)}^*$ denotes the effective shear stiffness of that contact. The reorientation of the contact area is modeled by $\mathbf{Q}_{ij}^{0,p} = \|\mathbf{Q}_{ij}^0\| \hat{\mathbf{t}}_{ij}$, where $\hat{\mathbf{t}}_{ij} = \mathbf{T}_{ij} \mathbf{Q}_{ij}^0 / \|\mathbf{T}_{ij} \mathbf{Q}_{ij}^0\|$, and

$\mathbf{T}_{ij} = \hat{\mathbf{I}} - \hat{\mathbf{r}}_{ij} \otimes \hat{\mathbf{r}}_{ij}$. For a contact with a boundary w , $\mathbf{T}_{iw} = \hat{\mathbf{I}} - \hat{\mathbf{n}}_w \otimes \hat{\mathbf{n}}_w$. The relative tangential displacement of grain i with respect to j , $\mathbf{u}_{ij(s)}$, is computed by Eqs. (3.2)–(3.3).

The shear stiffness, $k_{ij(s)}^*$, is evaluated from the theory of Mindlin & Deresiewicz [1953]. While cement prohibits relative sliding (“complete slip”) between the grains, we believe that partial slip, see Section 1.3.5.2, is important. We argue that the irregular surfaces of cemented contacts, see e.g. Section 4.2.2, are susceptible to slip. Additionally, slip along microcracks can reduce the lateral contact stress in a similar manner. In Mindlin & Deresiewicz [1953], slip is modeled by reducing the stiffness value predicted at initial loading or unloading (referred to as “no-slip”), until it vanishes at sliding, see Figure 3.2. Here, we simplify the treatment of slip by reducing the value predicted for no-slip, cf. Eq. (3.5a), by a fixed factor, C_s . Substituting the effective radius a_{ij}^* into Eq. (3.5a) provides the following effective stiffness:

$$k_{ij(s)}^* = C_s 8a_{ij}^* \left(\frac{2 - \nu_i}{G_i} + \frac{2 - \nu_j}{G_j} \right)^{-1} \quad (4.6)$$

Following Mindlin & Deresiewicz [1953], we vary the shear stiffness with the normal compression, through changes in the effective contact radius, a_{ij}^* .

4.4.3 Intergranular torques

A pair of grains, i and j , is loaded at a reference configuration by a torsional couple. The torque applied on grain i is denoted by $\mathbf{M}_{ij(t)}^0$. Following a perturbation, relative torsion between the grains, $\boldsymbol{\Omega}_{ij(t)}$, modifies the torque,

$$\mathbf{M}_{ij(t)} = \mathbf{M}_{ij(t)}^{0,p} - k_{ij(t)}^* \boldsymbol{\Omega}_{ij(t)} \quad (4.7)$$

where $\mathbf{M}_{ij(t)}^{0,p} = \left\| \mathbf{M}_{ij(t)}^0 \right\| \text{sgn} \left(\mathbf{M}_{ij(t)}^0 \cdot \hat{\mathbf{r}}_{ij} \right) \hat{\mathbf{r}}_{ij}$ accounts for the rotation of the contact area, see Figure 3.1(b). For a contact with a boundary, $\mathbf{M}_{iw(t)}^{0,p} = \left\| \mathbf{M}_{iw(t)}^0 \right\| \text{sgn} \left(\mathbf{M}_{iw(t)}^0 \cdot \hat{\mathbf{n}}_w \right) \hat{\mathbf{n}}_w$. The relative torsion, $\boldsymbol{\Omega}_{ij(t)}$, is computed by Eq. (3.7). The contact’s resistance to torsion is characterized by the effective stiffness $k_{ij(t)}^*$, evaluated from Deresiewicz [1954] assuming negligible slip, cf. Eq. (3.9a),

$$k_{ij(t)}^* = \frac{16}{3} (a_{ij}^*)^3 \left[\frac{1}{G_i} + \frac{1}{G_j} \right]^{-1} \quad (4.8)$$

Formally, partial slip in torsion should be modeled in a similar manner to that in the former section, e.g. by reducing the value in Eq. (4.8). However, since the contribution of

torsional couples to the averaged stress is negligible (see Section 3.5), such reduction has little effect on the results.

The tangential force, \mathbf{Q}_{ij} , is associated with a moment relative to the center of grain i , $\mathbf{M}_{ij(s)} = \mathbf{R}_{ij} \times \mathbf{Q}_{ij}$. The total moment relative to the center of the grain is

$$\mathbf{M}_{ij} = \mathbf{M}_{ij(s)} + \mathbf{M}_{ij(t)} \quad (4.9)$$

4.4.4 Evolution of the effective contact stiffness

4.4.4.1 Linear-elastic cement model

For grains bonded by weak cement, variations in the direct grain-grain contact area, e.g. as described in Hertz theory, may still be a significant source of nonlinearity. To explore the effect of the stiffness variations predicted by Hertzian theory on the bulk response, we formulate a “linear-elastic cement” model, in which the grain-grain portion of the contact area varies according to Eq. (2.1), whereas the cemented portion of the area remains fixed. The effective stiffness in the initial, undeformed configuration is computed by inserting the initial effective radius, cf. Eq. (4.4), into Eq. (4.3). The stiffness following deformations is evaluated by

$$a_{ij}^* = (R_{ij}h_{ij})^{1/2} + a_{ij}^{CEM} \quad (4.10)$$

In Hertz theory, if the grains separate, $h_{ij} \leq 0$, the intergranular force vanishes. In cemented contacts, separation should be resisted by tensile stresses. Thus, we assign a non-zero stiffness to contacts with $h_{ij} \leq 0$, computed by using $a_{ij}^* = a_{ij}^{CEM}$.

An alternative model, in which the nonlinear grain-grain and linear grain-cement interactions are treated independently, is presented in Section 4.7. Simulations reveal that both models underestimate the nonlinearity of the bulk response, for instance evaluating relatively small variations of the elastic moduli with increasing stress. A similar conclusion was made by Saidi et al. [2003].

4.4.4.2 Nonlinear cement deformation

To mimic the experimentally observed behavior, we model nonlinear cement deformation, e.g. caused by the mechanisms discussed in Section 4.2.2, by correlating the effective stiffness of each contact to the deformation it experiences. Following Hertz theory, we evaluate the contact’s deformation from the normal compression, through a single

parameter. We define a normal contact strain,

$$r_{ij}^* = \frac{r_{ij}^{(c)} - r_{ij}}{r_{ij}^{(c)}} \quad (4.11)$$

and relate the effective contact radius to this strain through an exponential function,

$$a_{ij}^* = a_{ij}^{*(c)} \exp(\gamma r_{ij}^*) \quad (4.12)$$

The effective stiffness increases from its initial value at the undeformed configuration, $a_{ij}^{*(c)}$, as the grains become closer, under compressive strain, $r_{ij}^* > 0$, and vice versa.

Exponential stiffness evolution was proposed by Potyondy [2007] to model cement dissolution in silicate rocks. The author simulated corrosion by a damage law, where the stiffness of each contact was reduced exponentially with increasing local stress. An exponential law for crack growth in brittle materials is observed in experiments and justified by theory, see Potyondy [2007] and the references therein.

For small ηr_{ij}^* values, the exponential function in Eq. (4.12) can be approximated by a power law, $(1 + \eta r_{ij}^*)^\omega \approx \exp(\gamma r_{ij}^*)$. Otherwise, for instance if the values of the parameters η and γ are large, or, following large deformations which correspond to large r_{ij}^* values, a power law will differ from an exponential law. To examine the ability of a power law to reproduce experimental data, we formulate the following relation:

$$a_{ij}^* = a_{ij}^{*(c)} (1 + \eta r_{ij}^*)^\omega \quad (4.13)$$

where $\eta \gg 1$ scales the effective radius with the contact strain, and ω determines its rate of change. The results of simulations using the different models are compared in Section 4.8.3.

4.5 Initial configuration

Simulations begin with an initial configuration of the grains. In Section 3.6.4.1 we show that simulations are sensitive to the way the initial configuration is generated. To reduce the dependence of the results on the generation procedure, we consider the initial configuration to be stress-free, and measure all intergranular deformations and loads relative to that configuration. Similar approach was taken by Potyondy & Cundall [2004], Tavarez & Plesha [2007] and Garcia & Medina [2007].

The assumption of initially unstressed cement is based on the hypothesis that cement accommodates to whatever surfaces are exposed at a given state, through pressure

dissolution [Dewers & Ortoleva, 1990; Garcia & Medina, 2007]: since stress is the driving force for dissolution, at contacts which experience higher stresses, dissolution will be enhanced. Once the dissolved material precipitates at these contacts, the effective contact area increases and thus stress is reduced. Similarly, in contacts which experience relatively low stresses, dissolution will be slower.

We create an initial, unstressed configuration from a dense irregular arrangement generated according to the procedure in Section 2.7.2. Cement is introduced by assigning an initial effective contact radius, cf. Eq. (4.4), *via* the parameter κ . To create a well-connected assembly of grains, we introduce cement between grains in close proximity. Close proximity is defined here by a separation distance between the grains which does not exceeds 10% of the grain radii, $h_{ij}^{(c)} \geq -0.1(R_i + R_j)$. For a grain i which is adjacent to grain j (or boundary w) however not in contact, $0 > h_{ij}^{(c)} \geq -0.1(R_i + R_j)$, we compute an initial effective radius by replacing the mutual approach $h_{ij}^{(c)}$ in Eq. (4.4) with h_i^{min} . The parameter h_i^{min} is the minimal mutual approach $h_{ij}^{(c)}$ among all *contacting* grains j . Note that, since the portion of the effective area in Eq. (4.10) associated with direct grain-grain contact, $(R_{ij}h_{ij})^{1/2}$, is allowed to vanish, a similar replacement of negative $h_{ij}^{(c)}$ values was not performed in generating the initial configuration for the elastic-cement model, cf. Section 4.4.4.1; instead, for grains with $0 > h_{ij}^{(c)} \geq -0.1(R_i + R_j)$, we assign $a_{ij}^{*(c)} = a_{ij}^{CEM}$.

4.6 Solution of the balance equations

At equilibrium, each grain satisfies the force and moment balance equations,

$$\mathbf{F}_i = \sum_{j=1}^{N_g^i} (\mathbf{P}_{ij} + \mathbf{Q}_{ij}) + \sum_{w=1}^{N_b^i} (\mathbf{P}_{iw} + \mathbf{Q}_{iw}) - m_i g \hat{\mathbf{e}}_z = \mathbf{0} \quad (4.14a)$$

$$\mathbf{M}_i = \sum_{j=1}^{N_g^i} (\mathbf{M}_{ij(s)} + \mathbf{M}_{ij(t)}) + \sum_{w=1}^{N_b^i} (\mathbf{M}_{iw(s)} + \mathbf{M}_{iw(t)}) = \mathbf{0} \quad (4.14b)$$

where \mathbf{F}_i and \mathbf{M}_i are the sum of forces and moments on grain i . We find the equilibrium configurations by minimizing the total work done against the loads on the grains, Π , with respect to the generalized coordinates, $\boldsymbol{\theta}$, computed by

$$\Pi(\boldsymbol{\theta}) = - \sum_{i=1}^N \left\{ \frac{1}{2} \sum_{j=1}^{N_g^i} W_{ij} + \sum_{w=1}^{N_b^i} W_{iw} - m_i g (\mathbf{u}_i \cdot \hat{\mathbf{e}}_z) \right\} \quad (4.15)$$

The parameter W_{ij} is the total work against the loads acting between grains i and j ,

$$W_{ij} = W_{ij(n)} + W_{ij(s)} + W_{ij(t)} \quad (4.16)$$

where $W_{ij(n)}$, $W_{ij(s)}$, and $W_{ij(t)}$ are the components of the total work associated with the normal and tangential forces, and torsional couples, respectively. These components are evaluated by integrating the product of the loads and generalized coordinates over the incremental displacements, see Section 3.4. Using the smallness of the incremental displacements, we linearize the constitutive rules in Section 4.4 by computing the intergranular loads based on the reference configuration, see Appendix A. Consequently, the terms in Eq. (4.16) are evaluated by numerical integration using a midpoint rectangular rule,

$$W_{ij(n)} = \mathbf{P}_{ij}^{0,p} \cdot \mathbf{u}_{ij(n)} - \frac{1}{2} k_{ij(n)}^* \|\mathbf{u}_{ij(n)}\|^2 \quad (4.17a)$$

$$W_{ij(s)} = \mathbf{Q}_{ij}^{0,p} \cdot \mathbf{u}_{ij(s)} - \frac{1}{2} k_{ij(s)}^* \|\mathbf{u}_{ij(s)}\|^2 \quad (4.17b)$$

$$W_{ij(t)} = \mathbf{M}_{ij(t)}^{0,p} \cdot \boldsymbol{\Omega}_{ij(t)} - \frac{1}{2} k_{ij(t)}^* \|\boldsymbol{\Omega}_{ij(t)}\|^2 \quad (4.17c)$$

A local minimum of Π is obtained numerically, see Appendix A. The gradient of Π with respect to $\boldsymbol{\theta}$, $\nabla_{\boldsymbol{\theta}} \Pi = -[\mathbf{F}_1 \dots \mathbf{F}_N \quad \mathbf{M}_1/R_1 \dots \mathbf{M}_N/R_N]^T$, equals the sum of forces and moments. Thus, the coordinates $\boldsymbol{\theta}$ which make the gradient vanish at a local minimum of Π , satisfy the balance equations, cf. Eq. (4.14).

4.7 The parallel bond model

In this section, we present a “parallel bond” model², in which the intergranular loads are computed by superimposing two independent components, related to: (a) direct grain-grain contact; and (b) grain-cement contact. Thus, two sets of constitutive rules are presented. This approach allows use of the contact mechanics theories for component (a). For the grain-cement component, we follow Potyondy & Cundall [2004] and formulate a constitutive rule based on the approximation of cement as a linear-elastic cylindrical beam. The parallel bond model is developed using QuSGM to examine the hypothesis that Hertzian contacts are the main source of nonlinearity in weakly-cemented materials.

²We borrow the term parallel bond from the work of Potyondy & Cundall [2004].

4.7.1 Constitutive rules for intergranular interactions

The intergranular loads associated with the grain-grain contact are computed by Hertz theory, assuming ideally smooth grains. Thus, frictional loads are associated with cement deformation alone. The motivation to neglect frictional loads associated with the grain-grain contact is based on the following hypothesis: the resistance to intergranular shear, tension and torsion is mostly supported by the cement material, whereas compression is mostly carried by the grains themselves.

We evaluate the loads associated with the cement deformation by modeling the cement between each pair of grains as homogeneous, isotropic, linearly-elastic cylinder, which can undergo compression, extension, and torsion³. The relations between the loads and the cylinder's deformations are obtained from the published analytical solutions [Timoshenko & Goodier, 1970] to the following boundary-value problem: find the stresses on the end-faces of an elastic cylinder, with (1) prescribed displacements and rotations of the end-faces, assuming they remain parallel; and (2) zero tractions on its lateral boundaries. Our model does not account for cement and grain fracturing or breakage. Cement deformation is computed relative to an initial configuration, in which *cement* is assumed undeformed, cf. Section 4.5. Note that, in contrast with the models in Section 4.4, here the *grains* themselves are considered stressed at the initial configuration.

4.7.1.1 Normal and tangential force components

To relate the cement deformation to the relative displacements and rotations of the grains, we model cement at a contact by a cylinder pinned to each grain by a “cementing point”. Consider a pair of grains, i and j . The cementing points associated with these grains, $\boldsymbol{\xi}_{ij}$ and $\boldsymbol{\xi}_{ji}$, are at the center of the cylinder's end-faces, see Figure 4.6. At the initial, undeformed configuration, denoted by superscript (c) , both points overlap at the center of the contact area,

$$\boldsymbol{\xi}_{ij}^{(c)} = \boldsymbol{\xi}_{ji}^{(c)} = \mathbf{r}_i^{(c)} + \mathbf{R}_{ij}^{(c)} \quad (4.18)$$

The location of the cementing points following deformation, $\boldsymbol{\xi}_{ij}$, is evaluated in an incremental fashion: given the location of these points at a reference configuration, $\boldsymbol{\xi}_{ij}^0$, their

³We assume that the longitudinal dimension of the cement is much smaller than its lateral extent, and do not account for bending or flexure.

current location is computed by

$$\boldsymbol{\xi}_{ij} = \boldsymbol{\xi}_{ij}^0 + \mathbf{u}_i + \boldsymbol{\Omega}_i \times \mathbf{R}_{ij}^0 \quad (4.19)$$

For an exterior grain i , interactions with the boundaries are computed in a similar manner: the cementing point on a boundary w , $\boldsymbol{\xi}_{wi}$, is found by substituting \mathbf{u}_i with \mathbf{u}_w and putting $\boldsymbol{\Omega}_w = 0$ in Eq. (4.19).

The average axial stress on the cylinder's end-faces, σ_a , is computed from a one dimensional form of Hooke's law, $\sigma_a = \bar{E}_{ij}\epsilon_a$ [Timoshenko & Goodier, 1970], where \bar{E}_{ij} is Young's modulus of the cement material. Overbar denotes a property of the cement. The axial strain, ϵ_a , is evaluated from the relative displacement of the cementing points measured from the initial configuration, normalized by the characteristic longitudinal extent of the cement. Here, the longitudinal and lateral extent of the cement, \bar{L}_{ij} and \bar{R}_{ij} , are the cylinder's length and radius, see Figure 4.6(a). Following Potyondy & Cundall [2004], we relate the longitudinal and lateral extent of the cement to the grain sizes, through $\bar{L}_{ij} = \lambda^L R_{ij}$ and $\bar{R}_{ij} = \lambda^R R_{ij}$. The dimensionless parameters $\lambda^L \ll 1$ and $\lambda^R \ll 1$ are related to the cement content and geometry, and are assumed uniform for all contacts. The flattened shape of the pore space near a contact between spherical grains, cf. Figure 4.5, suggests that $\lambda^L/\lambda^R < 1$.

Since the cementing points initially overlap, the relative displacement since the initial configuration is $\boldsymbol{\xi}_{ij} - \boldsymbol{\xi}_{ji}$. The strain and stress are compressive if the grains approach each other, and tensile otherwise. The magnitude of the resultant force, $\|\mathbf{F}_{ij}\| = \bar{A}_{ij}\bar{E}_{ij}\|\boldsymbol{\xi}_{ij} - \boldsymbol{\xi}_{ji}\|/\bar{L}_{ij}$, is the product of the stress and the cross-sectional area, $\bar{A}_{ij} = \pi(\bar{R}_{ij})^2$. The force applied on grain i by the deformation of the cement with grain j , \mathbf{F}_{ij} , is directed along the line connecting the cementing points, $\boldsymbol{\xi}_{ij} - \boldsymbol{\xi}_{ji}$,

$$\mathbf{F}_{ij} = -\pi(\bar{R}_{ij})^2 \bar{E}_{ij} \frac{\boldsymbol{\xi}_{ij} - \boldsymbol{\xi}_{ji}}{\bar{L}_{ij}} \quad (4.20)$$

We note that, if the force \mathbf{F}_{ij} is not aligned with the grains centerline, \mathbf{r}_{ij} , the force acting on grains i and j includes both normal and tangential components.

4.7.1.2 Torque

Relative twist of the grains deforms the cement in torsion, applying a torsional couple on the grains. Torsion of cement between grains i and j applies the following

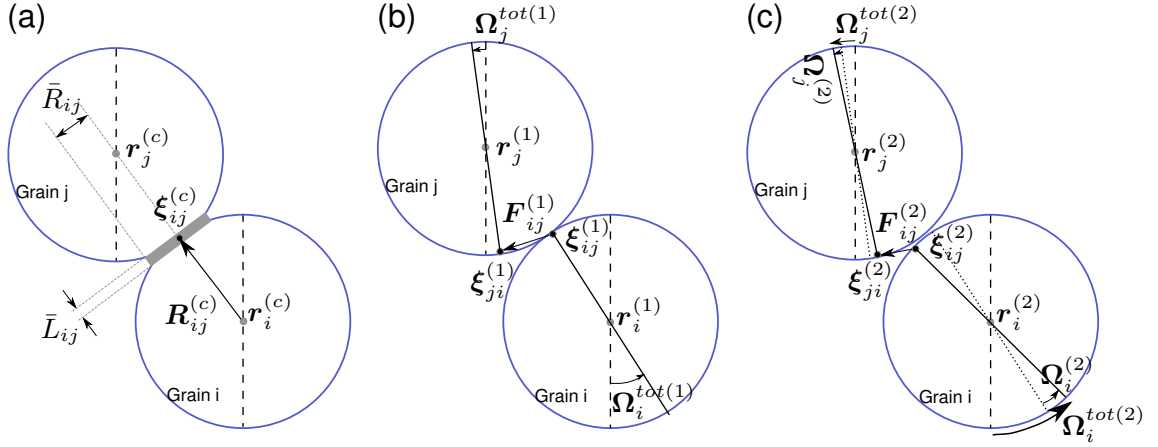


Figure 4.6: Schematic description of a pair of cemented grains: (a) initial configuration (denoted by superscript (c)), with undeformed cement (in grey); (b) a subsequent configuration, (1), following a perturbation. The cement deformation is associated with a pair of forces \mathbf{F}_{ij} and \mathbf{F}_{ji} , acting on grains i and j , respectively; and (c) a subsequent configuration, (2), following perturbation of configuration (1). Also shown are the incremental and total rotations, Ω_i and Ω_i^{tot} , measured from the former (*reference*) and the *initial* configurations, respectively. The solid, dotted and dashed lines mark the *current*, *reference*, and *initial* grain orientation, respectively.

torsional couple on grain i [Timoshenko & Goodier, 1970]:

$$\mathbf{M}_{ij(t)} = -\frac{1}{2}\pi (\bar{R}_{ij})^4 \bar{G}_{ij} \frac{\Omega_{ij(t)}^{tot}}{\bar{L}_{ij}} \quad (4.21)$$

where \bar{G}_{ij} is the shear modulus of the cement material, and $\Omega_{ij(t)}^{tot}$ denotes the total torsion since cement was deposited. We evaluate the torsional deformation of the cement as the component of relative rotation of the grains which is aligned with the grains centerline⁴. Thus, $\Omega_{ij(t)}^{tot}$ is evaluated by substituting the incremental rotations Ω_i and Ω_j in Eq. (3.7) with the rotations measured since cement deposition, Ω_i^{tot} and Ω_j^{tot} , see Figure 4.6.

Additional moment is associated with the force, $\mathbf{M}_{ij(s)} = (\boldsymbol{\xi}_{ij} - \mathbf{r}_i) \times \mathbf{F}_{ij}$. The total moment relative to the center of grain i , caused by deformation of the cement bonding it to grain j , is

$$\mathbf{M}_{ij} = \mathbf{M}_{ij(s)} + \mathbf{M}_{ij(t)} \quad (4.22)$$

We note that $\mathbf{M}_{ij(s)} = \mathbf{0}$ if the force \mathbf{F}_{ij} is aligned with the grains centerline, \mathbf{r}_{ij} .

⁴This formulation ignores the change in the direction of the cement cylinder, assuming small grain rearrangements since cement deposition. Otherwise, if large relative rotations or lateral displacements occur, relative torsion of the *grains* may result in other modes of *cement* deformation; since intergranular torsion has negligible effect on the macroscopic stresses [Goddard, 1990], the related error is insignificant.

4.7.2 Equilibrium configurations

The equilibrium configurations are sought in a similar manner to that described in Sections 2.5 and 4.6. The balance equations for the forces and moments on grain i are

$$\mathbf{F}_i = \sum_{j=1}^{N_g^i} (\mathbf{P}_{ij} + \mathbf{F}_{ij}) + \sum_{w=1}^{N_b^i} (\mathbf{P}_{iw} + \mathbf{F}_{iw}) - m_i g \hat{\mathbf{e}}_z = 0 \quad (4.23a)$$

$$\mathbf{M}_i = \sum_{j=1}^{N_g^i} (\mathbf{M}_{ij(s)} + \mathbf{M}_{ij(t)}) + \sum_{w=1}^{N_b^i} (\mathbf{M}_{iw(s)} + \mathbf{M}_{iw(t)}) = 0 \quad (4.23b)$$

The energy functional Π is evaluated from the potential energy of the pack,

$$\Pi(\boldsymbol{\theta}) = \sum_{i=1}^N \left\{ \frac{1}{2} \sum_{j=1}^{N_g^i} U_{ij} + \sum_{w=1}^{N_b^i} U_{iw} + m_i g (\mathbf{r}_i \cdot \hat{\mathbf{e}}_z - z^*) \right\} \quad (4.24)$$

where the strain energy U_{ij} stored in the deformed contact region between grains i and j , including both the grain and cement material, is

$$U_{ij} = U_{ij(n)} + U_{ij(F)} + U_{ij(t)} \quad (4.25)$$

Here, $U_{ij(n)}$ denotes the strain energy related to direct grain-grain contact, cf. Eq. (2.6). The strain energy stored in the deformed cement is evaluated by integrating the intergranular loads in Eqs. (4.20)–(4.21), over the respective displacements. The energy related to the compression/tension and torsion, $U_{ij(F)}$ and $U_{ij(t)}$, is computed by

$$U_{ij(F)} = \frac{\pi (\bar{R}_{ij})^2 \bar{E}_{ij}}{2 \bar{L}_{ij}} \|\boldsymbol{\xi}_{ij} - \boldsymbol{\xi}_{ji}\|^2 \quad (4.26a)$$

$$U_{ij(t)} = \frac{\pi (\bar{R}_{ij})^4 \bar{G}_{ij}}{4 \bar{L}_{ij}} \|\boldsymbol{\Omega}_{ij(t)}^{tot}\|^2 \quad (4.26b)$$

4.8 Simulations of a deforming weakly-cemented sample

4.8.1 Reproduction of experimental data

In this section, we demonstrate the ability of the exponential stiffness evolution law in Section 4.4.4.2 (“exponential model”) to reproduce experimental data. In most experiments, the effect of cement content is of interest; thus, measurements are performed at a given stress state on samples with different cement content, see, e.g., Dvorkin et al.

[1994], Berge et al. [1995], Dvorkin et al. [1999], and Holt et al. [2005]. Here, to observe the change in properties with deformation, we use data obtained by measurements in a single sample, at different loads [Saidi et al., 2003; Nakagawa, 2008].

Saidi et al. [2003] applied uniaxial stress on a synthetic sandstone made of quartz grains bonded by Portland cement. The dry cement weight was 28.5% of the total sample's dry weight. Young's modulus was estimated from the slope of the unloading portion of unloading-reloading cycles performed at different stresses, see Figure 4.1. The load was increased beyond the sample's failure strength. Thus, the data in Figure 4.7 includes pre- and post-failure behavior, marked by a decrease in the growth rate of moduli with stress, and a decrease in the moduli values following failure.

Nakagawa [2008] measured acoustic compressional and shear wave velocities in quartz grains cemented by soda-lime glass under uniaxial stress, see Figure 4.2. We estimate Young's modulus from the velocities, porosities and densities, cf. Eq. (2.20). The data in Figure 4.7 corresponds to a sample with 30.4% porosity, reduced from an initial value of 35% by addition of cement. The figure shows a loading-unloading cycle, with slightly higher velocities during unloading.

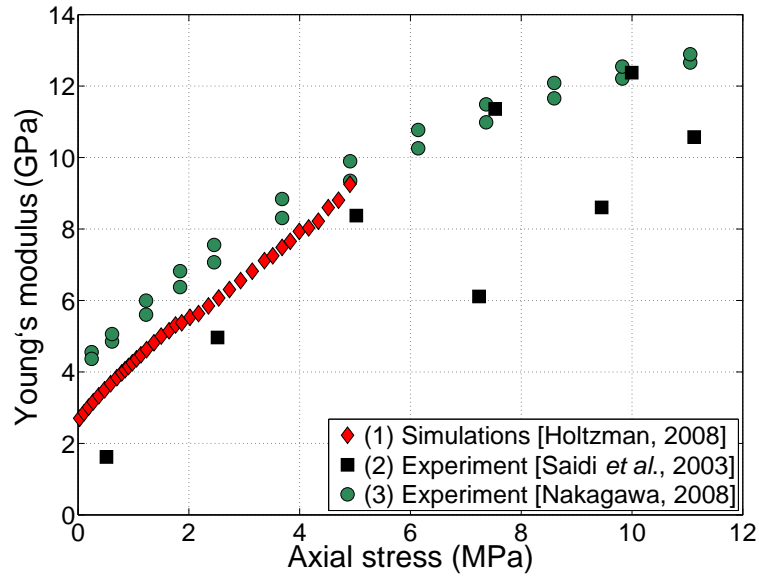


Figure 4.7: Effective Young's modulus, E , vs. axial stress, σ_a , obtained from: (1) simulations of uniaxial test of sample *Q2699-1*%, using the exponential stiffness evolution model with $\gamma=3000$; (2) uniaxial compression of quartz grains bonded by Portland cement [Saidi et al., 2003]; and (3) acoustic testing of quartz grains cemented by soda-lime glass [Nakagawa, 2008]. The strong nonlinearity, evident as an increase of the stiffness E with the stress, is reproduced by our model.

We simulate the above experiments by loading sample *Q2699-1%*, where *Q2699* denotes a pack of 2699 grains made of quartz, and the percentage after the dash represents the value of κ , 0.01. The initial packing was created by introducing cement into a pre-compacted pack, generated by isotropic compression to a stress of $\sigma_c^{\mu=0}=10$ MPa, as described in Section 4.5. The intergranular stiffness evolution is characterized by $\gamma=3000$, cf. Eq. (4.12). To model partial slip, we use a factor of $C_s=1/10$ in Eq. (4.6); the evaluation of C_s is discussed in Section 4.8.4.2. Uniaxial stress is applied through compressive axial strain increments, $\Delta\epsilon_a$, with Poisson's expansion of 0.25, i.e. tensile lateral strains of $0.25\Delta\epsilon_a$. Unless stated otherwise, similar initial packing, loading scheme, and C_s value were used in all the simulations presented in this chapter.

The good agreement in Figure 4.7 between the computed and the experimentally-measured Young's modulus (E), demonstrates that nonlinear microscopic deformation mechanisms, cf. Section 4.2.2, play a significant role in determining the bulk response. Conversely, in Section 4.8.3 we show that the other models proposed in this chapter could not reproduce the experimental data, predicting relatively linear-elastic behavior, regardless of the choice of model parameters.

Note that, since our model accounts for initial stages of loading only, we do not extend our simulations beyond stresses of ~ 5 MPa. At larger stresses, closer to the sample's strength, deformation mechanisms such as fractures formed by coalescing microcracks may become important [Jaeger & Cook, 1979; Martin & Chandler, 1994; Berge et al., 1995; David et al., 1998; Nakagawa & Myer, 2001; Holt, 2001; Saidi et al., 2003]. The effect of such mechanisms is not included in our model.

4.8.2 Examination of the performance of the numerical algorithm

To improve the performance of the minimization algorithm employed in finding the equilibrium configurations, we use the smallness of the incremental displacements and linearize the constitutive relations. Linearization is performed by: (a) fixing the grain locations in evaluating the intergranular loads; followed by (b) an update of the geometry based on the solution in (a), resolving for the loads, see Appendix A. To demonstrate the enhanced performance achieved by linearizing the constitutive rules, we compare the numerical and analytical solutions obtained for a regular packing undergoing self-similar deformations, see Section 2.7.3.1.

The numerical error for a model with $\gamma=0$, measured as the deviation from self-similar deformation, $(r_{ij}^A - r_{ij}^N) / r_{ij}^A$, is of the order of the machine's floating-point relative accuracy, even for large self-similar strain of $\varepsilon=0.2$. This error is smaller by several orders of magnitude compared to that produced by the simulations using nonlinear rules, cf. Sections 2.7.3.1 and 3.6.3.1. Moreover, simulations here predicted negligible⁵ grain rotations, in correspondence with the analytical solution, whereas the numerical solution in Section 3.6.3.1 predicted rotations of $\sim 10^{-9}$.

4.8.3 Comparison of intergranular constitutive rules

To examine the effect of the constitutive rules on the computed bulk response, we compare the results produced by the different rules described in Sections 4.4 and 4.7.1. In Figures 4.8–4.9 we present the stress-strain curves and corresponding Young's modulus values evaluated from simulations using the following models: (1) *Q2699-1%*($\gamma=3000$) - exponential model; (2) *Q2699-1%*($\eta=1111, \omega=1$) - power law, see Eq. (4.13); (3) *Q2699-1%*($\gamma=0$) - fixed intergranular stiffness; (4) *Q2699-1%*(Elastic cement) - assuming linear-elastic cement, see Section 4.4.4.1; and (5) *Q2699-G*(Parallel bond) - parallel bond model, cement material assigned with elastic moduli of glass ($\bar{E}_{ij}=70$ and $\bar{G}_{ij}=29.2$ MPa), with $\lambda^R=0.003$ and $\lambda^L=0.001$, see Section 4.7.

The deviatoric stress, σ_d , computed as the difference between the axial and lateral stresses, is plotted in Figure 4.8 *vs.* the axial strain, ϵ_a . Deviatoric rather than axial stress is used for comparison, because the latter is initially nonzero in the parallel bond model; the initial pack carries confining stresses of $\sigma_c=10$ MPa. Only the exponential model, (1), yields a stress-strain curve with significant convexity. Such convexity, corresponding to strain-hardening, is observed in experiments, see Section 4.2.1. The other models, (2) and (4)–(5), produce a more linear response⁶. In particular, assigning $\omega=1$ provides a quadratic relation between the macroscopic stress and the strain. Quadratic dependence is expected since the stress and strain are approximately linear with the intergranular forces and displacements, respectively, while the forces themselves are linear with the displacements. Finally, we demonstrate that the assumption of linearly-elastic contacts together with a fixed contact

⁵The rotations are of the order of the machine's floating-point relative accuracy.

⁶The slope of the stress-strain curve and the corresponding moduli computed by model (4) are lower than in models (1)–(3), because of differences in generating the initial sample: in model (4), only grains in direct contact are “cemented”, whereas in models (1)–(3) cement is introduced between all grains in close proximity, see Section 4.5.

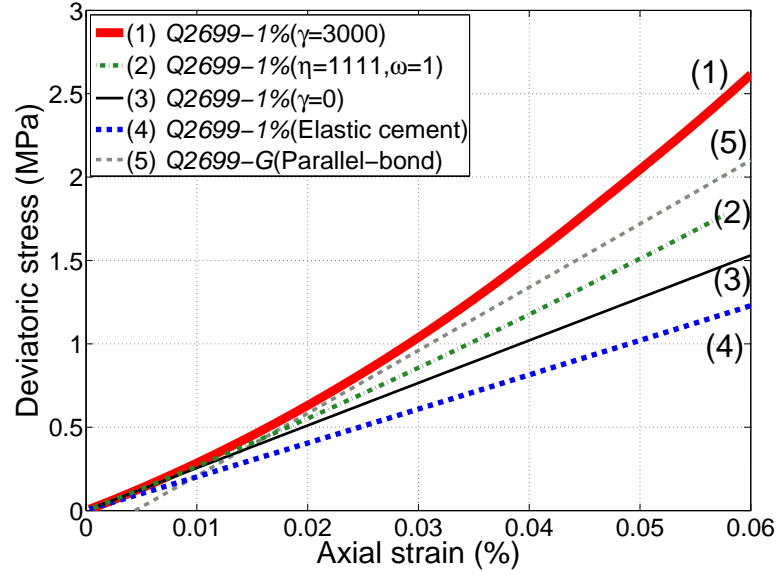


Figure 4.8: The deviatoric stress, σ_d , vs. axial strain, ϵ_a , evaluated by simulating uniaxial test on sample *Q2699* using different intergranular constitutive rules. The strong nonlinearity observed in experiments is reproduced by the exponential model (1) alone.

network, (3), yields a linearly-elastic material. The stress-strain curve is practically⁷ linear, and the moduli remain constant.

To quantify the nonlinearity of the bulk response, in Figure 4.9 we plot the evolution of Young's modulus with the applied stress, computed from the stress-strain curves in Figure 4.8. Only the exponential model, (1), is able to reproduce the experimental data. Since models (3)–(5) do not account for the inelastic contact deformation mechanisms discussed in Section 4.2.2, the computed variations of the moduli are small. The account for these mechanisms in the linear stiffness evolution model, (2), by using $\omega=1$ appears to be insufficient. We stress that models (2)–(5) cannot reproduce the experimental data, regardless of the values selected for the other parameters, η , \bar{E}_{ij} , \bar{G}_{ij} , λ^R and λ^L . In particular, our results confirm that the assumption underlying models (4) and (5), namely that the main source of nonlinearity is nonlinear deformations of the *grain* material, computed *via* Hertzian model, is invalid [Saidi et al., 2003]. In the following section we examine the effect of the stiffness evolution parameters, γ , η and ω on the bulk response.

⁷A geometrical nonlinearity is associated with changes in the directions of the intergranular loads with the deformation; however, its effect is negligible.

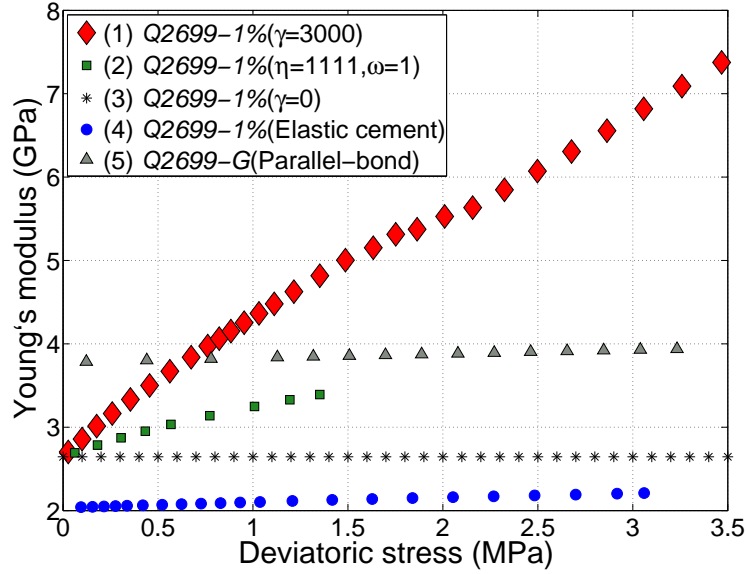


Figure 4.9: Effective Young's modulus, E , *vs.* deviatoric stress, σ_d , computed from the stress-strain curves in Figure 4.8. Only the exponential model (1) is in good agreement with experimental data, see Figure 4.7.

4.8.4 Sensitivity analysis

4.8.4.1 Effect of the stiffness evolution parameters

The value of the exponent γ (or, equivalently, ω) determines the rate of strain hardening. Thus, γ and ω represent the rate in which the microcracks close, better contact is achieved, or the effect of compression reaches stiffer portions of the grains and cement materials. The value of the exponent that provided good agreement with the experimental data, $\gamma = 3000$, was found by trial and error. For other samples, e.g. with different grains, cement material and quantity, microstructure and density, a different value may apply.

Figure 4.10 shows Young's modulus, E , *vs.* axial stress, σ_a , evaluated from simulations of a uniaxial test on sample *Q2699-1%* using the following parameters: (1) $\gamma=3000$; (2) $\gamma=1000$; (3) $\eta=1428, \omega=2$; (4) $\eta=1428, \omega=1$; and (5) $\eta=1111, \omega=1$. The similarity of results (2) and (5) demonstrate the equivalence of the exponential and the power law models at low ηr_{ij}^* values, see Section 4.4.4.2. Conversely, the larger η and γ values employed in (1) and (3) result in significantly different moduli. The divergence between curves (1) and (3) increases with the deformation, since, on average, the values of r_{ij}^* become larger. Results (4) and (5) show the relatively small effect of η on the moduli growth rate, i.e. the

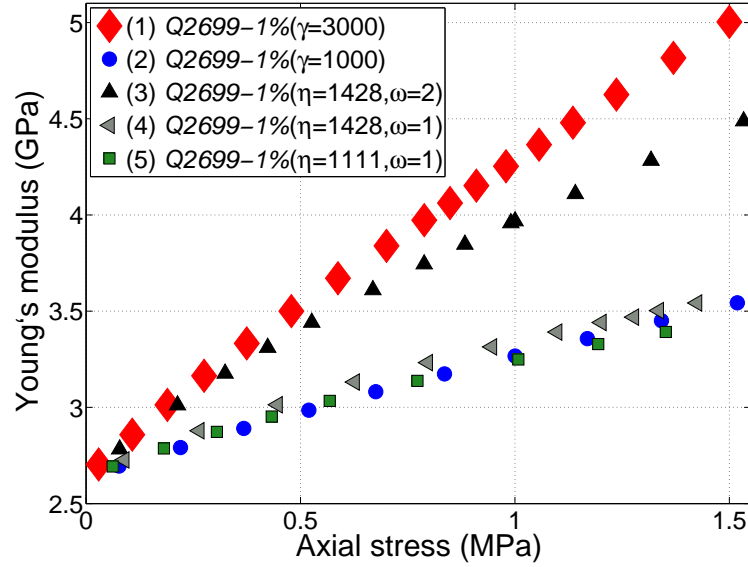


Figure 4.10: Effective Young's modulus, E , vs. axial stress, σ_a , computed from simulations of uniaxial test on sample *Q2699-1%*, employing different stiffness rules and parameters.

strain hardening. Thus, in a linear stiffness evolution model ($\omega=1$), by virtue of increasing η alone, it is impossible to match the experimental data.

4.8.4.2 Sensitivity to the intergranular tangential stiffness

In Section 4.4.2 we have discussed the occurrence of partial slip in cemented contacts. Following Mindlin & Deresiewicz [1953], we model slip by reducing the tangential stiffness from its initial value, which corresponds to negligible slip. The reduction of the stiffness is quantified here by the factor C_s . To study the effect of $k_{ij(s)}^*$ on the bulk response, in Figure 4.11 we compare Young's modulus, E , computed by simulating uniaxial test on sample *Q2699-1%* with $\gamma=3000$, assuming: (a) complete slip, $C_s=0$ (i.e., $k_{ij(s)}^*=0$); (b) partial slip, $C_s=1/10$; and (c) no-slip, $C_s=1$. As expected, the modulus E increases with the intergranular stiffness, $k_{ij(s)}^*$. To reproduce the experimental data, a factor of $C_s=1/10$ was determined by trial and error. By assuming complete slip, E was underestimated. Conversely, the no-slip assumption results in overestimated moduli, regardless of the stiffness evolution law employed. These results imply that in weakly-cemented materials, slip along microcracks within the cement or at the irregular surfaces of the cemented contacts, cf. Section 4.2.2, should be accounted for.

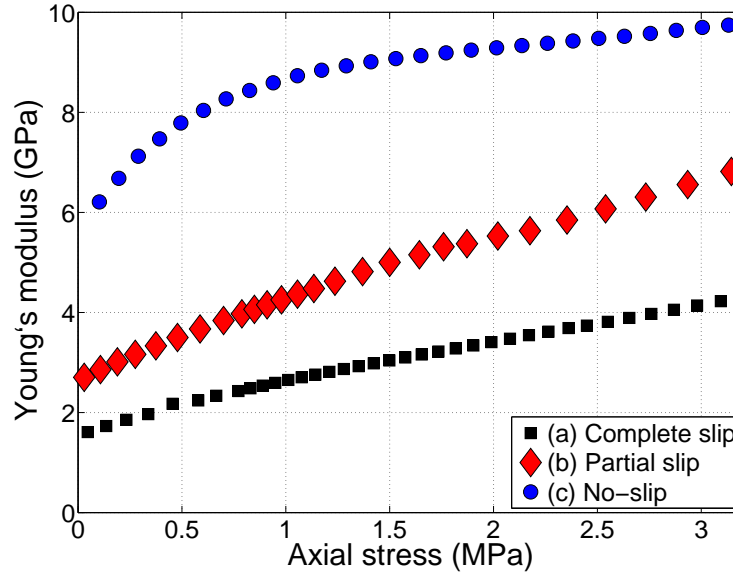


Figure 4.11: Effective Young's modulus, E , vs. axial stress, σ_a , computed from simulations of uniaxial test on sample $Q2699-1\%$ with $\gamma=3000$, assuming: (a) complete slip, $C_s=0$; (b) partial slip, $C_s=1/10$; and (c) no-slip, $C_s=1$.

4.8.4.3 Impact of the cement content

In this section, we discuss the impact of the parameter κ on the sample's effective properties. In our model, κ characterizes the initial effective contact radius, cf. Eq. (4.4). Since the contact stiffness is parameterized by the effective radius, κ is a function of the cement content, as well as its geometry and material properties. Here, we compare two samples with similar cement material, which differ by their degree of cementation. Since we consider cement which is deposited *only* around the grain contacts, larger cement quantities correspond to larger cemented contact area, i.e. larger κ values. In Figure 4.12 we present Young's modulus computed from the simulations of uniaxial test on two samples: (a) $Q2699-1\%$, with $\kappa=0.01$; and (b) $Q2699-20\%$, with $\kappa=0.2$. The exponential stiffness model was employed, with $\gamma=3000$.

Since κ characterizes the *initial* effective stiffness, at low stresses the moduli evaluated for sample $Q2699-20\%$ are approximately 20% larger than for $Q2699-1\%$. The difference between the moduli evaluated for the two samples reduces with further loading, implying that the moduli growth rate with stress in $Q2699-20\%$ is slightly lower than in $Q2699-1\%$. We attribute the faster strain hardening exhibited by $Q2699-1\%$ to the smaller

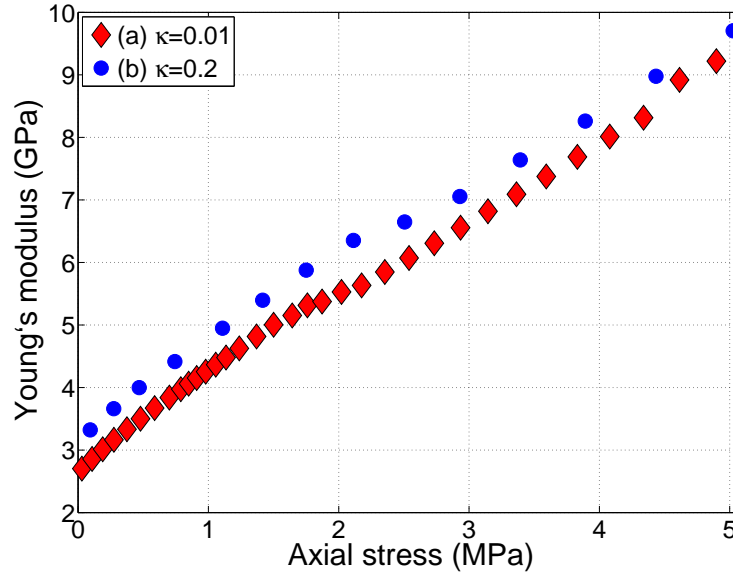


Figure 4.12: Effective Young’s modulus, E , vs. axial stress, σ_a , computed from simulations of uniaxial test on two samples with different cement content: (a) $\kappa=0.01$ and (b) $\kappa=0.2$. While larger moduli are evaluated for sample (b), the moduli growth rates are relatively similar to those in (a).

constraint posed by the smaller cement content on grain rearrangements.

This correlation between cement content and overall stiffness is in qualitative agreement with experiments [Dvorkin et al., 1994; David et al., 1998; Dvorkin et al., 1999; Nakagawa & Myer, 2001; Saidi et al., 2003; Holt et al., 2005; Nakagawa, 2008]. We note that at large cement contents, the increase in bulk stiffness with the degree of cementation is less evident; this is because some of the cement is deposited far away from the contacts, thus having smaller effect on the mechanical properties [Dvorkin et al., 1999; Garcia & Medina, 2007]. Conversely, experiments and theory show that introduction of even small amounts of soft cement at the grain contacts, significantly increases the sample’s stiffness [Bernabè et al., 1992; Garcia & Medina, 2007]. Similar conclusion is made from our simulations. For instance, the Young’s modulus values computed for sample *Q2699-1%* with $\gamma=3000$, ~ 2.7 – 9.5 GPa, are significantly larger than those evaluated by our models of uncemented materials. The moduli predicted by the frictional (Section 3.6.3.2, for sample *G2740*) and frictionless (Section 2.7.3.2, *G5036*) models are ~ 1.3 – 1.5 and ~ 0 – 0.6 GPa, respectively. The stiffer response computed for the cemented sample is attributed to the constraints imposed by the cement on grain rearrangements [Bernabè et al., 1992; Garcia & Medina, 2007]; the increase in the contact radius, and the corresponding contact stiffness, is small.

4.9 Concluding remarks

We have studied the mechanics of weakly-cemented granular materials, in which the grains are bonded together by small amounts of cement, *via* grain-scale simulations. We have sought to identify the micromechanical origins of the nonlinear deformation exhibited by cemented sediments [Murphy, 1982; Martin & Chandler, 1994; Saidi et al., 2003; Nakagawa, 2008]. The effect of possible microscopic deformation mechanisms is modeled within the framework of QuSGM, through several suites of constitutive relations. Particularly, we propose the following mechanisms for nonlinear contact deformation: closure and opening of microcracks, changes in the geometry of the cemented contacts, and propagation of the deformation into heterogeneous cement and grain materials. The effects of these mechanisms are modeled by varying the stiffness of each contact according to the local deformation. The contact stiffness is evaluated from the contact mechanics theories of Hertz, Mindlin, and Deresiewicz, modified to accommodate the cohesion introduced by the cement.

The results of simulations reveal that an account of nonlinear deformations at the grain-scale is required to reproduce the nonlinear bulk response. In particular, a model which links the intergranular stiffness and the local deformations through an exponential function, is shown to match experimental data. An exponential relation was found adequate to describe crack growth in brittle materials, see Potyondy [2007] and the references therein. Conversely, models based on the concept of linear-elastic cement deformation, where the main source of nonlinearity is the *grain* deformation, i.e. Hertzian contacts, fail to reproduce the experimentally-observed nonlinearities. Similar conclusion was made by Saidi et al. [2003]. These results find immediate application in modeling geological systems containing poorly-consolidated sedimentary rocks, such as oil and water reservoirs.

Chapter 5

Impact of hydrate dissociation in marine sediments

5.1 Introduction

GAS-HYDRATES are crystalline solids composed of water molecules arranged into a rigid framework of cages, each occupied by a gas molecule. In this chapter, we use grain-scale simulations to investigate the impact of hydrate dissociation on the properties of marine sediments. Hydrates form under relatively high pressures and low temperatures, with sufficient supply of gas [Sloan, 1998, 2003], see Figure 5.1. Methane hydrates, the most common type occurring in nature [Sloan, 2003], form in the uppermost tens to hundreds of meters of sediments in permafrost regions and marine continental margins [Kvenvolden et al., 1993; Kvenvolden, 1998; Davie & Buffett, 2001], see Figure 5.2.

There is considerable growth of interest in hydrates, stemming from several reasons. First, methane hydrates contain a large fraction of the earth's fossil fuels: even conservative estimates suggest that the amount of energy in hydrates is equivalent to twice that of all other fossil fuels combined [Sloan, 2003; Ruppel, 2007]. The large methane quantity constitutes a promising energy resource [Sloan, 2003] and plays an important role in the global carbon cycle [Dickens, 2003]. Secondly, if the conditions in which hydrates are stable, see Figure 5.1, cease to exist, hydrates dissociate into liquid water and free gas. Dissociation can be accompanied by an appreciable increase in pore pressure caused by volumetric expansion of the gas [Xu & Germanovich, 2006]. Hydrate dissociation in the ocean floor has been linked to massive submarine slope failures and landslides [Paull et al., 2003; Sultan et al., 2004]. Such events present a geohazard during oil recovery [Rutqvist

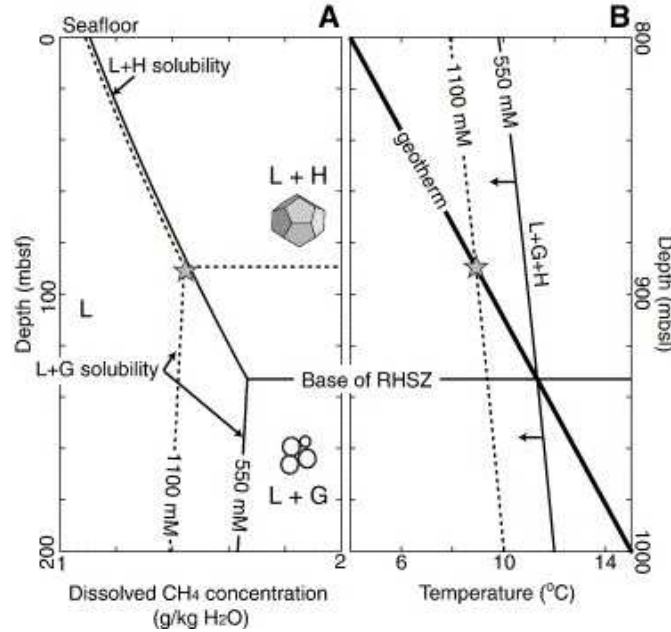


Figure 5.1: Diagram showing (A) methane solubility; and (B) temperature for hydrate-gas-brine equilibrium, as a function of depth, for two salinities (550 mM being that of seawater). Methane hydrate (H) and methane gas (G) exist only if the methane concentration exceeds solubility. The peak in solubility determines the bottom end of the hydrate stability zone (HSZ), see Figure 5.2. The diagram assumes water depth of 800 m, hydrostatic pressure gradient of 10 MPa/km, seafloor temperature of 4°C and geothermal gradient of 55°C/km. Abbreviations mbsf and mbsl denote meters below sea floor and level. Adapted from Liu & Flemings [2006].

& Moridis, 2007] and a source of methane during rapid intervals of climatic changes which could affect global warming [Dickens, 1999]. Finally, hydrate formation and dissociation has a crucial impact on flow assurance in oil and gas production: hydrate formation can plug pipelines, while dissociation can lead to pipeline blowouts and bursts [Sloan, 2003].

5.1.1 Natural formation of methane hydrates

The presence of methane hydrates in marine sediments is commonly explained through the following conceptual model [Dickens, 2003]: methane of biogenic or thermogenic origin is generated in deep oceanic sediments, where the temperature is high enough for the methane to be a gas. Methane bubbles grow and coalesce, eventually having sufficient buoyancy for upwards migration. In the shallow sediments, however, where the temperature is much colder, the methane stimulates formation of hydrates. Hydrate-bearing sediments (HBS) form a region denoted as the hydrate stability zone (HSZ), see Figure 5.2.

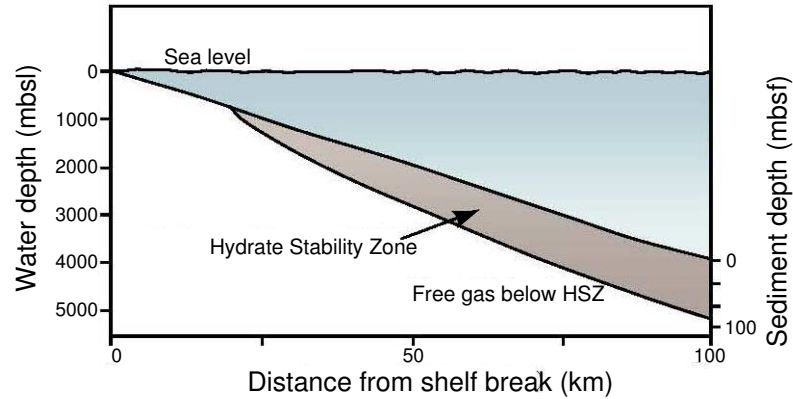


Figure 5.2: Idealized cross section of the hydrate stability zone (HSZ) along a continental shelf. The thickness of the HSZ increases with the depth of the sea floor. Adapted from Dickens [2003].

5.1.2 Hydrate distribution within the pore space

Hydrate distribution depends on the hydrate formation mechanism, type of guest gas molecule, and host sediment [Durham et al., 2005]. Experimental evidence suggests that hydrates form preferentially in the pore bodies if the guest gas is dissolved in water [Tohidi et al., 2001; Yun et al., 2005, 2007], whereas percolation of free gas is associated with hydrate formation around the grain contacts first, followed by hydrate growth into the pore bodies [Tohidi et al., 2001; Waite et al., 2004; Winters et al., 2004]. Given sufficient supply of gas, hydrates eventually fill the entire pore space [Yun et al., 2007].

The mechanical properties of an HBS sample depend on the saturation and distribution of hydrates within the pore space, e.g. on whether they are formed in the pore bodies or around the grain contacts [Ecker et al., 1998; Guerin, 2000; Tinivella & Accaino, 2000; Kleinberg et al., 2003; Winters et al., 2004; Yun et al., 2005]. For example, triaxial tests on synthetic HBS samples show an increase in sample stiffness with the hydrate saturation [Yun et al., 2007], see Figure 5.3. The authors suggest that, in the samples with high hydrate saturation, cohesion provided by hydrates which cement the sediment grains together strongly affects the sample's stiffness. Dvorkin et al. [2000] classified hydrate distributions into four types: (a) hydrates floating in the pore fluid; (b) hydrates forming part of the load-bearing granular frame; (c) hydrates coating the grains; and (d) hydrates cementing the grain contacts. Dvorkin et al. [1999] noted that small quantities of hydrates around the sediment grains further away from the contacts is not expected to

have a significant effect on the mechanical properties of HBS¹.

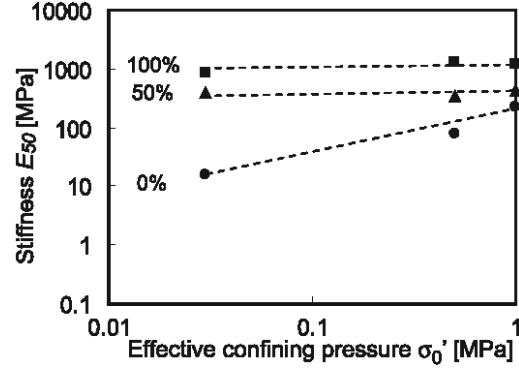


Figure 5.3: The secant modulus, E_{50} , of sand samples with different saturations of tetrahydrofuran-hydrates, evaluated from axial compression under variable confining pressures. The secant modulus, a measure of the sample’s stiffness, was determined from a stress-strain curve, as the slope of the line connecting the origin and a point which corresponds to half of the peak deviatoric stress. Adapted from Yun et al. [2007].

5.1.3 Chapter outline

We model the effect of hydrate dissociation on the mechanical properties of an HBS sample using the QuSGM model in Chapter 2. In Section 5.2, we describe a numerical HBS sample in which hydrates are load-bearing solid particles, and characterize the sample’s properties before and after partial dissociation of the hydrates. In Section 5.3, simulations of a triaxial test are performed to evaluate the mechanical properties of samples following different degrees of hydrate dissociation. Dissociation is shown to be correlated to degradation in the sample’s strength, demonstrated *via* the reduction in its elastic moduli. These results have been published in Holtzman et al. [2008b].

5.2 Micromechanical impact of hydrate dissociation

5.2.1 A numerical hydrate-bearing sediment sample

Let us consider a sample of marine sediment partially saturated with methane-hydrate, in which hydrates are load-bearing particles. The pore space is saturated with seawater. We model the sample as a dense irregular packing of ideally-smooth, spherical elastic grains, employing the QuSGM model in Chapter 2. The hydrates are represented

¹Unless these hydrates dissociate.

by the smaller grains, assigned with material properties of methane-hydrate. The number of hydrate grains is determined according to the hydrate saturation, denoted by S . We define the hydrate saturation, $S = V^h/V_{tot}$, using the convention that hydrates are a part of the pore volume [Jin et al., 2002]. In the above expression, V^h is the volume occupied by hydrates, and V_{tot} is the total pore volume (including the hydrates). Note that porosity is computed here according to the usual convention, denoted by Jin et al. [2002] as “water-filled” porosity, in which V_{tot} is the volume of the fluids only, cf. Eq. (2.19).

5.2.2 Characterization of the effect of hydrate dissociation

Hydrate dissociation weakens the host sediment [Paull et al., 2003; Sultan et al., 2004]. To model this weakening, we consider two underlying mechanisms: (a) reduction of solid fraction, as some of the hydrate grains are converted into gas and liquid water; and (b) decrease in solid support caused by the increase in pore pressure following dissociation. We quantify the dissociation through the reduction in solid fraction, from S to $S - \Delta S$, according to the saturation decrement, $\Delta S > 0$. We represent the decrease in solid fraction by shrinking the hydrate grains, reducing their radii by a uniform factor.

We are interested in the *variations* of the sample’s properties caused by dissociation, and thus consider the effect of the *change* in pressure and stress. The effect of the excess pore pressure, p_{ex} , is modeled at both the grain and the sample scale. To evaluate the immediate impact of dissociation, we neglect water flow within the sample, and assume spatially uniform pore pressure and stress. Since the contact area is much smaller than the surface area of the grains, we neglect the net force associated with the nonuniform distribution of fluid pressure on the grain’s surface, and model the effect of the excess pressure by an isotropic compression of the grains. The volume of grain i , V_i , is reduced by $\Delta V_i > 0$. For small volumetric changes, $\Delta V_i/V_i$ can be approximated as the volumetric strain of the grain, and thus determined by $p_{ex} = K_i \Delta V_i/V_i$. Here K_i is the bulk modulus of grain i .

Macroscopically, we quantify the decrease in solid support using the concepts of total and effective stress, introduced in the theory of poroelasticity [Biot, 1941; Biot & Willis, 1957]. The total stress is related to the total weight, including that of the solid and fluid phases, and, possibly, the weight of a nearby infrastructure, e.g. an oil platform. The total stress is fixed in our simulations. The effective stress is associated with the loads car-

ried by the granular frame, i.e. the sediment and hydrate grains. We compute the effective stress from the contact forces on the sample's boundaries, cf. Eq. (2.11). The reduction in effective stress due to dissociation is modeled by applying a tensile volumetric strain, $\epsilon_v < 0$, expanding the sample isotropically. For isotropic stress and strain, poroelasticity provides the following relation,

$$K\epsilon_v = \delta\sigma - \alpha_b p_{ex} \quad (5.1)$$

where $\delta\sigma$ is the increment of total stress, and α_b is the Biot-Willis coefficient [Biot & Willis, 1957]. Since the total stress is fixed, $\delta\sigma = 0$, the strain is $\epsilon_v = -\alpha_b p_{ex}/K$. This strain is applied through incremental displacements of the boundaries, see Section 2.6.1.

Finally, we quantify the impact of hydrate dissociation on the sample's mechanical properties through the change in its elastic properties. We determine the elastic moduli before and after dissociation, from simulations of uniaxial strain test, cf. Section 2.6.3.

Determination of the relation between the pore pressure and the decrement of hydrate saturation requires account of the complex kinetics of hydrate dissociation: the excess pressure varies with factors such as dissociation rate, sediment permeability, and initial pore pressure [Xu & Germanovich, 2006]. We consider several dissociation scenarios, by using a range of saturation decrements and excess pressures evaluated from the model of Xu & Germanovich [2006], as input parameters for the simulations. By varying the excess pressure and the saturation decrement independently, we produce a series of configurations, representing the different scenarios.

5.3 Simulation results

The sample used in the simulations was constructed by the procedure described in Section 2.7.2. It contains 2740 grains, of which the smallest (0.07–0.075 mm) are assigned properties of methane-hydrate, see Table 2.1. To model quartz sand as the host sediment, the other grains are assigned properties of quartz, with $\alpha_b=0.8$ [Hart & Wang, 1995]. The initial porosity and hydrate saturation prior to dissociation are $\phi \approx 36\%$ and $S \approx 0.22$. The initial isotropic effective stress is ~ 21 MPa.

A range of possible dissociation scenarios was modeled by varying the excess pressure, p_{ex} , between 0–1 MPa, and the saturation decrement, ΔS , between 0–0.015. The effective elastic moduli evaluated for each state are plotted in Figure 5.4, against: (a) the excess pressure, for a fixed saturation decrement, $\Delta S=0.01$; and (b) the saturation

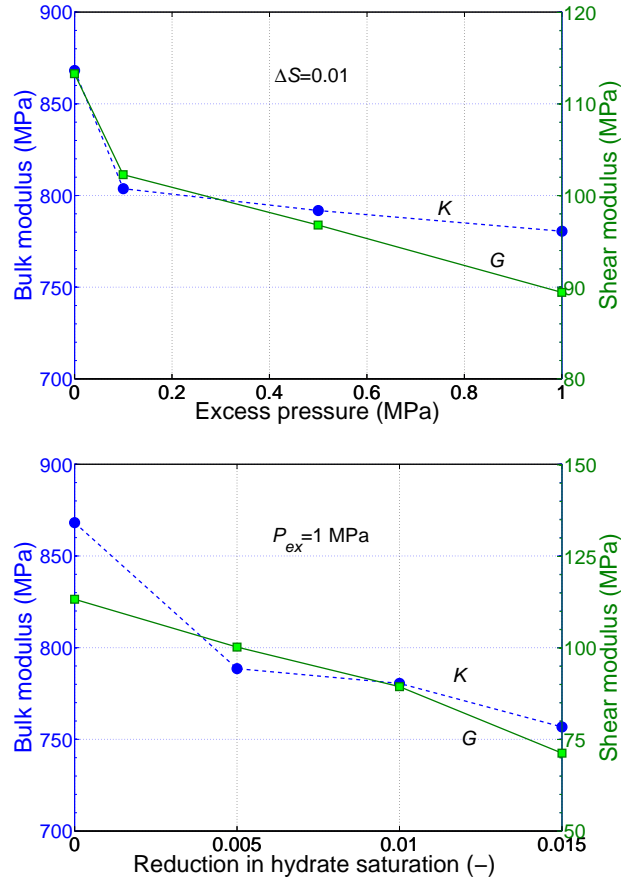


Figure 5.4: Simulations showing weakening of a hydrate-bearing sediment caused by hydrate dissociation. Weakening is demonstrated by a reduction in bulk (dashed line) and shear (solid line) modulus *vs.* hydrate dissociation. The effect of dissociation is modeled by: (a) increasing the excess pore pressure, p_{ex} , for a fixed saturation decrement, $\Delta S = 0.01$ (top plot); and (b) decreasing the saturation for a fixed excess pressure, $p_{ex} = 1 \text{ MPa}$ (bottom). The initial moduli prior to dissociation are plotted in the left-most parts of the figures, i.e. $p_{ex} = 0$ and $\Delta S = 0$.

decrement, for a fixed excess pressure, $p_{ex} = 1 \text{ MPa}$. The initial moduli prior to dissociation correspond to either $p_{ex} = 0$ or $\Delta S = 0$ in Figure 5.4. Weakening of the sediment is evident from a reduction in elastic moduli, indicating that the sample becomes looser and softer. This observation is in qualitative agreement with the published experimental data, which show the strengthening effect of hydrates on the host sediment [Durham et al., 2005; Yun et al., 2007].

5.4 Concluding remarks

We have applied our Quasi-Static Granular Model to quantify the mechanical impact of hydrate dissociation in marine sediments. Dissociation converts the solid hydrates into gas and liquid water, and is associated with an increase in pore pressure. Hydrates are modeled as load-bearing solid particles, i.e. a part of the granular frame. The reduction in solid fraction is modeled by shrinking the hydrate grains. The effect of the excess pore pressure is represented through a reduction in effective stress, by expanding the sample and compressing the grains.

A series of possible dissociation scenarios has been simulated, showing degradation in sediment strength as a reduction in the macroscopic elastic moduli. These results are in qualitative agreement with the limited available published experimental data. Further dissociation may lead to a significant decrease in the solid support, e.g. loss of shear rigidity, making the sediment susceptible to landslides and subsidence. To predict such instabilities and their impact on adjacent infrastructures, our model can provide a micromechanically-based constitutive relationship for large-scale simulations.

Chapter 6

Closure

6.1 Summary and conclusions

IN THIS DISSERTATION, we have studied the mechanics of particulate materials by a quasi-static, variational micromechanical model, implemented as a numerical simulation code. Obtaining the equilibrium configurations of grain assemblies requires a solution of a large, highly-nonlinear system of equations. In most micromechanical models, e.g. the discrete elements method, these equations are solved by explicit numerical integration in time. To enhance convergence to an oscillation-free equilibrium, a damping parameter is often introduced, and its value together with other grain-scale parameter are adjusted [Thornton, 2000; O’Sullivan et al., 2004; Potyondy & Cundall, 2004; Tavaréz, 2005; Peña et al., 2008]. In contrast, our quasi-static, variational approach can predict the mechanical properties of a sample, given its grain properties, with no adjustments of parameters.

We model the intergranular interactions through constitutive relations which are based on the contact mechanics theories of Hertz [1882], Mindlin & Deresiewicz [1953] and Deresiewicz [1954]. A three-dimensional disordered pack of spherical grains is loaded by incremental displacements of its boundaries. An equilibrium configuration is sought by minimizing the total potential energy of the pack. This minimum is computed numerically, by a modified conjugate gradient algorithm. The macroscopic stress, strain and elastic moduli are evaluated from the intergranular forces and the deformation of the pack. Our computational technique is termed Quasi-Static Granular Model (QuSGM).

Two models of cohesionless granular materials have been presented: (a) “frictionless”, neglecting intergranular tangential and torsional loads associated with frictional resistance (Chapter 2); and (b) “frictional”, accounting for intergranular friction (Chapter 3).

Our simulations confirm that the resistance of a grain pack to volumetric compaction, characterized by the bulk modulus, mainly depends on the normal contact forces [Thornton, 2000; Krut & Antony, 2007], and that the assumption of grain-scale elasticity predicts inelastic deformation of a granular pack [Goldenhirsch & Goldenberg, 2005]. While our frictionless model supports the idea that microscopic friction is not the sole mechanism of macroscopic shear resistance [Peña et al., 2008], it underestimates the shear modulus, predicting loss of shear rigidity at packing densities higher than those experimentally observed. To verify our frictional model, we simulate triaxial testing of a sample assigned grain properties from published experiments, and compare the effective elastic moduli with the experimental data. Good agreement between predicted and measured moduli, achieved with no adjustments of material parameters, demonstrates the physical soundness of our model.

By analysis of intergranular forces and displacements we show mechanisms responsible for hysteresis, strain hardening, and stress-induced anisotropy. In particular, our simulations capture rare “jump” events, in which few grains move significantly more than others, causing irreversible variations in the highly heterogeneous contact force network (“force chains”). Macroscopically, we show that these variations correspond to large fluctuations in the stress, with a significant effect on the bulk properties. These observations demonstrate the sensitivity of the bulk properties to small perturbations in the grain configurations (“emergent properties”), an intrinsic source of difficulty in predicting the behavior of particulate materials [Behringer et al., 1999]. Further difficulty is related to memory effects, at both the grain and sample scale, which require account of the loading history in characterizing a grain pack. Our observations are supported by published experimental evidence [Oda et al., 1998; Behringer et al., 1999; Ribière et al., 2005; Majmudar & Behringer, 2005; Tordesillas, 2007; Peña et al., 2008].

In Chapter 4 we apply QuSGM to study the micromechanical origins of the nonlinear deformation of weakly-cemented sediments. To model the effects of possible microscopic deformation mechanisms, we formulate several suites of constitutive relations. We propose that the following nonlinear deformation mechanisms may become important: closure and opening of microcracks, changes in the geometry of the cemented contacts, and propagation of the deformation into heterogeneous cement and grain materials. The effect of these mechanisms is modeled by varying the stiffness of each contact according to the local deformation. This stiffness is evaluated by modifying the contact theories of Hertz, Mindlin,

and Deresiewicz to account for cement. Our simulations reveal that account of nonlinear deformations at the grain-scale is required to reproduce the experimentally-observed nonlinear bulk response. In particular, a model which links the intergranular stiffness and the local deformations *via* an exponential function, is shown to match experimental data. An exponential relation is frequently used to describe crack growth, and has been justified by experiments and theory [Potyondy, 2007]. Conversely, models based on the concept of linear-elastic *cement* deformation, where the main source of nonlinearity is the *grain* deformation, i.e. Hertzian contacts, fail to reproduce the experimentally-observed nonlinearities. Our findings can be used to improve modeling of oil and water reservoirs made of poorly-consolidated sedimentary rocks.

In Chapter 5 we use QuSGM to investigate the mechanical impact of hydrate dissociation in marine sediments. Hydrates are modeled as load-bearing solid particles. The reduction in solid fraction is represented by shrinking the hydrate grains. The effect of the excess pore pressure associated with dissociation, linked to an effective stress decrement, is modeled by expanding the sample and compressing the grains. Simulations of several dissociation scenarios show degradation in sediment strength by a reduction in the macroscopic elastic moduli. These results are in qualitative agreement with published experimental data. Our model can be used to provide a micromechanically-based constitutive relationship, employed in large-scale simulations. In summary, QuSGM shows great potential for advancing the understanding of granular mechanics, and modeling complex geological systems.

6.2 Future extensions

Several issues discussed within this dissertation deserve further investigation. The following key directions can be taken to address these issues:

- (1) *Irregular grain shapes.* Computations are greatly simplified by approximating the shape of the grains by spheres. The ability of models employing spherical grains to predict the mechanical properties of packs of glass beads or sands implies that such a simplification is satisfactory for the materials made of relatively rounded grains. Nonetheless, experiments and simulations demonstrate that grain angularity can have a significant effect on the bulk response [Murphy, 1982; Robinson & Friedman, 2002;

Peña et al., 2008]. A grain of arbitrary shape can be represented through clusters of spherical grains bonded at their contacts [Jensen et al., 1999; Vu-Quoc et al., 2000], using the model in Chapter 4 to account for intergranular cohesion. The resulting contact geometry maintains the computational simplicity. Additionally, clustering allows modeling of grain damage, fracturing and comminution [Jensen et al., 2001], which are crucial in the study of faulting [Abe & Mair, 2005; Guo, 2006].

- (2) *Inelastic grain deformations.* The contact theories of Hertz, Mindlin and Deresiewicz assume linearly-elastic grain material. While we demonstrate that the *bulk* response predicted for a collection of elastic *grains* is inherently inelastic, in materials made of soft grains, or otherwise under very large stresses, inelastic grain deformation, and possibly, grain damage, may become important [Plantard & Papini, 2005]. Modeling such materials using QuSGM can be performed by modifying the constitutive rules; for example, using the elasto-plastic rules suggested in Vu-Quoc & Zhang [1999b] and Zhang & Vu-Quoc [2007].
- (3) *Description of intergranular slip.* To allow easier implementation of the model in Chapter 3, we simplify the constitutive rules by neglecting partial slip, assuming either perfect stick or sliding of each contact. The accuracy of our model can be enhanced by adopting more comprehensive constitutive relations, such as those proposed in Vu-Quoc & Zhang [1999a].
- (4) *Alteration of grain properties.* In addition to mechanically-induced damage, the grain and contact properties can be altered by processes such as chemical reactions and dissolution by pressure and heat. These processes can be modeled at the grain-scale through the constitutive equations, see, e.g., Potyondy [2007].
- (5) *Analysis of grain rotations.* Experiments and simulations show that grain rotations have significant impact on the mechanical properties of a granular pack [Oda et al., 1982]. In particular, large rotations of angular grains create large voids, increasing the sample's anisotropy, which is a necessary condition for the generation of shear bands [Oda et al., 1998]. Further analysis of simulations results, particularly with account for irregular grains, can be used to study anisotropy and shear bands.
- (6) *Enhanced applicability of our geological models.* In the two applications of QuSGM we have presented here, namely introduction of cement and gas-hydrates, we have made

several restrictive assumptions. For instance, we do not account for cement breakage. Cement breakage can be introduced by “removal” of the intergranular bonds and the corresponding loads, if these loads exceed a strength threshold [Potyondy & Cundall, 2004; Tavaréz & Plesha, 2007]. In modeling a hydrate-bearing sediment, we assumed hydrates are load-bearing particles. In some cases, hydrates can also cement the grains [Yun et al., 2005]; such sediments can be modeled by adapting the models in Chapter 4, introducing a relation between the degradation in cement properties and the dissociation.

- (7) *Large-scale computations.* Complexity of intergranular interactions restricts the number of grains that can be used in simulations. Limited pack size can have consequences on the analysis, through boundary effects [Procopio & Zavaliangos, 2005; Mesarovic & Padbidri, 2005]. The relative simplicity of the constitutive rules and the efficiency of our computational technique offer a partial remedy; using a conventional desktop for computations, the number of grains in our simulations was up to ~ 5000 . Introduction of irregular grains or inelastic grain deformations will further restrict the pack’s size. To overcome this limitation, our model can be implemented using parallel computing. Gradient algorithms, being composed of products between vectors and matrices, make implementation of a parallel version relatively straight-forward [Renouf & Alart, 2005].
- (8) *Granular dynamics.* QuSGM employs static constitutive relations, neglecting grain inertia. Such approach is applicable to describe numerous practical applications, including most conventional triaxial tests. There are, however, several situations in which dynamics becomes important, for example granular flow in low-density packings and wave propagation. To avoid the difficulties associated with numerical time-integration, the grain accelerations and velocities can be evaluated through a variational approach, retaining the quasi-static description. For instance, using two former configurations within a first-order, two-step optimization algorithm (“heavy-ball method”), see, e.g., Nesterov [1983] and the references therein.

Nomenclature

Below is a partial list of the symbols used in this dissertation. Following the definition of each variable are its physical dimensions, the equation and page number in which it was *first* introduced in the text.

Roman symbols

| | |
|-------------------|--|
| a_{ij} | Radius of contact area between grains i and j [L], Eq. (2.1), p. 28. |
| a_{ij}^{CEM} | Increment of contact radius associated with the cement [L], p. 79. |
| \hat{e}_z | Unit vector pointing opposite to the direction of gravity [dimensionless], Eq. (2.5), p. 29. |
| E | Young's modulus [$ML^{-1}T^{-2}$], p. 90. |
| E_i | Young's modulus of the material of grain i [$ML^{-1}T^{-2}$], p. 26. |
| E_{ij} | Effective elastic coefficient of the contact between grains i and j [$ML^{-1}T^{-2}$], Eq. (2.3), p. 28. |
| \bar{E}_{ij} | Young's modulus of the cement material between grains i and j [$ML^{-1}T^{-2}$], Eq. (4.20), p. 86. |
| \bar{E} | Arithmetic mean of the Young's modulus of the grains [$ML^{-1}T^{-2}$], p. 35. |
| \mathbf{f}_{ij} | Force exerted on grain i by grain j [MLT^{-2}], Eq. (2.12), p. 32. |
| \mathbf{F}_i | Sum of forces on grain i [MLT^{-2}], Eq. (2.5), p. 29. |
| \mathbf{F}_{ij} | The force applied on grain i by deformation of the cement with grain j [MLT^{-2}], Eq. (4.20), p. 86. |
| g | gravity acceleration [LT^{-2}], Eq. (2.5), p. 29. |
| G | Shear modulus [$ML^{-1}T^{-2}$], Eq. (2.15), p. 33. |
| G_i | Shear modulus of the material of grain i [$ML^{-1}T^{-2}$], p. 54. |

| | |
|----------------------|--|
| \bar{G}_{ij} | Shear modulus of the material cementing grains i and j [$\text{ML}^{-1}\text{T}^{-2}$], Eq. (4.21), p. 87. |
| \bar{G} | Arithmetic mean of the shear modulus of the grains [$\text{ML}^{-1}\text{T}^{-2}$], p. 35. |
| h_{ij} | Mutual approach between grains i and j [L], Eq. (2.1), p. 28. |
| $\hat{\mathbf{I}}$ | Second order unit tensor [dimensionless], Eq. (2.15), p. 33. |
| $k_{ij(n)}$ | Normal stiffness of the contact between grains i and j [MT^{-2}], Eq. (4.1), p. 78. |
| $k_{ij(s)}$ | Tangential stiffness of the contact between grains i and j [MT^{-2}], Eq. (3.1), p. 52. |
| $k_{ij(t)}$ | Torsional stiffness of the contact between grains i and j [ML^2T^{-2}], Eq. (3.6), p. 55. |
| K | Bulk modulus [$\text{ML}^{-1}\text{T}^{-2}$], Eq. (2.20), p. 41. |
| \bar{K} | Arithmetic mean of the bulk modulus of the grains [$\text{ML}^{-1}\text{T}^{-2}$], p. 35. |
| K_i | Bulk modulus of the material of grain i [$\text{ML}^{-1}\text{T}^{-2}$], p. 102. |
| \bar{L}_{ij} | Characteristic longitudinal extent of the cement material between grains i and j [L], Eq. (4.20), p. 86. |
| L_l | Length of the domain in direction l [L], Eq. (2.10), p. 31. |
| $L_l^{\sigma=0}$ | Length of the domain in direction l in the undeformed configuration [L], Eq. (2.10), p. 31. |
| m_i | Mass of grain i [M], Eq. (2.5), p. 29. |
| \mathbf{M}_{ij} | Torque acting on grain i in contact with grain j [ML^2T^{-2}], Eq. (3.6), p. 55. |
| $\hat{\mathbf{n}}_w$ | Inward unit normal of a planar boundary w [dimensionless], p. 27. |
| N | Number of grains in a sample [dimensionless], p. 26. |
| N_c | Number of contacts in a grain pack [dimensionless], Eq. (2.12), p. 32. |
| N_g^w | Number of grains in contact with boundary w [dimensionless], p. 32. |
| N^i | Coordination number of grain i [dimensionless], p. 29. |
| N_b^i | Number of contacts of grain i with boundaries [dimensionless], Eq. (2.5), p. 29. |
| N_g^i | Number of contacts of grain i with other grains [dimensionless], Eq. (2.5), p. 29. |
| p_{ex} | Excess pore pressure developed due to hydrate dissociation [$\text{ML}^{-1}\text{T}^{-2}$], Eq. (5.1), p. 103. |
| \mathbf{P}_{ij} | Normal force acting on grain i in contact with grain j [MLT^{-2}], Eq. (2.2), p. 28. |
| \mathbf{Q}_{ij} | Tangential force acting on grain i in contact with grain j [MLT^{-2}], Eq. (3.1), p. 52. |

| | |
|-------------------------|--|
| \mathbf{r}_i | Center coordinates of grain i [L], p. 26. |
| \mathbf{r}_{ij} | Radius-vector connecting between the centers of grains j and i [L], Eq. (2.4), p. 29. |
| r_{ij} | Distance between centers of grains i and j [L], Eq. (2.16), p. 33. |
| $\hat{\mathbf{r}}_{ij}$ | Unit vector in the direction of the centerline between grains i and j [dimensionless], Eq. (2.14), p. 32. |
| r_{ij}^* | Normal contact strain of a cemented contact between grains i and j [dimensionless], Eq. (4.11), p. 82. |
| \bar{R} | Arithmetic mean of the grain radii [L], p. 36. |
| R_i | Radius of grain i [L], p. 26. |
| R_{ij} | Effective geometric coefficient associated with the contact between grains i and j [L], Eq. (2.3), p. 28. |
| \bar{R}_{ij} | Characteristic lateral extent of the cement material between grains i and j [L], Eq. (4.20), p. 86. |
| \mathbf{R}_{ij} | Radius-vector connecting the center of grain i to the initial contact point with grain j [L], Eq. (2.18), p. 34. |
| S | Saturation of gas-hydrate in the pore space [dimensionless], p. 102. |
| \mathbf{u} | Displacement of a point [L], Eq. (2.9), p. 31. |
| \mathbf{u}_i | Displacement of the center of grain i [L], p. 26. |
| \mathbf{u}_{ij} | Relative displacement of grain i with respect to grain j [L], Eq. (3.1), p. 52. |
| $\mathbf{u}_{ij(n)}$ | Normal component of the displacement of grain i relative to grain j [L], Eq. (4.1), p. 78. |
| $\mathbf{u}_{ij(s)}$ | Tangential component of the displacement of grain i relative to grain j [L], Eq. (3.1), p. 52. |
| \mathbf{u}_w | Displacement of a boundary w [L], p. 27. |
| U_{ij} | Strain energy stored in the deformed region between grains i and j [ML ² T ⁻²], Eq. (4.25), p. 88. |
| $U_{ij(F)}$ | Strain energy associated with the deformation induced by the force \mathbf{F}_{ij} [ML ² T ⁻²], Eq. (4.25), p. 88. |
| $U_{ij(n)}$ | Strain energy associated with the deformation induced by normal compression between grains i and j [ML ² T ⁻²], Eq. (2.6), p. 30. |
| v_p | Acoustic compressional velocity [LT ⁻¹], Eq. (2.20), p. 41. |

| | |
|----------------|---|
| v_s | Acoustic shear velocity [LT^{-1}], Eq. (2.20), p. 41. |
| V_{ij}^{cap} | The volume of a spherical cap associated with sphere i overlapping with sphere j [L^3], Eq. (2.17), p. 34. |
| V^h | Volume occupied by gas-hydrates [L^3], p. 102. |
| V_i | Volume of grain i [L^3], p. 102. |
| V_{tot} | Total volume of a sample [L^3], Eq. (2.12), p. 32. |
| W_{ij} | Work done against the loads acting on grain i associated with its contact with grain j [ML^2T^{-2}], Eq. (3.14), p. 58. |
| \mathbf{x} | Radius-vector to a point [L], Eq. (2.9), p. 31. |
| \mathbf{x}_w | Coordinates of an arbitrary point on a planar boundary w [L], p. 27. |
| z^* | Reference elevation [L], Eq. (2.7), p. 30. |

Greek symbols

| | |
|--------------------|---|
| α_b | Biot-Willis coefficient [dimensionless], Eq. (5.1), p. 103. |
| γ | Exponent characterizing the stiffness evolution of a cemented contact (2) [dimensionless], Eq. (4.12), p. 82. |
| $\Delta\epsilon$ | Increment of the macroscopic strain [dimensionless], p. 45. |
| $\Delta\epsilon_a$ | Increment of the macroscopic axial strain [dimensionless], p. 67. |
| ΔS | Decrement of the saturation of gas-hydrate in the pore space [dimensionless], p. 102. |
| ΔV_i | Decrement of the volume of grain i [L^3], p. 102. |
| ϵ | Strain tensor [dimensionless], Eq. (2.9), p. 31. |
| ϵ_a | Axial strain [dimensionless], p. 86. |
| ϵ_v | Volumetric strain [dimensionless], p. 43. |
| ε | Strain factor associated with self-similar deformation [dimensionless], p. 39. |
| η | Parameter scaling the effective radius with the contact strain [dimensionless], Eq. (4.13), p. 82. |
| θ | Generalized coordinates vector [L], p. 26. |
| κ | Parameter quantifying the increase in contact area due to introduction of cement [dimensionless], p. 79. |

| | |
|--------------------|---|
| λ | Lame's coefficient [$\text{ML}^{-1}\text{T}^{-2}$], Eq. (2.15), p. 33. |
| λ^L | Parameter relating the longitudinal extent of the cement between a pair of grains to the grain sizes [dimensionless], p. 86. |
| λ^R | Parameter relating the lateral extent of the cement between a pair of grains to the grain sizes [dimensionless], p. 86. |
| μ | Coefficient of static friction [dimensionless], p. 15. |
| μ_{ij} | Coefficient of static friction between grains i and j [dimensionless], p. 51. |
| $\bar{\nu}$ | Arithmetic mean of the Poisson's ratio of the grains [dimensionless], p. 35. |
| ν_i | Poisson's ratio of the material of grain i [dimensionless], p. 26. |
| ξ_{ij} | Coordinates of a point by which the cement between grains i and j is pinned to grain i [L], Eq. (4.18), p. 85. |
| Π | Energy functional minimized to obtain the equilibrium configurations [ML^2T^{-2}], Eq. (2.7), p. 30. |
| ρ_b | Bulk density of a granular sample [M/L^3], Eq. (2.20), p. 41. |
| ρ_i | Density of the material of grain i [M/L^3], p. 26. |
| ρ_{ij} | Radius of disk of intersection between the surfaces of two overlapping spheres, i and j [L], Eq. (2.16), p. 33. |
| σ | Stress tensor [$\text{ML}^{-1}\text{T}^{-2}$], Eq. (2.11), p. 32. |
| σ_a | Axial stress [$\text{ML}^{-1}\text{T}^{-2}$], p. 86. |
| σ_c | Confining stress [$\text{ML}^{-1}\text{T}^{-2}$], p. 38. |
| σ_d | Deviatoric stress [$\text{ML}^{-1}\text{T}^{-2}$], p. 91. |
| $\sigma_c^{\mu=0}$ | Confining stress at the end of the sample generation procedure using the frictionless model [$\text{ML}^{-1}\text{T}^{-2}$], p. 37. |
| τ_{FC} | Percentile of largest forces, used in defining force chains [dimensionless], p. 45. |
| ϕ | Porosity of a sample [dimensionless], Eq. (2.19), p. 34. |
| ω | Exponent characterizing the stiffness evolution of a cemented contact (1) [dimensionless], Eq. (4.13), p. 82. |
| Ω_i | Rotation of grain i [dimensionless], p. 50. |
| $\Omega_{ij(t)}$ | Torsion of grain i relative to grain j [dimensionless], Eq. (3.6), p. 55. |

$\Omega_{ij(t)}^{tot}$ Total torsion of grain i relative to grain j , measured from the initial, undeformed configuration [dimensionless], Eq. (4.21), p. 87.

Subscripts

i A parameter associated with grain i , p. 26.

ij A parameter associated with the contact between grains i and j ; for a contact with boundary wall, j is replaced with w , p. 28.

l A parameter associated with the direction l in a cartesian coordinate system, p. 27.

mn Indices for entries of a tensor, p. 31.

(n) A parameter associated with the normal component, p. 30.

(s) A parameter associated with the tangential (shear) component, p. 52.

(t) A parameter associated with the torsional component, p. 55.

w A parameter associated with boundary w , p. 26.

Superscripts

0 Reference configuration, p. 26.

A A parameter computed analytically, p. 40.

(c) Values corresponding to the initial, undeformed configuration, p. 79.

N A parameter computed numerically, p. 40.

p A vector rotated to account for reorientation of the contact area, p. 52.

$*$ Effective property of a cemented contact, p. 78.

T Transpose (of a matrix or vector), p. 26.

Bibliography

- Abe, S. & Mair, K. (2005). Grain fracture in 3D numerical simulations of granular shear. *Geophysical Research Letters*, 32, L05305.
- Aharonov, E. & Katz, O. (2006). Landslides in vibrating sand box: what controls types of slope failure and frequency magnitude relations? *Earth and Planetary Science Letters*, 247(3–4), 280–294.
- Alonso-Marroquin, F. & Herrmann, H. J. (2002). Calculation of the incremental stress-strain relation of a polygonal packing. *Physical Review E*, 66, 021301.
- Anthony, J. L. & Marone, C. (2005). Influence of particle characteristics on granular friction. *Journal of Geophysical Research*, 110, B08409.
- Bagi, K. (1996). Stress and strain in granular assemblies. *Mechanics of Materials*, 22, 165–177.
- Bagi, K. (2003). From order to chaos: the mechanical behaviour of regular and irregular assemblies. In K. Bagi (Ed.), *QuaDPM'03 Workshop, 25–28 August 2003* (pp. 33–42). Budapest, Hungary.
- Bagi, K. (2004). Granular mechanics special issue. *International Journal of Solids and Structures*, 41(21), 5761–5762.
- Bagi, K. (2005). An algorithm to generate random dense arrangements for discrete element simulations of granular assemblies. *Granular Matter*, 7(1), 31–43.
- Bagi, K. (2006). Analysis of microstructural strain tensors for granular assemblies. *International Journal of Solids and Structures*, 43(10), 3166–3184.
- Behringer, R. P., Howell, D., Kondic, L., Tennakoon, S., & Veje, C. (1999). Predictability and granular materials. *Physica D*, 133(1–4), 1–17.
- Behringer, R. P. & Jenkins, J. T., Eds. (1997). *Powders and Grains 97*. Rotterdam, The Netherlands: Balkema.
- Berge, P. A., Bonner, B. P., & Berryman, J. G. (1995). Ultrasonic velocity-porosity relationships for sandstone analogs made from fused glass beads. *Geophysics*, 60(1), 108–119.
- Bernabè, Y., Fryer, D. T., & Hayes, J. A. (1992). The effect of cement on the strength of granular rocks. *Geophysical Research Letters*, 19(14), 1511–1514.

- Bicanic, N. (2004). Discrete element methods. In R. Stein, R. de Borst, & T. J. R. Hughes (Eds.), *Encyclopedia of Computational Mechanics*, volume 1. Wiley.
- Biot, M. A. (1941). General theory of three-dimensional consolidation. *Journal of Applied Physics*, 12(2), 155–164.
- Biot, M. A. & Willis, D. G. (1957). The elastic coefficients of the theory of consolidation. *Journal of Applied Mechanics*, 24, 594–601.
- Blair, D. L., Mueggenburg, N. W., Marshall, A. H., Jaeger, H. M., & Nagel, S. R. (2001). Force distributions in three-dimensional granular assemblies: effects of packing order and interparticle friction. *Physical Review E*, 63(4), 041304.
- Brouste, A., Renard, F., Gratier, J.-P., & Schmittbuhl, J. (2007). Variety of stylolites' morphologies and statistical characterization of the amount of heterogeneities in the rock. *Journal of Structural Geology*, 29(3), 422–434.
- Budhu, M., Ramakrishnan, S., & Frantziskonis, G. (1999). A lattice type model for particulate media. *International Journal for Numerical and Analytical Methods in Geomechanics*, 23(7), 647–671.
- Cattaneo, C. (1938). Sul contatto di due corpi elastici: distribuzione locale degli sforzi. *Rendiconti dell'Accademia Nazionale dei Lincei*, 27(6), 342–348, 434–436, 474–478.
- Chang, C. & Haimson, B. (2000). True triaxial strength and deformability of the German Continental Deep Drilling Program (KTB) deep hole amphibolite. *Journal of Geophysical Research*, 105(B8), 18999–19013.
- Chang, C. S., Chang, Y., & Kabir, M. G. (1992). Micromechanics modeling for stress-strain behavior of granular soils. I: Theory. *Journal of Geotechnical Engineering*, 118(12), 1959–1974.
- Christoffersen, J., Mehrabadi, M. M., & Nemat-Nasser, S. (1981). A micromechanical description of granular material behavior. *Journal of Applied Mechanics*, 48(2), 339–344.
- Cole, D. M. & Peters, J. F. (2007). A physically based approach to granular media mechanics: grain-scale experiments, initial results and implications to numerical modeling. *Granular Matter*, 9(5), 309–321.
- Corwin, E. I., Jaeger, H. M., & Nagel, S. R. (2005). Structural signature of jamming in granular media. *Nature*, 435, 1075–1078.
- Courant, R. & Hilbert, D. (1962). *Methods of Mathematical Physics, Vol. II: Partial Differential Equations*. New York, NY: Interscience (Wiley).
- Cui, L. & O'Sullivan, C. (2006). Exploring the macro- and micro-scale response of an idealised granular material in the direct shear apparatus. *Géotechnique*, 56(7), 455–468.

- Cundall, P. A. & Strack, O. D. L. (1979). A discrete numerical model for granular assemblies. *Géotechnique*, 29, 47–65.
- David, C., Menendez, B., & Bernabè, Y. (1998). The mechanical behaviour of synthetic sandstone with varying brittle cement content. *International Journal of Rock Mechanics and Mining Sciences*, 35(6), 759–770.
- Davie, M. K. & Buffett, B. A. (2001). A numerical model for the formation of gas hydrate below the seafloor. *Journal of Geophysical Research*, 106(B1), 497–514.
- Deresiewicz, H. (1954). Contact of elastic spheres under an oscillating torsional couple. *Journal of Applied Mechanics*, 21, 52–56.
- Deresiewicz, H. (1958a). Mechanics of granular matter. *Advances in Applied Mechanics*, 5, 233–306.
- Deresiewicz, H. (1958b). Stress-strain relations for a simple model of a granular medium. *Journal of Applied Mechanics*, 25, 402–406.
- Dewers, T. & Ortoleva, P. (1990). A coupled reaction/transport/mechanical model for intergranular pressure solution, stylolites, and differential compaction and cementation in clean sandstones. *Geochimica et Cosmochimica Acta*, 54, 1609–1625.
- Dickens, G. R. (1999). The blast in the past. *Nature*, 401, 752–755.
- Dickens, G. R. (2003). Rethinking the global carbon cycle with a large, dynamic and microbially mediated gas hydrate capacitor. *Earth and Planetary Science Letters*, 213(3–4), 169–183.
- Digby, P. J. (1981). The effective elastic moduli of porous granular rocks. *Journal of Applied Mechanics*, 48, 803–808.
- Dintwa, E., Tijskens, E., & Ramon, H. (2008). On the accuracy of the Hertz model to describe the normal contact of soft elastic spheres. *Granular Matter*, 10(3), 209–221.
- Dobry, R., Ng, T.-T., Petrakis, E., & Seridi, A. (1991). General model for contact law between two rough spheres. *Journal of Engineering Mechanics*, 117(6), 1365–1381.
- Domenico, S. N. (1977). Elastic properties of unconsolidated porous sand reservoirs. *Geophysics*, 42(7), 1339–1368.
- Duffy, J. (1959). A differential stress-strain relation for the hexagonal close-packed array of elastic spheres. *Journal of Applied Mechanics*, 26, 88–94.
- Duffy, J. & Mindlin, R. D. (1957). Stress-strain relations and vibrations of a granular medium. *Journal of Applied Mechanics*, 24, 585–593.
- Duran, J. (2000). *Sands, Powders, and Grains: An Introduction to the Physics of Granular Materials*. New York, NY: Springer.

- Durham, W. B., Stern, L. A., Kirby, S. H., & Circone, S. (2005). Rheological comparisons and structural imaging of sI and sII endmember gas hydrates and hydrate/sediment aggregates. In *Proceedings of the 5th International Conference on Gas Hydrates, 26-29 September, 2004*. Trondheim, Norway.
- Dvorkin, J., Berryman, J., & Nur, A. (1999). Elastic moduli of cemented sphere packs. *Mechanics of Materials*, 31(7), 461–469.
- Dvorkin, J., Helgerud, M. B., Waite, W. F., Kirby, S. H., & Nur, A. (2000). Introduction to physical properties and elasticity models. In M. D. Max (Ed.), *Natural Gas Hydrate in Oceanic and Permafrost Environments* (pp. 245–260). Dordrecht, The Netherlands: Kluwer.
- Dvorkin, J., Mavko, G., & Nur, A. (1991). The effect of cementation on the elastic properties of granular material. *Mechanics of Materials*, 12(3), 207–217.
- Dvorkin, J. & Nur, A. (1996). Elasticity of high-porosity sandstones: theory for two North Sea data sets. *Geophysics*, 61(5), 1363–1370.
- Dvorkin, J., Nur, A., & Yin, H. (1994). Effective properties of cemented granular materials. *Mechanics of Materials*, 18(4), 351–366.
- Ecker, C., Dvorkin, J., , & Nur, A. (1998). Sediments with gas hydrates: internal structure from seismic AVO. *Geophysics*, 63(5), 1659–1669.
- Elata, D. & Berryman, J. G. (1996). Contact force-displacement laws and the mechanical behavior of random packs of identical spheres. *Mechanics of Materials*, 24(3), 229–240.
- Elata, D. & Dvorkin, J. (1996). Pressure sensitivity of cemented granular materials. *Mechanics of Materials*, 23(2), 147–154.
- Finney, J. L. (1970). Random packings and the structure of simple liquids. I. The geometry of random close packing. *Proceedings of the Royal Society of London, Series A*, 319(1539), 479–493.
- Forsythe, G. E., Malcolm, M. A., & Moler, C. B. (1977). *Computer Methods for Mathematical Computations*. Englewood Cliffs, NJ: Prentice-Hall.
- Fu, Y. (2005). *Experimental Quantification and Dem Simulation of Micro-Macro Behaviors of Granular Materials Using X-Ray Tomography Imaging*. PhD thesis, University of Louisiana, Baton Rouge, LA.
- Garcia, X. & Medina, E. (2007). Acoustic response of cemented granular sedimentary rocks: molecular dynamics modeling. *Physical Review E*, 75(6), 061308.
- Ghaboussi, J. & Barbosa, R. (1990). Three-dimensional discrete element method for granular materials. *International Journal for Numerical and Analytical Methods in Geomechanics*, 14(7), 451–472.

- Goddard, J. D. (1990). Nonlinear elasticity and pressure-dependent wave speeds in granular media. *Proceedings of the Royal Society of London, Series A*, 430, 105–131.
- Goldenberg, C. & Goldenhirsch, I. (2005). Friction enhances elasticity in granular solids. *Nature*, 435, 188–191.
- Goldenhirsch, I. & Goldenberg, C. (2005). Stress in dense granular materials. In H. Hinrichsen & D. E. Wolf (Eds.), *The Physics of Granular Media*. Wiley–VCH.
- Gratier, J., Muquet, L., Hassani, R., & Renard, F. (2005). Experimental microstylolites in quartz and modeled application to natural stylolitic structures. *Journal of Structural Geology*, 27(1), 89–100.
- Grierson, D. S., Flater, E. E., & Carpick, R. W. (2005). Accounting for the JKR–DMT transition in adhesion and friction measurements with atomic force microscopy. *Journal of Adhesion Science and Technology*, 19(3–5), 291–311.
- Guerin, G. (2000). *Acoustic and Thermal Characterization of Oil Migration, Gas Hydrates Formation and Silica Diagenesis*. PhD thesis, Columbia University, New York, NY.
- Guo, Y. (2006). *Study of Fault Gouge Influences on Mechanical and Frictional Behavior of Granular Shear Zones Using the Distinct Element Method*. PhD thesis, Rice University, Houston, TX.
- Haff, P. K. (1997). Why prediction of grain behavior is difficult in geological granular systems. In R. P. Behringer & J. T. Jenkins (Eds.), *Powders and Grains 97*. Rotterdam, The Netherlands: Balkema.
- Haile, J. M. (1992). *Molecular Dynamics Simulation. Elementary Methods*. New York, NY: Wiley.
- Halsey, T. C. & Levine, A. J. (1998). How sandcastles fall. *Physical Review Letters*, 80(14), 3141–3144.
- Harris, J. W. & Stocker, H. (1998). *Handbook of Mathematics and Computational Science*. New York, NY: Springer–Verlag.
- Hart, D. J. & Wang, H. F. (1995). Laboratory measurements of a complete set of poroelastic moduli for Berea sandstone and Indian limestone. *Journal of Geophysical Research*, 100(B9), 17741–17751.
- Hazzard, J. F. & Mair, K. (2003). The importance of the third dimension in granular shear. *Geophysical Research Letters*, 30(13), 1708.
- Herrmann, H. J., Luding, S., & Hori, J. P., Eds. (1998). *Physics of Dry Granular Media*. Nato ASI series. Dordrecht, The Netherlands: Kluwer Academic Publishers.
- Hertz, H. (1882). Über die berührung fester elastischer körper (on the contact of elastic solids). *Journal Reine und Angewandte Mathematik*, 92, 156–171. In German.

- Heyliger, P. R. & McMeeking, R. M. (2001). Cold plastic compaction of powders by a network model. *Journal of the Mechanics and Physics of Solids*, 49(9), 2031–2054.
- Hills, D. A. (1986). The stress field induced by a twisting sphere. *Journal of Applied Mechanics*, 53, 372–378.
- Hinrichsen, H. & Wolf, D. E., Eds. (2005). *The Physics of Granular Media*. Wiley-VCH.
- Holt, R. M. (2001). Particle vs. laboratory modelling of In Situ compaction. *Physics and Chemistry of the Earth (A)*, 26(1–2), 89–93.
- Holt, R. M., Kjolaas, J., Larsen, I., Li, L., Gotusso Pillitteri, A., & Sonstebo, E. F. (2005). Comparison between controlled laboratory experiments and discrete particle simulations of the mechanical behaviour of rock. *International Journal of Rock Mechanics and Mining Sciences*, 42(7–8), 985–995.
- Holtzman, R., Silin, D. B., & Patzek, T. W. (2008a). Frictional granular mechanics: a variational approach. *International Journal for Numerical Methods in Engineering*. (Submitted).
- Holtzman, R., Silin, D. B., & Patzek, T. W. (2008b). Mechanical properties of granular materials: a variational approach to grain-scale simulations. *International Journal for Numerical and Analytical Methods in Geomechanics*. (Accepted).
- Jaeger, H. M. & Nagel, S. R. (1992). Physics of the granular state. *Science*, 255(5051), 1523–1531.
- Jaeger, H. M., Nagel, S. R., & Behringer, R. P. (1996a). Granular solids, liquids, and gases. *Reviews of Modern Physics*, 68(4), 1259–1273.
- Jaeger, H. M., Nagel, S. R., & Behringer, R. P. (1996b). The physics of granular materials. *Physics Today*, 49, 32–38.
- Jaeger, J. C. & Cook, N. G. W. (1979). *Fundamentals of Rock Mechanics*. London, UK: Chapman and Hall, third edition.
- Jenkins, J. T. & Strack, O. D. L. (1993). Mean-field inelastic behavior of random arrays of identical spheres. *Mechanics of Materials*, 16(1–2), 25–33.
- Jensen, R. P., Bosscher, P. J., Plesha, M. E., & Edil, T. B. (1999). DEM simulation of granular media-structure interface: effects of surface roughness and particle shape. *International Journal for Numerical and Analytical Methods in Geomechanics*, 23, 531–547.
- Jensen, R. P., Plesha, M. E., Edil, T. B., Bosscher, P. J., & Kahla, N. B. (2001). DEM simulation of particle damage in granular media-structure interfaces. *The International Journal of Geomechanics*, 1(1), 21–39.

- Jiang, M. J., Yu, H. S., & Harris, D. (2006). Bond rolling resistance and its effect on yielding of bonded granulates by DEM analyses. *International Journal for Numerical and Analytical Methods in Geomechanics*, 30(8), 723–761.
- Jin, G. (2006). *Physics-Based Modeling of Sedimentary Rock Formation and Prediction of Transport Properties*. PhD thesis, University of California, Berkeley, CA.
- Jin, G., Patzek, T. W., & Silin, D. B. (2003). Physics-based reconstruction of sedimentary rocks (SPE83587). In *SPE Western Regional/AAPG Pacific Section Joint Meeting, 19–24 May, 2003*. Long Beach, CA.
- Jin, Y. K., Lee, M. W., & Collett, T. S. (2002). Relationship of gas hydrate concentration to porosity and reflection amplitude in a research well, Mackenzie Delta, Canada. *Marine and Petroleum Geology*, 19(4), 407–415.
- Johnson, D. L. & Norris, A. N. (1997). Rough elastic spheres in contact: memory effects and the transverse force. *Journal of the Mechanics and Physics of Solids*, 45(6), 1025–1036.
- Johnson, D. L., Schwartz, L. M., Elata, D., Berryman, J. G., Hornby, B., & Norris, A. N. (1998). Linear and nonlinear elasticity of granular media: stress-induced anisotropy of a random sphere pack. *Journal of Applied Mechanics*, 65, 380–388.
- Johnson, K. L. (1987). *Contact Mechanics*. Cambridge, MA: Cambridge University Press.
- Katsman, R., Aharonov, E., & Scher, H. (2006). A numerical study on localized volume reduction in elastic media: some insights on the mechanics of anticracks. *Journal of Geophysical Research*, 111, B03204.
- Klaas, N. V., Marcus, K., & Kellock, C. (2005). The tribological behaviour of glass filled polytetrafluoroethylene. *Tribology International*, 38(9), 824–833.
- Kleinberg, R. L., Flaum, C., Griffin, D. D., Brewer, P. G., Malby, G. E., Pelzer, E. T., & Yesinowski, J. P. (2003). Deep sea NMR: methane hydrate growth habit in porous media and its relationship to hydraulic permeability, deposit accumulation, and submarine slope stability. *Journal of Geophysical Research*, 108(B10), 2508.
- Kozicki, J. & Teichman, J. (2005). Application of a cellular automaton to simulations of granular flow in silos. *Granular Matter*, 7(1), 45–54.
- Kranz, R. L. (1983). Microcracks in rocks: a review. *Tectonophysics*, 100(1–3), 449–480.
- Krugger-Emden, H., Simsek, E., Rickelt, S., Wirtz, S., & Scherer, V. (2007). Review and extension of normal force models for the Discrete Element Method. *Powder Technology*, 171(3), 157–173.
- Kruyt, N. P. & Antony, S. J. (2007). Force, relative-displacement, and work networks in granular materials subjected to quasistatic deformation. *Physical Review E*, 75(5), 051308.

- Kvenvolden, K. A. (1998). Potential effects of gas hydrate on human welfare. In *National Academy of Sciences colloquium: Geology, Mineralogy, and Human Welfare, 8-9 November 1998, Irvine, CA*.
- Kvenvolden, K. A., Ginsburg, G. D., & Soloviev, V. A. (1993). Worldwide distribution of subaquatic gas hydrates. *Geo-Marine Letters*, 13(1), 32–40.
- Landau, L. D. & Lifshitz, E. M. (1986). *Theory of Elasticity*. Course of Theoretical Physics, Vol 7. Burlington, MA: Elsevier.
- Li, Y., Xu, Y., & Thornton, C. (2005). A comparison of discrete element simulations and experiments for ‘sandpiles’ composed of spherical particles. *Powder Technology*, 160(3), 219–228.
- Lin, C. & Cohen, M. H. (1982). Quantitative methods for microgeometric modeling. *Journal of Applied Physics*, 53, 4152–4165.
- Lin, X. & Ng, T.-T. (1997). A three dimensional discrete element model using arrays of ellipsoids. *Géotechnique*, 47(2), 319–329.
- Liou, J.-C. & Pan, Y.-W. (2003). Fabric evolution of granular assembly under $K0$ loading/unloading. *International Journal for Numerical and Analytical Methods in Geomechanics*, 27(13), 1099–1122.
- Liu, X. & Flemings, P. B. (2006). Passing gas through the hydrate stability zone at southern Hydrate Ridge, offshore Oregon. *Earth and Planetary Science Letters*, 241(1–2), 211–226.
- Lubkin, J. L. (1951). The torsion of elastic spheres in contact. *Journal of Applied Mechanics*, 18, 183–187.
- Magnanimo, V., La Ragione, L., Jenkins, J. T., Wang, P., & Makse, H. A. (2008). Characterizing the shear and bulk moduli of an idealized granular material. *Europhysics Letters*, 81(3), 34006.
- Mair, K., Frye, K., & Marone, C. (2002). Influence of grain characteristics on the friction of granular shear zones. *Journal of Geophysical Research*, 107(B10), 2219.
- Mair, K., Marone, C., & Young, R. P. (2007). Rate dependence of acoustic emissions generated during shear of simulated fault gouge. *Bulletin of the Seismological Society of America*, 97(6), 1841–1849.
- Majmudar, T. S. & Behringer, R. P. (2005). Contact force measurements and stress-induced anisotropy in granular materials. *Nature*, 435, 1079–1082.
- Makse, H. A., Gland, N., Johnson, D. L., & Schwartz, L. (2001). The apparent failure of effective medium theory in granular materials. *Physics and Chemistry of the Earth, Part A*, 26(1–2), 107–111.

- Makse, H. A., Gland, N., Johnson, D. L., & Schwartz, L. (2004). Granular packings: nonlinear elasticity, sound propagation and collective relaxation dynamics. *Physical Review E*, 70, 061302.
- Makse, H. A., Gland, N., Johnson, D. L., & Schwartz, L. M. (1999). Why effective medium theory fails in granular materials. *Physical Review Letters*, 83(24), 5070–5073.
- Makse, H. A., Johnson, D. L., & Schwartz, L. (2000). Packing of compressible granular materials. *Physical Review Letters*, 84(18), 4160–4163.
- Martin, C. D. & Chandler, N. A. (1994). The progressive fracture of Lac du Bonnet granite. *International Journal of Rock Mechanics and Mining Sciences and Geomechanics Abstracts*, 31(6), 643–659.
- Martin, C. L., Bouvard, D., & Shima, S. (2003). Study of particle rearrangement during powder compaction by the Discrete Element Method. *Journal of the Mechanics and Physics of Solids*, 51(4), 667–693.
- Mehrabadi, M. M., Nemat-Nasser, S., Shodja, H. M., & Subhash, G. (1988). Some basic theoretical and experimental results on micromechanics of granular flow. In M. Satake & J. T. Jenkins (Eds.), *Micromechanics of Granular Materials* (pp. 253–262). Amsterdam: Elsevier.
- Mesarovic, S. D. & Padbidri, J. (2005). Minimal kinematic boundary conditions for simulations of disordered microstructures. *Philosophical Magazine*, 85(1), 65–78.
- Mindlin, R. D. (1949). Compliance of elastic bodies in contact. *Journal of Applied Mechanics*, 16, 259–268.
- Mindlin, R. D. & Deresiewicz, H. (1953). Elastic spheres in contact under varying oblique forces. *Journal of Applied Mechanics*, 20, 327–344.
- Munjiza, A., Owen, D. R. J., & Bicanic, N. (1995). A combined finite-discrete element method in transient dynamics of fracturing solids. *Engineering Computations*, 12(2), 145–174.
- Murphy, W. F. (1982). *Effects of Microstructure and Pore Fluids on the Acoustic Properties of Granular Sedimentary Materials*. PhD thesis, Stanford University, Stanford, CA.
- Muthuswamy, M. & Tordesillas, A. (2006). How do interparticle contact friction, packing density and degree of polydispersity affect force propagation in particulate assemblies? *Journal of Statistical Mechanics: Theory and Experiment*, 2006(09), P09003.
- Nakagawa, S. (2008). Acoustic experiments on synthetic and natural weakly cemented sands. Unpublished data.
- Nakagawa, S. & Myer, L. Y. (2001). *Mechanical and Acoustic Properties of Weakly Cemented Granular Rocks*. Technical Report LBNL-50814, Lawrence Berkeley National Laboratory, Berkeley, CA.

- Nesterov, Y. E. (1983). A method of solving the convex programming problem with convergence rate $O(1/k^2)$. *Doklady Akademii Nauk SSSR*, 269(3), 543–547.
- Ng, T. T. & Wang, C. (2001). Comparison of a 3-D DEM simulation with MRI data. *International Journal for Numerical and Analytical Methods in Geomechanics*, 25(5), 497–507.
- Norris, A. N. & Johnson, D. L. (1997). Nonlinear elasticity of granular media. *Journal of Applied Mechanics*, 64, 39–49.
- O’Hern, C. S., Silbert, L. E., Liu, A. J., & Nagel, S. R. (2003). Jamming at zero temperature and zero applied stress: the epitome of disorder. *Physical Review E*, 68(1), 011306.
- Oda, M., Kazama, H., & Konishi, J. (1998). Effects of induced anisotropy on the development of shear bands in granular materials. *Mechanics of Materials*, 28(1–4), 103–111.
- Oda, M., Konishi, J., & Nemat-Nasser, S. (1982). Experimental micromechanical evaluation of strength of granular materials: effects of particle rolling. *Mechanics of Materials*, 1(4), 269–283.
- O’Sullivan, C. (2002). *The Application of Discrete Element Modelling to Finite Deformation Problems in Geomechanics*. PhD thesis, University of California, Berkeley, CA.
- O’Sullivan, C. & Bray, J. D. (2004). Selecting a suitable time-step for discrete element simulations that use the central difference time integration approach. *Engineering Computations*, 21(2–4), 278–303.
- O’Sullivan, C., Bray, J. D., & Riemer, M. (2004). Examination of the response of regularly packed specimens of spherical particles using physical tests and discrete element simulations. *Journal of Engineering Mechanics*, 130(10), 1140–1150.
- Paull, C. K., Brewer, P. G., Ussler, W., Peltzer, E. T., Rehder, G., & Clague, D. (2003). An experiment demonstrating that marine slumping is a mechanism to transfer methane from seafloor gas-hydrate deposits into the upper ocean and atmosphere. *Geo-Marine Letters*, 22(4), 198–203.
- Peña, A. A., Lizcano, A., Alonso-Marroquin, F., & Herrmann, H. J. (2008). Biaxial test simulations using a packing of polygonal particles. *International Journal for Numerical and Analytical Methods in Geomechanics*, 32(2), 143–160.
- Peters, J. F., Muthuswamy, M., Wibowo, J., & Tordesillas, A. (2005). Characterization of force chains in granular material. *Physical Review E*, 72(4), 041307.
- Plantard, G. & Papini, M. (2005). Mechanical and electrical behaviors of polymer particles. Experimental study of the contact area between two particles. Experimental validation of a numerical model. *Granular Matter*, 7(1), 1–12.
- Pohlman, N. A., Severson, B. L., Ottino, J. M., & Lueptow, R. M. (2006). Surface roughness effects in granular matter: influence on angle of repose and the absence of segregation. *Physical Review E*, 73(3), 031304.

- Potyondy, D. O. (2007). Simulating stress corrosion with a bonded-particle model for rock. *International Journal of Rock Mechanics and Mining Sciences*, 44(5), 677–691.
- Potyondy, D. O. & Cundall, P. A. (2004). A bonded-particle model for rock. *International Journal of Rock Mechanics and Mining Sciences*, 41(8), 1329–1364.
- Press, W. H., Flannery, B. P., Teukolsky, S. A., & Vetterling, W. T. (1986). *Numerical Recipes in Fortran 77*. New York: Cambridge University Press.
- Pride, S. R. (2005). Relationships between seismic and hydrological properties. In Y. Rubin & S. Hubbard (Eds.), *Hydrogeophysics*. Dordrecht, The Netherlands: Springer.
- Procopio, A. T. & Zavaliangos, A. (2005). Simulation of multi-axial compaction of granular media from loose to high relative densities. *Journal of the Mechanics and Physics of Solids*, 53(7), 1523–1551.
- Radjaï, F., Jean, M., Moreau, J. J., & Roux, S. (1996). Force distributions in dense two-dimensional granular systems. *Physical Review Letters*, 77(2), 274–277.
- Rees, D. (2006). *Basic Engineering Plasticity: An Introduction with Engineering and Manufacturing Applications*. United Kingdom: Butterworth–Heinemann.
- Renard, F., Gratier, J.-P., & Jamtveit, B. (2000). Kinetics of crack-sealing, intergranular pressure solution, and compaction around active faults. *Journal of Structural Geology*, 22(10), 1395–1407.
- Renouf, M. & Alart, P. (2005). Conjugate gradient type algorithms for frictional multi-contact problems: applications to granular materials. *Computer Methods in Applied Mechanics and Engineering*, 194, 2019–2041.
- Ribière, P., Richard, P., Delannay, R., Bideau, D., Toiya, M., & Losert, W. (2005). Effect of rare events on out-of-equilibrium relaxation. *Physical Review Letters*, 95(26), 268001.
- Robinson, D. A. & Friedman, S. P. (2002). Observations of the effects of particle shape and particle size distribution on avalanching of granular media. *Physica A*, 311(1–2), 97–110.
- Rothenburg, L. & Bathurst, R. J. (1989). Analytical study of induced anisotropy in idealized granular-materials. *Géotechnique*, 39(4), 601–614.
- Rothenburg, L. & Bathurst, R. J. (1991). Numerical simulation of idealized granular assemblies with plane elliptical particles. *Computers and Geotechnics*, 11(4), 315–329.
- Ruppel, C. (2007). Tapping methane hydrates for unconventional natural gas. *Elements*, 3(3), 193–199.
- Rutqvist, J. & Moridis, G. J. (2007). Numerical studies of geomechanical stability of hydrate-bearing sediments. In *2007 Offshore Technology Conference, 30 April - 3 May* Houston, TX.

- Saidi, F., Bernabè, Y., & Reuschlè, T. (2003). The mechanical behaviour of synthetic, poorly consolidated granular rock under uniaxial compression. *Tectonophysics*, 370(1–4), 105–120.
- Saidi, F., Bernabè, Y., & Reuschlè, T. (2005). Uniaxial compression of synthetic, poorly consolidated granular rock with a bimodal grain-size distribution. *Rock Mechanics and Rock Engineering*, 38(2), 129–144.
- Segalman, D. J., Starr, M. J., & Heinsteins, M. W. (2005). New approximations for elastic spheres under an oscillating torsional couple. *Journal of Applied Mechanics*, 72(5), 705–710.
- Shi, G.-H. (1988). *Discontinuous Deformation Analysis: A New Numerical Model for the Statics and Dynamics of Block Systems*. PhD thesis, University of California, Berkeley, CA.
- Shimizu, Y. (2002). Three-dimensional DEM simulation of conveying granular materials by horizontal screw. In B. K. Cook & R. P. Jensen (Eds.), *Discrete Element Methods: Numerical Modeling of Discontinua (GSP 117), Proceedings of the Third International Conference on Discrete Element Methods, September 23–25, 2002*, volume 259 (pp. 415–422). Santa Fe, New Mexico: ASCE.
- Sienkiewicz, F., Shukla, A., Sadd, M., Zhang, Z., & Dvorkin, J. (1996). A combined experimental and numerical scheme for the determination of contact loads between cemented particles. *Mechanics of Materials*, 22(1), 43–50.
- Sloan, E. D. (1998). *Clathrate Hydrates of Natural Gases*. New York: Marcel Dekker.
- Sloan, E. D. (2003). Fundamental principles and applications of natural gas hydrates. *Nature*, 426, 353–363.
- Sultan, N., Cochonat, P., Foucher, J.-P., & Mienert, J. (2004). Effect of gas hydrates melting on seafloor slope instability. *Marine Geology*, 213(1–4), 379–401.
- Taboada, A., Estrada, N., & Radjaï, F. (2006). Additive decomposition of shear strength in cohesive granular media from grain-scale interactions. *Physical Review Letters*, 97(9), 098302.
- Tada, R. & Siever, R. (1989). Pressure solution during diagenesis. *Annual Review of Earth and Planetary Sciences*, 17(1), 89–118.
- Tavarez, F. A. (2005). *Discrete Element Method for Modelling Solid and Particulate Materials*. PhD thesis, University of Wisconsin, Madison, WI.
- Tavarez, F. A. & Plesha, M. E. (2007). Discrete element method for modelling solid and particulate materials. *International Journal for Numerical Methods in Engineering*, 70, 379–404.

- Tejchman, J. & Wu, W. (1995). Experimental and numerical study of sand-steel interfaces. *International Journal for Numerical and Analytical Methods in Geomechanics*, 19(8), 513–536.
- The MathWorks Inc. (2008). *MATLAB, The Language of Technical Computing, Version 7.6.0.324 (R2008a)*.
- Thomas, P. A. (1997). *Discontinuous Deformation Analysis of Particulate Media*. PhD thesis, University of California, Berkeley, CA.
- Thomas, P. A. & Bray, J. D. (1999). Capturing nonspherical shape of granular media with disk clusters. *Journal of Geotechnical and Geoenvironmental Engineering*, 125(3), 169–178.
- Thornton, C. (2000). Numerical simulations of deviatoric shear deformation of granular media. *Géotechnique*, 50(1), 43–53.
- Thornton, C. & Antony, S. J. (1998). Quasi-static deformation of particulate media. *Philosophical Transactions of the Royal Society A: Mathematical, Physical and Engineering Sciences*, 356(1747), 2763–2782.
- Thurston, C. W. & Deresiewicz, H. (1959). Analysis of a compression test of a model of a granular medium. *Journal of Applied Mechanics*, 26, 251–258.
- Timoshenko, S. P. & Goodier, J. N. (1970). *Theory of Elasticity*. Engineering societies monographs. New York: McGraw-Hill.
- Tinivella, U. & Accaino, F. (2000). Compressional velocity structure and Poisson’s ratio in marine sediments with gas hydrate and free gas by inversion of reflected and refracted seismic data (South Shetland Islands, Antarctica). *Marine Geology*, 164(1), 13–27.
- Tohidi, B., Anderson, R., Clennell, M. B., Burgass, R. W., & Biderkab, A. B. (2001). Visual observation of gas-hydrate formation and dissociation in synthetic porous media by means of glass micromodels. *Geology*, 29(9), 867–870.
- Tomutsa, L. & Silin, D. (2004). *Nanoscale Pore Imaging and Pore Scale Fluid Flow Modeling in Chalk*. Technical Report LBNL-56266, Lawrence Berkeley National Laboratory, Berkeley, CA.
- Tordesillas, A. (2007). Force chain buckling, unjamming transitions and shear banding in dense granular assemblies. *Philosophical Magazine*, 87(32), 4987–5016.
- Vaisnys, J. R. & Pilbeam, C. C. (1975). Mechanical properties of granular media. *Annual Review of Earth and Planetary Sciences*, 3(1), 343–360.
- Visser, J. (1989). Van der Waals and other cohesive forces affecting powder fluidization. *Powder Technology*, 58(1), 1–10.

- Vu-Quoc, L. & Zhang, X. (1999a). An accurate and efficient tangential force-displacement model for elastic frictional contact in particle-flow simulations. *Mechanics of Materials*, 31(4), 235–269.
- Vu-Quoc, L. & Zhang, X. (1999b). An elastoplastic contact force-displacement model in the normal direction: displacement-driven version. *Proceedings of the Royal Society of London, Series A*, 455(1991), 4013–4044.
- Vu-Quoc, L. & Zhang, X. (2001). Normal and tangential force-displacement relations for frictional elasto-plastic contact of spheres. *International Journal of Solids and Structures*, 38(36–37), 6455–6489.
- Vu-Quoc, L., Zhang, X., & Walton, O. R. (2000). A 3-D discrete-element method for dry granular flows of ellipsoidal particles. *Computer Methods in Applied Mechanics and Engineering*, 187(3–4), 483–528.
- Waite, W. F., Winters, W. J., & H., M. D. (2004). Methane hydrate formation in partially water-saturated ottawa sand. *American Mineralogist*, 89, 1202–1207.
- Walsh, S. D. C., Tordesillas, A., & Peters, J. F. (2007). Development of micromechanical models for granular media. *Granular Matter*, 9(5), 337–352.
- Walton, K. (1978). The oblique compression of two elastic spheres. *Journal of the Mechanics and Physics of Solids*, 26, 139–150.
- Walton, K. (1987). The effective elastic moduli of a random packing of spheres. *Journal of the Mechanics and Physics of Solids*, 35, 213–226.
- Walton, O. R. (1993). Numerical simulation of inclined chute flows of monodisperse, inelastic, frictional spheres. *Mechanics of Materials*, 16(1–2), 239–247.
- Walton, O. R. & Braun, R. L. (1986). Viscosity, granular-temperature, and stress calculations for shearing assemblies of inelastic, frictional disks. *Journal of Rheology*, 30(5), 949–980.
- Williams, J. R. & O'Connor, R. (1995). A linear complexity intersection algorithm for discrete element simulation of arbitrary geometries. *Engineering Computations*, 12(2), 185–208.
- Winters, W. J., Pecher, I. A., Waite, W. F., & Mason, D. H. (2004). Physical properties and rock physics models of sediment containing natural and laboratory-formed methane gas hydrate. *American Mineralogist*, 89(8-9), 1221–1227.
- Xu, W. & Germanovich, L. N. (2006). Excess pore pressure resulting from methane hydrate dissociation in marine sediments: a theoretical approach. *Journal of Geophysical Research*, 111, B01104.
- Yin, H. (1993). *Acoustic Velocity and Attenuation of Rocks: Isotropy, Intrinsic Anisotropy, and Stress-Induced Anisotropy*. PhD thesis, Stanford University, Stanford, CA.

- Yin, H. & Dvorkin, J. (1994). Strength of cementated grains. *Geophysical Research Letters*, 21(10), 903–906.
- Yong, R. N. & Warkentin, B. P. (1975). *Soil properties and behaviour*. Developments in geotechnical engineering. Amsterdam; The Netherlands: Elsevier.
- Yun, T. S., Francisca, F. M., Santamarina, J. C., & Ruppel, C. (2005). Compressional and shear wave velocities in uncemented sediment containing gas hydrate. *Geophysical Research Letters*, 32, L10609.
- Yun, T. S., Santamarina, J. C., & Ruppel, C. (2007). Mechanical properties of sand, silt, and clay containing tetrahydrofuran hydrate. *Journal of Geophysical Research*, 112, B04106.
- Zang, A. & Wong, T.-F. (1995). Elastic stiffness and stress concentration in cemented granular material. *International Journal of Rock Mechanics and Mining Science & Geomechanics Abstracts*, 32(6), 563–574.
- Zhang, H. P. & Makse, H. A. (2005). Jamming transition in emulsions and granular materials. *Physical Review E*, 72(1), 011301.
- Zhang, X. & Vu-Quoc, L. (2007). An accurate elasto-plastic frictional tangential force-displacement model for granular-flow simulations: displacement-driven formulation. *Journal of Computational Physics*, 225, 730–752.
- Zhu, H., Chang, C. S., & Rish, J. W. (1996a). Normal and tangential compliance for conforming binder contact I: elastic binder. *International Journal of Solids and Structures*, 33(29), 4337–4349.
- Zhu, H., Chang, C. S., & Rish, J. W. (1996b). Normal and tangential compliance for conforming binder contact II: visco-elastic binder. *International Journal of Solids and Structures*, 33(29), 4351–4363.

Appendix A

Numerical algorithm

THIS APPENDIX outlines the numerical algorithm used in the simulations. Following application of each load increment at a given (reference) configuration, simulated through displacements of the pack's boundaries, a modified conjugate gradient (CG) algorithm is employed to find a new (current) equilibrium configuration of the grains. We begin with a brief description of CG for minimization of a quadratic criterion, followed by a presentation of the modified algorithm implemented in our computations. A detailed description of CG method appears in Press et al. [1986]. The difficulties associated with implementing CG in granular mechanics are discussed in Renouf & Alart [2005].

A.1 Conjugate gradient: minimizing a quadratic criterion

The conjugate gradient (CG) method was designed for the minimization of a quadratic criterion,

$$J(\mathbf{x}) = \frac{1}{2} \mathbf{A} \mathbf{x} \cdot \mathbf{x} - \mathbf{b} \cdot \mathbf{x} \quad (\text{A.1})$$

where \mathbf{b} is a known column-vector of dimension N , \mathbf{A} is a symmetric, positive-definite $N \times N$ matrix, and \mathbf{x} is a column-vector of N unknowns. The gradient of $J(\mathbf{x})$ is

$$\nabla_{\mathbf{x}} J|_{\mathbf{x}} = \mathbf{A} \mathbf{x} - \mathbf{b} \quad (\text{A.2})$$

The value of \mathbf{x} that corresponds to a minimum of the function in Eq. (A.1), $\mathbf{x} = \mathbf{x}^*$, is the solution to the following system of linear equations: $\mathbf{A} \mathbf{x} = \mathbf{b}$.

Conjugate gradient is an iterative procedure: starting from an initial guess $\mathbf{x}^{k=0}$, at each iteration, k , the variables are updated from \mathbf{x}^k to \mathbf{x}^{k+1} by

$$\mathbf{x}^{k+1} = \mathbf{x}^k - \alpha^k \mathbf{p}^k \quad (\text{A.3})$$

The step size coefficient α^k is selected to minimize $J(\mathbf{x}^k - \alpha^k \mathbf{p}^k)$ for a given \mathbf{x}^k and \mathbf{p}^k . At the minimum,

$$\begin{aligned} \left. \frac{d}{d\alpha} J(\mathbf{x}^k - \alpha \mathbf{p}^k) \right|_{\alpha=\alpha^k} &= (\mathbf{A}(\mathbf{x}^k - \alpha^k \mathbf{p}^k) - \mathbf{b}) \cdot \mathbf{p}^k \\ &= (\mathbf{A}\mathbf{x}^{k+1} - \mathbf{b}) \cdot \mathbf{p}^k = 0 \end{aligned} \quad (\text{A.4})$$

Therefore,

$$\alpha^k = \frac{\mathbf{r}^k \cdot \mathbf{p}^k}{\mathbf{A}\mathbf{p}^k \cdot \mathbf{p}^k} \quad (\text{A.5})$$

where

$$\mathbf{r}^k = \mathbf{A}\mathbf{x}^k - \mathbf{b} \quad (\text{A.6})$$

is the so-called residual vector.

The search direction vector \mathbf{p} indicates the directions of the update. In the steepest descent (SD) method, the update is done in a direction which opposes that of the gradient, i.e. $\mathbf{p}^k = \mathbf{r}^k$ [Press et al., 1986]. While within a specific iteration, updating in the anti-gradient direction provides the largest possible decrease of the functional [Courant & Hilbert, 1962], these directions may be repeated after several iterations. In CG, the efficiency of the algorithm is improved by avoiding such repetition, computing the search directions by

$$\mathbf{p}^k = \mathbf{r}^k - \beta^k \mathbf{p}^{k-1} \quad (\text{A.7})$$

where β^k is selected to provide for

$$\mathbf{A}\mathbf{p}^k \cdot \mathbf{p}^{k-1} = 0 \quad (\text{A.8})$$

The latter quality is denoted as ‘‘A-conjugacy’’: the search directions \mathbf{p}^k are orthogonal to all former directions (0,1,...,k-1). For any two iterations, k and m , the following conditions hold true:

$$\mathbf{A}\mathbf{p}^k \cdot \mathbf{p}^m = 0, \quad k \neq m \quad (\text{A.9a})$$

$$\mathbf{r}^k \cdot \mathbf{r}^m = 0, \quad k \neq m \quad (\text{A.9b})$$

$$\mathbf{r}^k \cdot \mathbf{p}^m = 0, \quad k > m \quad (\text{A.9c})$$

With some algebra, it can be shown that β can be evaluated at each iteration by

$$\beta^k = \frac{(\nabla_{\mathbf{x}} J|_{\mathbf{x}^k} - \nabla_{\mathbf{x}} J|_{\mathbf{x}^{k-1}}) \cdot \nabla_{\mathbf{x}} J|_{\mathbf{x}^k}}{(\nabla_{\mathbf{x}} J|_{\mathbf{x}^k} - \nabla_{\mathbf{x}} J|_{\mathbf{x}^{k-1}}) \cdot \mathbf{p}^{k-1}} = -\frac{\|\nabla_{\mathbf{x}} J|_{\mathbf{x}^k}\|^2}{\|\nabla_{\mathbf{x}} J|_{\mathbf{x}^{k-1}}\|^2} \quad (\text{A.10})$$

The iterations begin by selecting the initial guess, \mathbf{x}^0 , with the gradient as the initial search direction, $\mathbf{p}^0 = \mathbf{r}^0$, and $\beta^0 = 0$. Selecting an initial guess which is closer to the solution can reduce the number of iterations required for convergence [Press et al., 1986]. Convergence is monitored using two criteria: (1) the relative reduction of the functional, namely the ability of the numerical algorithm to improve the solution; and (2) the magnitude of the squared norm of the functional's gradient, which vanishes as $\mathbf{x}^k \rightarrow \mathbf{x}^*$. The algorithm is summarized in Figure A.1.

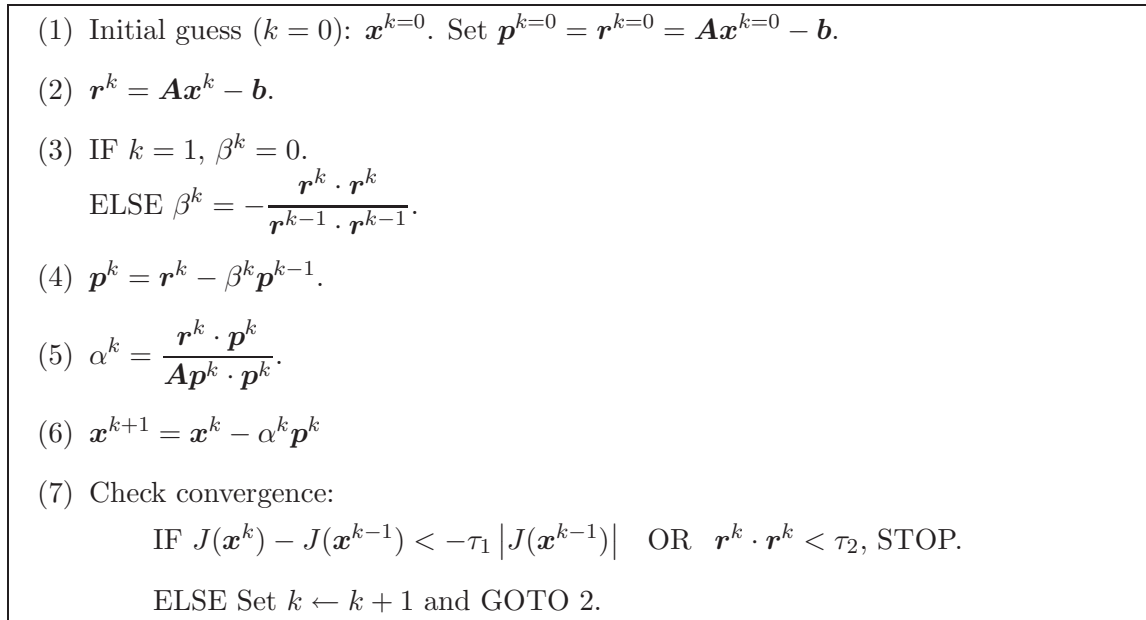


Figure A.1: Conjugate gradient algorithm for the minimization of a quadratic criterion.

A.2 Modified algorithm implemented in granular mechanics

A.2.1 Conjugate gradient for minimization of a non-quadratic criterion

An equilibrium configuration of a grain pack satisfies a system of force and moment balance equations. To find this configuration, we seek for the generalized coordinates, $\boldsymbol{\theta}$, that provide a local minimum of an energy functional, Π . Thus, $\boldsymbol{\theta}$ becomes the vector of unknowns, \mathbf{x} , and $\Pi(\boldsymbol{\theta})$ replaces the quadratic functional $J(\mathbf{x})$ in Eq. (A.1). The functional's gradient, $\nabla_{\boldsymbol{\theta}}\Pi$, computed from the sum of forces and moments on each grain ("generalized forces"), replaces $\nabla_{\mathbf{x}}J = \mathbf{r}(\mathbf{x})$. We note that the frictionless model presented in Chapter 2 does not account for rotations and moments, reducing the size of $\boldsymbol{\theta}$ and $\nabla_{\boldsymbol{\theta}}\Pi$.

We use the principle of minimum potential energy [Timoshenko & Goodier, 1970], and compute Π from the work done against the intergranular loads. Thus, the functional Π is not quadratic, for the following reasons: (a) nonlinearity of the constitutive relations, associated with changes in the contact area with the normal compression, cf. Eq. (2.1)–(2.2), and in the tangential and torsional stiffness (stick-slip); and (b) variations in the contact network. Minimization of a non-quadratic functional requires modification of the algorithm presented in Section A.1. The modified algorithm employed in our simulations (Except in Chapter 4) is presented in Sections A.2.1.1–A.2.1.3. The algorithm used in Chapter 4 is given in Section A.2.2.

- (1) Initial guess ($k = 0$): $\boldsymbol{\theta}^{k=0} = \mathbf{0}$. Set $\mathbf{p}^{k=0} = \nabla_{\boldsymbol{\theta}} \Pi|_{\boldsymbol{\theta}^{k=0}}$.
- (2) IF k divisible by k_{inc} AND $\mathbf{u}_w^k < \mathbf{u}_w$, apply incremental perturbation:
 - (a) Update boundary conditions: $\mathbf{x}_w^k \leftarrow \mathbf{x}_w^k + \Delta \mathbf{u}_w^k$ and $\mathbf{u}_w^k \leftarrow \mathbf{u}_w^k + \Delta \mathbf{u}_w^k$
 - (b) Update the grain displacements (“initial guess”): $\mathbf{u}_i^k \leftarrow \mathbf{u}_i^k + \Delta \mathbf{u}_i^k$, cf. Eq. (A.11), and $\mathbf{r}_i^k \leftarrow \mathbf{r}_i^k + \Delta \mathbf{u}_i^k$.
- (3) Evaluate $\nabla_{\boldsymbol{\theta}} \Pi|_{\boldsymbol{\theta}^k}$.
- (4) IF $k = 1$ OR k divisible by k_{SD} , refresh with an SD step, by setting $\beta^k = 0$.
 ELSE $\beta^k = - \left(\frac{\|\nabla_{\boldsymbol{\theta}} \Pi|_{\boldsymbol{\theta}^k}\|}{\|\nabla_{\boldsymbol{\theta}} \Pi|_{\boldsymbol{\theta}^{k-1}}\|} \right)^2$.
- (5) $\mathbf{p}^k = \nabla_{\boldsymbol{\theta}} \Pi|_{\boldsymbol{\theta}^k} - \beta^k \mathbf{p}^{k-1}$.
- (6) Given $\boldsymbol{\theta}^k$ and \mathbf{p}^k , find α^k that minimizes $\Pi(\boldsymbol{\theta}^k - \alpha^k \mathbf{p}^k)$, cf. Section A.2.1.2.
- (7) Update the generalized coordinates, $\boldsymbol{\theta}^{k+1} = \boldsymbol{\theta}^k - \alpha^k \mathbf{p}^k$, and the grain positions, $\mathbf{r}_i^{k+1} = \mathbf{r}_i^k + \mathbf{u}_i^k$.
- (8) Check convergence:
 IF $\Pi(\mathbf{x}^{k-1}) - \Pi(\mathbf{x}^k) < \tau_1 |\Pi(\mathbf{x}^{k-1})|$ OR $\|\nabla_{\boldsymbol{\theta}} \Pi|_{\boldsymbol{\theta}^k}\|^2 < \tau_2 N (\bar{E} \bar{R}^2)^2$ OR $k > k_{max}$,
 STOP.
 ELSE Set $k \leftarrow k + 1$ and GOTO Step 2.

Figure A.2: A numerical algorithm used in simulating application of a load increment and obtaining an equilibrium configuration. The conjugate gradient algorithm was modified to accommodate the nonlinearity of the balance equations.

A.2.1.1 Initial guess following application of a load increment

We choose as the initial guess $\boldsymbol{\theta}^{k=0} = \mathbf{0}$, i.e. the reference configuration. We use a fixed cartesian coordinate system with its origin at the pack's geometric center, \mathbf{x}_{CM} , aligned with the pack's boundaries. Application of each load increment is modeled by symmetric displacements of each pair of parallel boundaries, $\mathbf{u}_{w=l} = -\mathbf{u}_{w=l+3}$, where $l = 1, 2, 3$ denotes the coordinate directions, see Figure 2.2. Note that we apply normal strains only, thus each boundary is displaced in the direction of its normal. Within the iterations, these displacements are applied in several sub-increments, every k_{inc} iterations¹, see Figure A.2. To enhance convergence, following application of each incremental boundary displacement, we select an “initial guess” by which the grain displacements and positions are updated. For each direction, the update for grain i is computed from the displacement of the boundaries, scaled by the ratio between the distance of the grain to the pack's center and the side length. Denoting the incremental displacement of a boundary in the l direction by $\Delta \mathbf{u}_l^k$, this update is computed by

$$\Delta \mathbf{u}_{i(l)}^k = \frac{(\mathbf{x}_{CM} - \mathbf{r}_i^k) \cdot \hat{\mathbf{e}}_l}{2L_l^k} \Delta \mathbf{u}_l^k \quad (\text{A.11})$$

where L_l and $\hat{\mathbf{e}}_l$ are the length of the pack and a unit vector in the l direction, respectively. The displacement and center coordinates of grain i , \mathbf{u}_i^k and \mathbf{r}_i^k , are updated by adding the increment $\Delta \mathbf{u}_i^k = \sum_{l=1}^3 \Delta \mathbf{u}_{i(l)}^k$, see Figure A.2. The incremental displacements, $\Delta \mathbf{u}_l^k$, are applied until the total desired boundary displacement, $\mathbf{u}_{w=l}$, has been achieved.

A.2.1.2 Finding an optimal update coefficient

The nonlinearity of the balance equations implies that the update coefficient, α , should not be evaluated by Eq. (A.5). Here, α is found numerically, by minimizing $\Pi(\boldsymbol{\theta}^k - \alpha^k \nabla_{\boldsymbol{\theta}} \Pi|_{\boldsymbol{\theta}^k})$ with respect to α^k . We perform this minimization iteratively, using an algorithm which combines the golden section search and parabolic interpolation methods² [Forsythe et al., 1977; Press et al., 1986]. To avoid non-physical deformation path such as grain permutations³, we restrict the update of the grain displacements within each iteration by limiting the value of α : the maximum grain displacement within a single iteration does

¹The number of iterations between application of each incremental displacement, k_{inc} , that provided the smallest number of iterations until convergence, was found by trial and error.

²The function *fminbnd* in MATLAB software [The MathWorks Inc., 2008] was employed in our code.

³A numerical artifact which corresponds to a non-local minimum of Π .

not exceed 10^{-3} – 10^{-1} of its radius. The optimal constraint value varies with the packing density and microstructure, among other factors, and is determined by trial and error.

A.2.1.3 Convergence criteria

The CG method yields an exact solution to a system of linear equations with symmetric, positive-definite matrix, within a number of iterations which does not exceed the dimensions of the matrix, N [Press et al., 1986]. Here, the nonlinearity of the equations together with accumulated round-off errors may lead to loss of conjugacy, i.e. violation of Eq. (A.8) [Renouf & Alart, 2005]. Such violation implies that the algorithm may not work in the same manner as it works for a linear system of equations. For example, $\nabla_{\boldsymbol{\theta}}\Pi$ may point to a direction of increase in Π . To avoid loss of conjugacy, the iterative procedure is periodically refreshed every k_{SD} iterations by setting $\beta^k = 0$, equivalent to performing an SD step, see Figure A.2. The frequency of this operation is determined by trial and error.

The iterative scheme is stopped if convergence has been achieved within a given tolerance, or otherwise if a specified number of iterations k_{max} has been exceeded. The tolerance is specified by

$$\Pi^{k-1} - \Pi^k < \tau_1 \left| \Pi(\mathbf{x}^{k-1}) \right| \quad \text{or} \quad \left\| \nabla_{\boldsymbol{\theta}} \Pi|_{\boldsymbol{\theta}^k} \right\|^2 < \tau_2 N (\bar{E} \bar{R}^2)^2 \quad (\text{A.12})$$

where \bar{R} and \bar{E} are the mean grain radius and Young's modulus. For example, for sample *G2740* with $\bar{E} = 7 \cdot 10^{10}$ Pa and $\bar{R} = 10^{-4}$ m, the following tolerance parameters were chosen: $\tau_1 = 10^{-11}$ and $\tau_2 = 10^{-5}$. These values provide for each grain a residual force, \mathbf{F}_i , and moment, \mathbf{M}_i , which are smaller than the maximum contact force and moment on that grain by at least 4 orders of magnitude. Note that due to inevitable round-off errors, the chosen tolerance cannot be arbitrarily small.

Finally, we note that the zero gradient of a functional may correspond to a local maximum, saddle point, or a flat surface of a functional. While we do not provide here a rigorous proof, we stress that the physical meaning of Π implies that its zero gradient corresponds to a local minimum.

A.2.2 Conjugate gradient implemented in the cemented pack model

In modeling a cemented grain pack (Chapter 4), we improve the performance of the minimization algorithm presented in Sections A.2.1.1–A.2.1.3 by linearizing the constitutive relations. This linearization is justified by the smallness of the incremental grain displacements following each load increment, \mathbf{u}_i . Linearization is performed within the iterative scheme by: (I) evaluating the intergranular loads based on the *reference* configuration, i.e. fixing the load directions, the effective contact stiffness, and the contact network; followed by (II) updating the grain locations with the grain displacements obtained in (I), and resolving for the intergranular loads based on the *updated* reference configuration, see Figure A.3. Note that in step (II), the boundary conditions are not perturbed. However, since the directions of the loads are updated, the system will reach a new equilibrium configuration. In both (I) and (II), the linear equations and the corresponding quadratic functional allow to compute the update coefficient α by Eq. (A.5). The use of a closed-form expression rather than an iterative minimization (cf. Section A.2.1.2) reduces the computational cost, and improves the accuracy of the computations, see Section 4.8.2. Since loss of conjugacy can occur due to round-off errors, the search directions are refreshed every k_{SD} iterations, see Section A.2.1.3.

- (1) Begin step (I): set FLAG=I.
- (2) Initial guess ($k = 0$): $\boldsymbol{\theta}^{k=0} = \mathbf{0}$. Set $\mathbf{p}^{k=0} = \nabla_{\boldsymbol{\theta}} \Pi|_{\boldsymbol{\theta}^{k=0}}$.
- (3) IF k divisible by k_{inc} AND $\mathbf{u}_w^k < \mathbf{u}_w$, apply incremental perturbation:
 - (a) Update boundary conditions: $\mathbf{x}_w^k \leftarrow \mathbf{x}_w^k + \Delta \mathbf{u}_w^k$ and $\mathbf{u}_w^k \leftarrow \mathbf{u}_w^k + \Delta \mathbf{u}_w^k$
 - (b) Update the grain displacements (“initial guess”): $\mathbf{u}_i^k \leftarrow \mathbf{u}_i^k + \Delta \mathbf{u}_i^k$, cf. Eq. (A.11), keeping the grain positions fixed: $\mathbf{r}_i^k = \begin{cases} \mathbf{r}_i^{k=0} & \text{If FLAG=I} \\ \mathbf{r}_i^{k=k^*} & \text{If FLAG=II} \end{cases}$
- (4) Evaluate $\nabla_{\boldsymbol{\theta}} \Pi|_{\boldsymbol{\theta}^k}$.
- (5) IF $k = 1$ OR $k = k^*$ OR k divisible by k_{SD} , refresh with an SD step: set $\beta^k = 0$.
 ELSE $\beta^k = - \left(\frac{\|\nabla_{\boldsymbol{\theta}} \Pi|_{\boldsymbol{\theta}^k}\|}{\|\nabla_{\boldsymbol{\theta}} \Pi|_{\boldsymbol{\theta}^{k-1}}\|} \right)^2$.
- (6) $\mathbf{p}^k = \nabla_{\boldsymbol{\theta}} \Pi|_{\boldsymbol{\theta}^k} - \beta^k \mathbf{p}^{k-1}$.
- (7) Given $\boldsymbol{\theta}^k$, \mathbf{p}^k and $\nabla_{\boldsymbol{\theta}} \Pi|_{\boldsymbol{\theta}^k}$, find α^k by Eq. (A.5).
- (8) Update the generalized coordinates, $\boldsymbol{\theta}^{k+1} = \boldsymbol{\theta}^k - \alpha^k \mathbf{p}^k$, keeping the grain positions fixed.
- (9) Check convergence:
 IF $\Pi(\mathbf{x}^{k-1}) - \Pi(\mathbf{x}^k) < \tau_1 |\Pi(\mathbf{x}^{k-1})|$ OR $\|\nabla_{\boldsymbol{\theta}} \Pi|_{\boldsymbol{\theta}^k}\|^2 < \tau_2 N (\bar{E} \bar{R}^2)^2$ OR $k > k_{max}$:
 IF FLAG=I, set FLAG=II and $k = k^*$, and begin step (II). Update the grain positions with $\boldsymbol{\theta}^{k+1}$, i.e. $\mathbf{r}_i^{k^*} = \mathbf{r}_i^0 + \mathbf{u}_i^{k+1}$, and reset the generalized coordinates to zero, $\mathbf{u}_i^{k^*+1} = 0$ and $\boldsymbol{\Omega}_i^{k^*+1} = 0$, to be used as an initial guess. Set $k \leftarrow k + 1$, $\mathbf{u}_w = 0$, and restart the process from Step 4.
 ELSE (FLAG=II), STOP.
 ELSE Set $k \leftarrow k + 1$ and GOTO Step 3.

Figure A.3: A numerical algorithm used in simulating application of a load increment and obtaining an equilibrium configuration, employed in the cemented pack model, cf. Chapter 4.